UNIVERSITY OF SOUTHAMPTON

FACULTY OF ENGINEERING, SCIENCE AND MATHEMATICS

SCHOOL OF PHYSICS AND ASTRONOMY

Femtosecond pulse generation in surface-emitting semiconductor lasers

Adrian Hugh Quarterman

Submitted for the degree of Doctor of Philosophy

July 2009

UNIVERSITY OF SOUTHAMPTON

ABSTRACT

Faculty of Engineering, Science and Mathematics

School of Physics and Astronomy

Doctor of Philosophy

Femtosecond pulse generation in surface-emitting semiconductor lasers

Adrian Hugh Quarterman

In this thesis I report significant advances towards the goal of stable ultrashort pulse generation in mode-locked optically pumped vertical external-cavity surface-emitting lasers (VECSELs). Continuous wave VECSELs were first designed as a type of semiconductor laser capable of producing high output power in near transform-limited beams. Optical pumping allows the output power of the device to be increased simply by increasing the pumped area of the sample, and an external cavity forces the laser into single transverse mode operation. VECSELs' external cavities also allow for the insertion of semiconductor saturable absorber mirrors (SESAMs) for modelocking. Mode-locked VECSELs have surpassed the performance of other types of mode-locked semiconductor laser, with modelocking via the optical Stark effect allowing VECSELs to produce sub-picosecond pulses in transform-limited beams, at power levels up to 100 mW and at GHz repetition rates.

The work presented in this thesis describes recent progress in reducing the durations of VECSEL pulses to below 100 fs. At these pulse durations, gain saturation forces the laser oscillator to enter a dynamic regime never before seen in semiconductor lasers, which is also investigated here. In addition, the timing jitter of a VECSEL mode-locked using the optical Stark effect is characterised for the first time, and a versatile frequency-divider-based active stabilisation technique is demonstrated. Finally, the fabrication of carbon nanotube based saturable absorbers for VECSEL modelocking via solution processing is investigated.

Contents

List of Figures

Declaration of Authorship

I, Adrian Hugh Quarterman, declare that the thesis entitled 'Femtosecond pulse generation in surface-emitting semiconductor lasers' and the work presented in it are my own. I confirm that:

- this work was done wholly or mainly while in candidature for a research degree at this University;
- where any part of this thesis has previously been submitted for a degree or any other qualification at this University or any other institution, this has been clearly stated;
- where I have consulted the published work of others, this is always clearly attributed;
- where I have quoted from the work of others, the source is always given. With the exception of such quotations, this thesis is entirely my own work;
- I have acknowledged all main sources of help;
- where the thesis is based on work done by myself jointly with others, I have made clear exactly what was done by others and what I have contributed myself;
- parts of this work have been published as listed on the following page.

Signed:

Date: 07/07/2009

Acknowledgements

I would like to thank the many people who have contributed in many ways to this work. Firstly, I would like to thank my supervisor, Professor Anne Tropper, for making the last three years hugely enjoyable and educational, thanks to her tireless enthusiasm, excellent advice and the many impromptu physics lessons. I am also indebted to Dr Vasilis Apostolopoulos for many valuable discussions, a great deal of good advice, and for correcting my latin.

Thanks also to the various group members that I have worked with. In particular I would like to thank Steve Elsmere, Zak Mihoubi and Keith 'If it was easy someone would have already done it' Wilcox for the many fruitful discussions, an excellent education in practical physics, and for the three highly entertaining years. Many thanks also to Aaron Chung and Stuart Nardone who joined the group more recently.

I would like to acknowledge all the department support and technical staff, without whom little of this work would have been possible. Thanks to all the electrical and mechanical workshop staff, in particular thanks to Chad and Gareth in the electronics workshop for their advice and their patience, and to Phil Connell in the mechanical workshop for the beautiful stabilised laser base.

Many thanks to all the other members of the Quantum Light and Matter group for shared ideas and advice.

Finally, I am most grateful to my family and friends for their love and support.

Adrian Quarterman

July 2009

Chapter 1

Introduction

The vertical external-cavity surface-emitting laser (VECSEL) is a type of semiconductor laser that is designed to provide high power, high beam quality laser output. Since the first demonstration of a VECSEL by Kuznetsov et al. in 1997 [7] interest in these lasers has grown rapidly due to their great potential as a flexible, high brightness source.

Traditionally, semiconductor lasers have been either edge emitting diode lasers or surface emitting diode lasers, known as vertical cavity surface-emitting lasers (VCSELs). Single edge emitting diode lasers are capable of reaching multi-watt power levels, but the use of a high aspect ratio active region results in output beams with very poor beam quality. The beam quality of such lasers can be improved by using a waveguide active region to give single mode output but this limits the power to a few watts. VCSELs emit beams vertically from a circular active region, and therefore can produce circular, transform limited output beams. The size of the emitting region is typically around 10 μm however, limiting the output powers to tens of milliwatts in transform limited beams. Large active regions can be used to reach higher powers, but it is very difficult to achieve a uniform current density across such a large area. Such large area devices are also prone to multimode operation, reducing the beam quality.

VECSELs achieve high powers with good beam quality by emitting light vertically from a larger active region and by using an external focussing cavity mirror. The problems of uniform pumping and limited emitting areas suffered by VCSELs are overcome by using optical pumping rather than electrical pumping. In this way uniform carrier density can be achieved across large areas, allowing power scaling simply by increasing

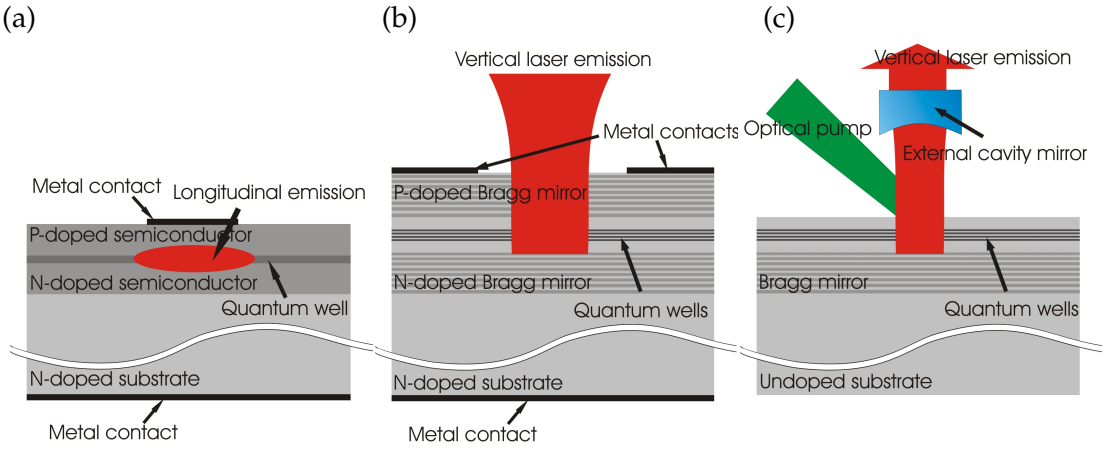

Figure 1.1: Schematics of (a) an edge-emitting diode laser, (b) a VCSEL and (c) a VECSEL. The diagram shows the layer structure and major components of the three types of laser. Note that in the edge-emitting diode the laser beam is emitted in the plane of the semiconductor layers whereas in the VCSEL and VECSEL emission is perpendicular to the layers.

the spot size of the pump laser in the same way as thin disc solid state lasers. VECSEL's external cavities can ensure close to transform limited beam quality. Figure 1.1 shows schematic views of an edge-emitting diode, a VCSEL and a VECSEL.

Using optical pumping also leads to much simpler sample design and processing. Samples no longer need to use doped semiconductors to conduct carriers to the active regions. This significantly reduces the overall loss of the device by eliminating free carrier absorption. Sample processing is simplified as no contacting of the device is needed. In some cases samples can be cleaved directly from a wafer and used without further processing, though in many cases some processing is performed in order to improve the thermal characteristics, and therefore the efficiency of the device. Optical pumping has its disadvantages however, most notably the scale of the device. Whereas edge emitting diodes and VCSELs are millimeter scale devices, VECSELs are typically shoebox-size lasers.

High power CW operation has been the focus of much of the work into VECSELs as they can provide multi-watt output from a very compact device over a large range of wavelengths. The first VECSEL produced an output of 0.5 W at a wavelength of 1 μm. The output power is largely limited by the temperature of the active region. Improved thermal management, principally either by removing the sample substrate or

by bonding the sample to a transparent intracavity heatspreader, have lead to significant increases in output power. Since their first demonstration powers have increased to over 30 W at wavelengths around 1 μm [8–10]. Heatspreader-bonded VECSELs have seen similar progress, reaching powers as high as 10 W [11–13].

An alternative to increasing the thermal conductivity of the sample is to reduce the heat deposited. In-well pumping reduces the quantum defect of the laser by pumping at wavelengths very close to the laser wavelength and absorbing the pump radiation in the quantum wells instead of in pump absorbing barrier layers. This also results in increased efficiency. The disadvantage of this method lies in the extremely short absorption length of the quantum wells. Such lasers must use several passes of the pump beam throught the active region in order to absorb enough pump power. Several systems at different wavelengths have been demonstrated using this method including 850 nm [14], 1 μm [15] and 2.3 μm [16]. Other novel pumping methods are also researched. Electrically pumped VECSELs have been demonstrated [17], most notably by Novalux, as well as integrated optical pumping schemes [18].

VECSELs benefit from the high spectral versatility of semiconductor lasers. A wide range of emission wavelengths can be selected by bandgap engineering, and the emission wavelengths of individual devices can be highly tunable thanks to the broad lasing bandwidths of semiconductor quantum wells. VECSELs have been demonstrated in several materials systems with different wavelength ranges. The most common materials system is the GaAs/AlAs/InGaAs system for lasers around 1 μm [8, 10, 13, 19].

Longer wavelength VECSELs have been demonstrated at wavelengths around 1.2-1.3 μm using GaInNAs based materials [20] and highly strained InGaAs quantum wells [21], and 1.5 μm using InP based materials [22, 23]. The low refractive index contrasts, poor thermal conductivity and high two-photon absorption coefficients of the InP materials system make VECSELs inefficient at these wavelengths, limiting output powers to less than 1 W. Wafer bonding techniques have used to bond InP based active regions onto a GaAs based Bragg mirrors allowing watt-level output powers at the expense of complex sample processing [24]. VECSELs around 2-2.3 μm, using GaSb based materials, have been demonstrated with powers up to 5W [25] and with tuning ranges of up to 150 nm [26]. Wavelengths as long as 5.3 μm have been demonstrated

using small bandgap PbTe semiconductors [27].

One of the largest potential markets for VECSELs is their use in RGB projection systems. There has therefore also been significant work on VECSELs at shorter wavelengths. Powers of up to 0.5 W have been demonstrated at 850 nm using AlGaAs based materials [28] and of up to 0.4 W in the red part of the spectrum [29].

An alternative route to shorter wavelengths is to use second harmonic generation (SHG) with infrared lasers. The external cavities and high intracavity powers of VECSELs make them ideal candidates for intracavity SHG. Frequency doubling of VECSELs between 1.2 μm and 900 nm has allowed several watts of red [30], green [31] and blue [32] to be generated. Frequency doubling of red VECSELs has given outputs of hundreds of milliwatts in the ultraviolet [33].

The external cavities of VECSELs also make them suitable candidates for passive modelocking using semiconductor saturable absorber mirrors (SESAMs). The optical path lengths through semiconductors in VECSELs are very small, reducing the strong phase modulation effects suffered by other types of semiconductor lasers and allowing them to generate nearly transform limited ultrashort pulses.

Passive modelocking has been demonstrated over a range of wavelengths, including 1.5 μm [34], 1.2 μm [35], 1 μm [36] and 830 nm [37], generally producing pulses with picosecond durations at power levels of hundreds of milliwatts. Again, the highest performances have been achieved around 1 μm. Here, powers of up to 2 W have been achieved [38], and the use of SESAMs designed to operate in the optical Stark regime has allowed sub-picosecond pulse durations [39,40]. The thin disc geometry of VECSELs also allows modelocking at high repetition rates, up to 50 GHz having been demonstrated with picosecond pulse durations [41] and up to 10 GHz with femtosecond pulses [42].

All the VECSELs described above use quantum well gain structures. Research has also been conducted into quantum dots, as they offer greater wavelength flexibility in gain structures and improved recovery times and saturation fluences in SESAMs. Both sub-monolayer [43] and Stranski-Krastanow [44] quantum dot gain structures have been used to give watt-level CW performance at wavelengths near to 1 μm. Passive modelocking has been demonstrated in both VECSELs with quantum well gain sam-

ples and quantum dot SESAMs [41] and quantum dot gain structures and quantum well SESAMs [45]. Recently, a quantum well gain region and quantum dot SESAM have been integrated into a single structure called a Mode-locked Integrated External-Cavity Surface-Emitting Laser, or MIXSEL [46], demonstrating 30 ps duration pulses and the promise of extremely compact modelocked VECSELs.

This thesis begins by describing the essential features of mode-locked VECSELs and the theoretical models used to describe the different modelocking regimes observed. In chapter 4 I describe in greater detail the features of VECSEL gain sample and SESAM design. Results are presented for VECSELs producing 500 fs, 260 fs [47] and sub-100-fs pulses [48], and the changes in sample design required to achieve these pulse durations are explained. In the case of the sub-100-fs pulses a novel modelocking regime governed by rapid gain saturation is described and investigated.

Chapter 5 describes the active stabilisation of a sub-picosecond VECSEL, using the novel method of locking the repetition rate of the laser to an electrical oscillator at a much lower frequency. In this way the timing jitter of the laser is reduced to a value of 190 fs in the bandwidth 300 Hz to 1.5 MHz. Sources of pulse timing noise in modelocked VECSELs are identified and analysed, and applications for low-timing-jitter VECSELs are discussed.

Chapter 6 describes a study into the use of single-walled carbon nanotubes (SWCNTs) as a saturable absorber material for VECSEL modelocking. I examine the optical properties of SWCNTs and identify possible methods for the fabrication of such an absorber, including possible solution processing techniques. The mixed sucesses of these solution processing attempts are analysed, issues identified, and possibilities for future work suggested.

Chapter 2

Principles of VECSEL operation

2.1 Semiconductor properties and quantum well gain media

Semiconductors have great potential as a laser gain medium. Their large optical cross sections give them the potential for very high optical gain and they have unmatched potential for spectral versatility via the tuning of the material composition. They can also be pumped electrically, leading to highly efficient and low cost operation, and the atomic-level precision of epitaxial growth methods gives extraordinary control over the device structure.

Figure 2.1 shows the conduction and valence bands of gallium arsenide (GaAs). The band gap of this material is labelled as E_g, and it is important to note that in gallium arsenide the minimum energy gap occurs at the point where the valence band has a maximum and the conduction band a minimum. A semiconductor where these extrema both lie at the same momentum is known as a direct bandgap semiconductor. In direct bandgap semiconductors the probability of radiative trasitions at the band edge is high, making this type of material ideal for optical devices. Usually, the semiconductors used for optical devices are III-V semiconductors, alloys made of group III and group V elements. These alloys are mostly direct bandgap semiconductors and have the high optical transition cross sections required for laser operation.

Figure 2.2 shows the bandgaps and lattice spacings of several common III-V semiconductors. The bandgap of a semiconductor can be tailored by adjusting the composition of the alloy. For example, GaAs has a bandgap of 1.4 eV and AlAs has a bandgap

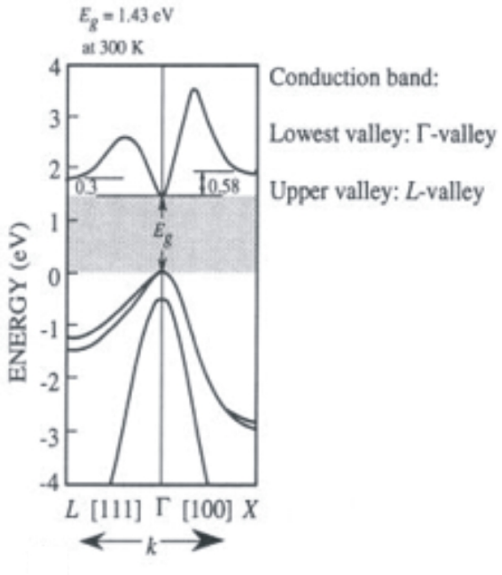

Figure 2.1: Band structure of gallium arsenide. The minima of the conduction band lies at the same momentum value as the maximum of the valence band, indicating that GaAs is a direct bandgap semiconductor. The three branches of the valence band are the heavy hole band, the light hole band and the spin-off band. Modified from [1].

of 2.2 eV. The bandgap of an $Al_xGa_{1-x}As$ alloy can be varied between these two values by tuning the aluminium fraction, x.

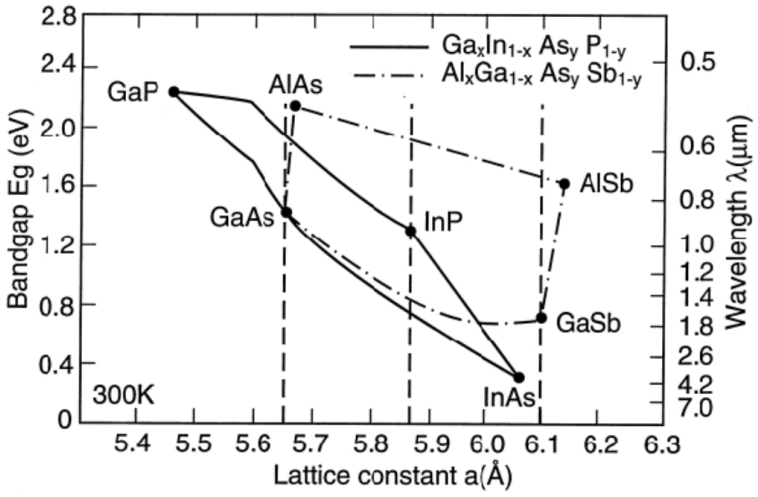

Figure 2.2: Diagram showing the band gaps and lattice constants of several common III-V semiconductors. Modified from [2].

The AlGaAs material system is a very convenient one to use as its lattice constant

changes very little over the whole composition range. This is not the case for most alloy systems, which can result in the device having overall strain due to mismatched lattice constants. If the strain is not compensated for it can cause defects to propagate through the material, severely limiting device lifetime. Strain compensating layers can be used to give the device no overall strain, as discussed in section 2.5.2.

Bulk semiconductor is rarely used as a gain medium as the current density required for laser threshold is very high. The threshold can be reduced by reducing the dimensionality of the gain medium. The medium can be confined to two dimensions, one dimension or zero dimensions leading to quantum wells, quantum wires or quantum dots. The different degrees of confinement give rise to different densities of states and therefore to different radiative transition rates.

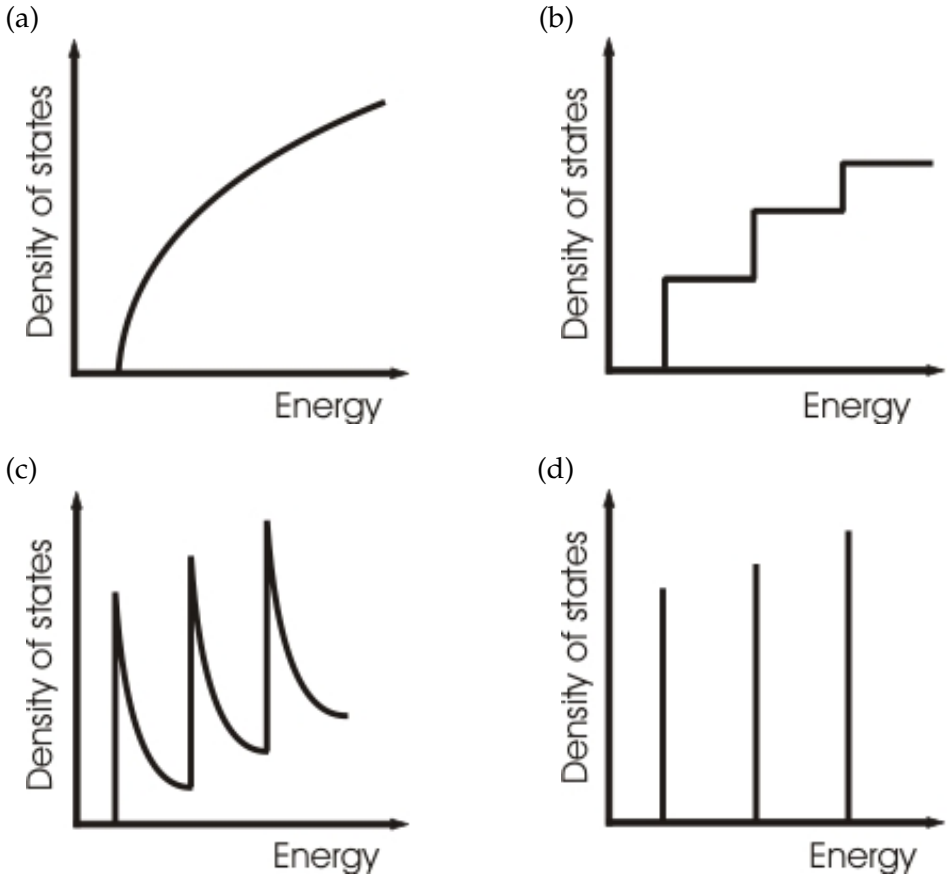

Figure 2.3: Density of states near the band edge for semiconductor materials with different degrees of confinement. (a) shows bulk semiconductor, (b) a quantum well, (c) a quantum wire, and (d) a quantum dot.

Figure 2.3 shows the density of states for the different degrees of confinement. It can be seen that increasing the degree of confinement causes an increase in the density of states at the band edge. VECSELs have been demonstrated using both quantum well and quantum dot gain media, but all those described in this work were based on quantum wells.

2.2 Gain in semiconductor quantum wells

In order to find the gain experienced by light passing through a quantum well we need to derive the rates of transitions between the conduction and valence bands. These rates can be found from the population densities, which depend of the pumping, and the transition probabilities, which can be calculated using Fermi's golden rule. The transition probability per second per unit volume can be calculated [49] to be

$$R_\tau(E) = \frac{e^2\lambda_0}{2c\epsilon_0 m_e^2 n^2} N_p \left|M_T\right|^2 \rho_j(E), \tag{2.1}$$

where n is the refractive index, N_p is the photon number density, $|M_T|$ is the matrix element of the transition and $\rho_j(E)$ is the joint density of states.

Momentum conservation rules mean that photons can only cause vertical transitions between the bands shown in figure 2.1, meaning that the joint density of states is given by the density of states in either the conduction or the valence band. Assuming that each band can be approximated by a parabola near to the zero momentum point, the joint density of states is given by

$$\rho_j(E) = \frac{m_{c,v}}{2\pi\hbar^2 L} \sum_{i=1}^{N_l} \Theta(h\nu - (E_{c_i} - E_{v_i})), \tag{2.2}$$

where Θ is the Heaviside function, $m_{c,v}$ is the effective mass of the carriers in the band and L is the thickness of the quantum well. As all the transitions in our lasers occur between the $i = 1$ levels equation 2.2 can be simplified to

$$\rho_j = \frac{m_{c,v}}{2\pi\hbar^2 L}. \tag{2.3}$$

The rates of stimulated transitions from one band to another is determined by the availability of carriers in one band and the availability of empty states in the other. The

transition rates from the conduction band to the valence band and from the valence band to the conduction band correspond to stimulated emission and absorption and are given by

$$R_{cv} = R_\tau f_c(1 - f_v), \tag{2.4}$$

and

$$R_{vc} = R_\tau f_v(1 - f_c), \tag{2.5}$$

where $f_{c,v}$ are the Fermi-Dirac functions describing the filling of the states in each band. In the steady state the probability of a carrier in a band being found at energy E is given by the Fermi-Dirac distributions in the two bands:

$$f_{c,v}(E) = \frac{1}{1 + e^{(E - E_{f_{c,v}})/k_b T}}, \tag{2.6}$$

where $E_{f_{c,v}}$ is the Fermi energy for each band.

If a laser beam passes through the medium then the rate at which photons are added to the beam is given by the difference between the rates of stimulated emission and absorption, leading to the equation for the gain per unit length

$$g = \frac{n}{cN_p}\left(R_{cv} - R_{vc}\right) = \frac{e^2 \lambda_0 \left|M_T\right|^2}{2c^2 \epsilon_0 m_e^2 n}\left(f_c - f_v\right)\rho_j(E). \tag{2.7}$$

The rate equation for the photon number in the device can be found by integrating the stimulated emission and absorption terms over the gain medium to find

$$\frac{dN_p}{dt} = \Gamma_z \int R_\tau f_c(1 - f_v)dz - \Gamma_z \int R_\tau f_v(1 - f_c)dz - \frac{N_p}{\tau_p}, \tag{2.8}$$

where the first and second terms describe the effect of stimulated emission and absorption and the third term describes the fixed cavity loss in terms of a cavity lifetime τ_p. The overlap between the electric field distribution and the quantum well is described by the longitudinal confinement factor Γ_z.

The gain experienced will become positive when $f_c > f_v$ which is equivelent to requiring that $E_{f_c} > E_{f_v}$. The Fermi levels in the conduction and valence bands are determined by the carrier densities in the bands by noting that the total number of carriers in a band is given by

$$N = \int_0^\infty f_{c,v}(E)\rho_{c,v}(E)dE, \tag{2.9}$$

from which one can find

$$E_{f_c} = k_b T \ln\left(e^{\frac{N_c \pi \hbar^2 L}{m_e k_b T}} - 1\right), \tag{2.10}$$

and

$$E_{f_v} = k_b T \ln\left(e^{\frac{N_v \pi \hbar^2 L}{m_h k_b T}} - 1\right). \tag{2.11}$$

If the device is pumped so as to move carriers from the valence band to the conduction band then the carrier density will increase until the condition for positive gain is met. The point at which stimulated emission exactly matches absorption is known as transparency. Carrier densities at transparency for quantum wells are typically of the order of 10^{18} cm^{-3}. Figure 2.4 shows the gain of a single InGaAs quantum well as a function of carrier density above and below threshold. As the carrier density increases the gain can be seen to increase until threshold is reached at 0.88×10^{18} cm^{-3}. As the carrier density is increased further the gain approaches a maximum value of approximately 0.6%.

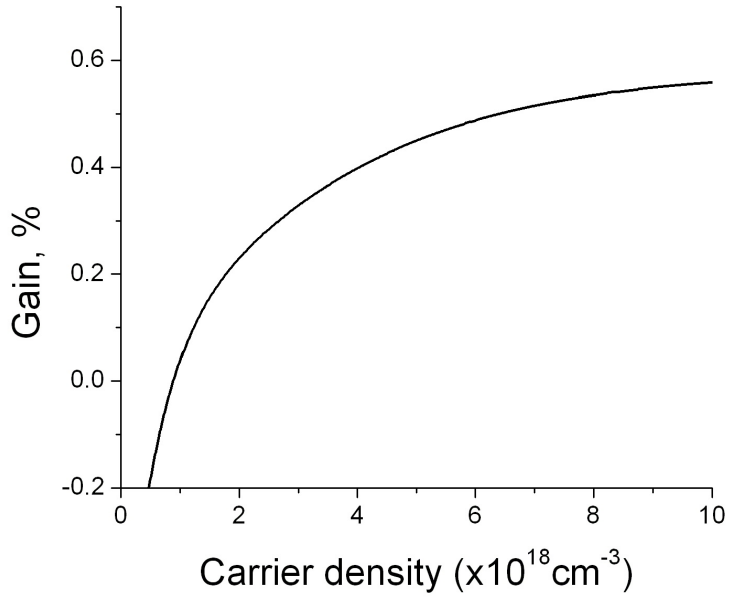

Figure 2.4: Gain of a single 8 nm thick $In_{0.25}Ga_{0.75}As$ quantum well as a function of carrier density. Transparency is reached at a carrier density of 0.88×10^{18} cm^{-3} and the maximum gain is 0.58%.

Rate equations for the numbers of carriers in the conduction and valence bands can

also be defined. If pumping shifts carriers from the valence band to the conduction band at a rate R_P, then

$$\frac{dN_c}{dt} = R_P - \Gamma_z \int R_\tau f_c(1-f_v)dz + \Gamma_z \int R_\tau f_v(1-f_c)dz - R_{waste}(N_c), \qquad (2.12)$$

and

$$\frac{dN_v}{dt} = -R_P + \Gamma_z \int R_\tau f_c(1-f_v)dz - \Gamma_z \int R_\tau f_v(1-f_c)dz + R_{waste}(N_c). \qquad (2.13)$$

$R_{waste}(N_c)$ includes all 'wasted' recombinations which do not add photons to the laser beam. As such it includes spontaneous emission (assuming that few photons are spontaneously emitted into the laser mode), which depends quadratically on N_c, as well as the non-radiative recombination mechanisms described in the following section.

2.3 Non-radiative processes in semiconductors

In addition to the radiative processes described above it is worth considering some of the non-radiative processes that affect laser operation. Some of these effects allow non-radiative recombination and therefore will reduce the fraction of excited carriers that contribute to laser gain. The processes affecting the carrier distribution inside a band are also described briefly.

In the VECSEL gain structure described below in section 2.5, carriers are generated by absorption of 830 nm radiation in a GaAs region. The carriers then travel through the semiconductor until they reach an InGaAs quantum well, where they lose energy via scattering processes to drop into the quantum well, forming a Fermi-Dirac distribution as described above.

Two scattering processes are involved in the formation of this Fermi-Dirac distribution. Firstly, carrier-carrier scattering allows the electrons to form a distribution with a particular characteristic temperature. Carrier-phonon scattering then allows the electrons to exchange energy with the crystal lattice, allowing the temperature of the distribution to equalise with that of the lattice.

These processes occur over timescales determined by the scattering processes. For the InGaAs quantum wells used in both the gain samples and the SESAMs used in this work the carrier-carrier scattering time is approximately 35 fs and the carrier-phonon

scattering time is of the order of a few hundred femtoseconds. Both scattering times increase with both carrier density and temperature, and can therefore be expected to be shorter in the gain sample than the SESAM. In the steady state these mechanisms have a limited effect on the laser behaviour as they are both much shorter than the timescale over which the pump laser replaces carriers. They become important, however, when pulses passing through the medium approach these timescales, as is discussed in chapter 4.

Besides radiative recombination, the two main recombination processes are recombination at defect sites and Auger recombination. These three processes all depend differently on the carrier density. Defect recombination occurs when carriers scatter off defects in the material, giving their energy to the lattice. The rate at which this process occurs depends linearly on the density of defects and on the carrier density. Loss of carriers in the gain sample through this mechanism can therefore be reduced by using high quality growth processes such as molecular beam epitaxy. In a SESAM a high defect density can be desirable as it speeds up the overall recovery, as discussed in section 4.2.2.

Auger recombination occurs when an electron loses its energy by scattering off another carrier. This process requires three carriers to be present, an electron and a hole to recombine with each other and a third carrier to conserve energy and momentum. Auger recombination therefore depends on the cube of the carrier density, becoming a major source of loss in VECSELs at high pump powers.

Taking defect recombination and Auger recombination into account as well as spontaneous emission it is now possible to find an expression for the rate of 'wasted' recombinations in equations 2.12 and 2.13 as

$$R_{waste}(N_c) = AN_c + BN_c^2 + CN_c^3, \tag{2.14}$$

where the three terms describe defect recombination, spontaneous emission and Auger recombination respectively.

Auger recombination also depends on the carrier-carrier scattering time, which increases with temperature. As Auger recombination converts the energy of the electron to heat, it is clear that a runaway process can occur. As the temperature rises Auger recombination will become increasingly probable, resulting in more heat being dumped

into the sample and reducing the gain. The positive feedback in this process can result in large temperature increases, and beyond a certain pump threshold will severely reduce the gain of the device in a process known as thermal rollover. Devices with low threshold carrier densities and good thermal characteristics are less susceptible to thermal rollover, making such properties desirable.

2.4 Components of mode-locked VECSELs

VECSELs were originally conceived as semiconductor lasers which could give high output powers in transform limited beams, something that is difficult to achieve in traditional electrically pumped semiconductor lasers. Figure 2.5 shows a VECSEL. The gain sample is an active mirror, amplifying the light reflected from it. The laser cavity is formed between this active mirror and an external cavity mirror. The sample is pumped in a circular spot by another laser, usually a fibre coupled diode laser. The pump light is absorbed in pump-absorbing layers near the quantum wells, allowing carriers generated in the pump absorbing layers to move into the quantum wells, providing gain. Once the carrier density is above threshold then light emitted by the quantum wells into the cavity defined by the DBR and the external mirror will begin to oscillate. An output coupler is used as the external mirror, allowing useful output to be extracted.

VECSELs can give output powers of several watts in transform-limited beams. The external cavity also makes it possible to add further elements into the laser. CW VECSELs often use intracavity second harmonic crystals to convert infrared radiation to visible wavelengths. Alternatively, saturable absorbers can be introduced in order to mode-lock the laser.

2.5 VECSEL gain samples

Figure 2.6 shows the general type of VECSEL gain sample used in this work. It can be split into two major parts; the DBR mirror, and the active region which contains both pump absorbing layers and quantum wells. A high reflectivity AlAs/GaAs DBR is used as a cavity end mirror. The active region contains GaAs pump absorbing lay-

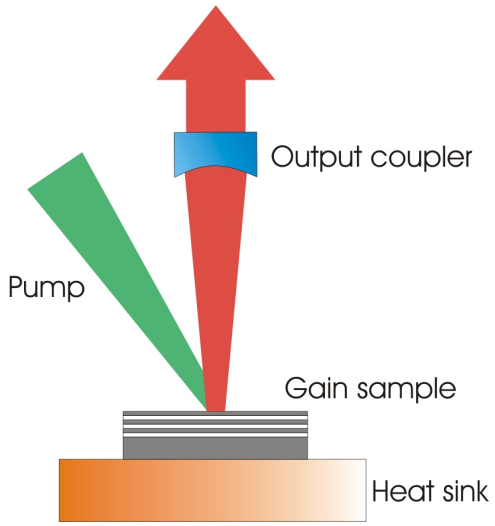

Figure 2.5: VECSEL schematic. Pump light is shown in green, laser light in red. The cavity is formed between the gain sample and the external output coupler.

ers where carriers are generated, which then move into the InGaAs quantum wells to provide gain.

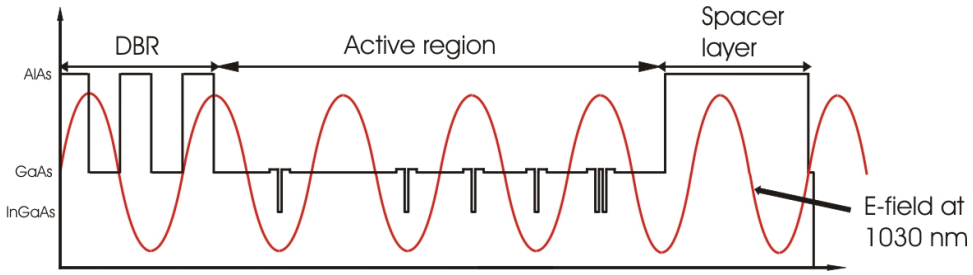

Figure 2.6: Gain sample layer structure showing the DBR, active region with quantum wells, and the spacer layer.

The overall thickness of the sample is also important as a microcavity is formed between the DBR and the sample surface. This microcavity acts as an etalon whose spectral filtering effects muct be carefully controlled. These features are described in the following sections. In particular, I will discuss how best to design each component for sub-picosecond pulse generation.

2.5.1 Distributed Bragg reflectors

Light passing from low index to high index material is partially reflected at the interface between the two materials. If alternating quarter-wavelength thick layers of high and low index material are used then the reflections from the high-to-low index interfaces will add constructively to give a much higher reflectivity than can be achieved using a single layer, as shown in figure 2.7.

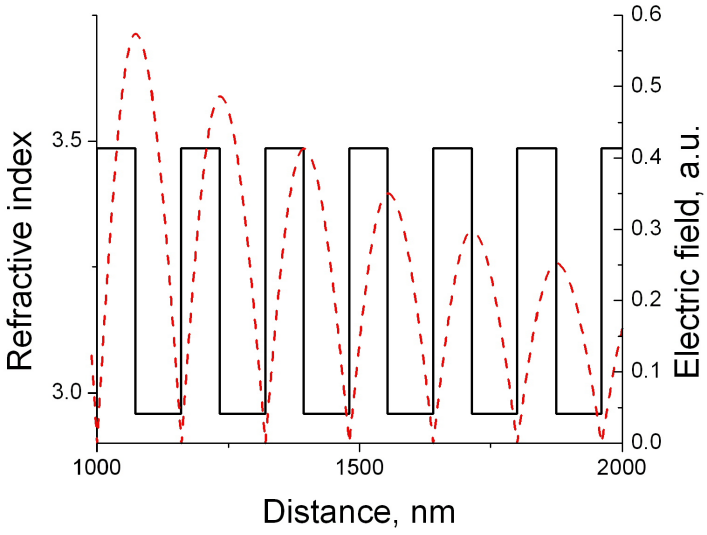

Figure 2.7: DBR multilayer reflective coating. Light arriving from the left experiences reflection from each low-index-to-high-index interface. The reflected waves add in phase to give high reflectivity, causing the amplitude of the electric field to decay rapidly through the material.

The reflectivity of such a mirror is governed by two factors. The index contrast between the high and low index layers determines how much light is reflected at each interface. A high index contrast is therefore desirable. The second factor is the number of layers. If a fixed percentage of the light is reflected at each interface then it is clear that the light transmitted by the DBR at the design wavelength will decrease exponentially with the number of layers.

The VECSELs used in this work all operate at wavelengths around 1030 nm. The GaAs/AlAs material system is ideal for use at these wavelengths. The wide lattice matching range described in section 2.1 means that a high index contrast is possible

without introducing strain to the DBR. The bandgaps of GaAs and AlAs are both large enough that light at 1030 nm is not absorbed, but the 830 nm pump radiation used in 1030 nm VECSELs is absorbed in GaAs. Pump absorption in the DBR might at first glance seem unimportant, as any pump radiation not absorbed in the active region is lost anyway, however absorption of the pump in the DBR increases the thermal load of the gain chip which reduces its efficiency. $Ga_{0.8}Al_{0.2}As$/AlAs can be used instead of GaAs as the pump radiation is not absorbed in $Ga_{0.8}Al_{0.2}As$. This would increase the efficiency of the sample but the refractive index contrast is reduced, meaning that more repeats are needed and resulting in worse dispersion characteristics. All the samples used in this work used GaAs/AlAs DBRs.

Properties of multilayered structures can be calculated by using a transfer matrix approach. Here the details of the layer structure are specified and the electric field inside the structure is calculated numerically using transfer matrices. Properties such as the reflectivity or the GDD of the multilayer can then be calculated from the known E-field. Figure 2.8 (a) shows calculated reflectivity spectra for $Ga_{0.8}Al_{0.2}As$/AlAs DBRs with 21, 41 and 61 layers. The number of layers in the DBR is an important consideration. More layers will give a higher reflectivity but worse dispersive characteristics. The reflectivity at the design wavelength increases from 0.97 to 0.9999.

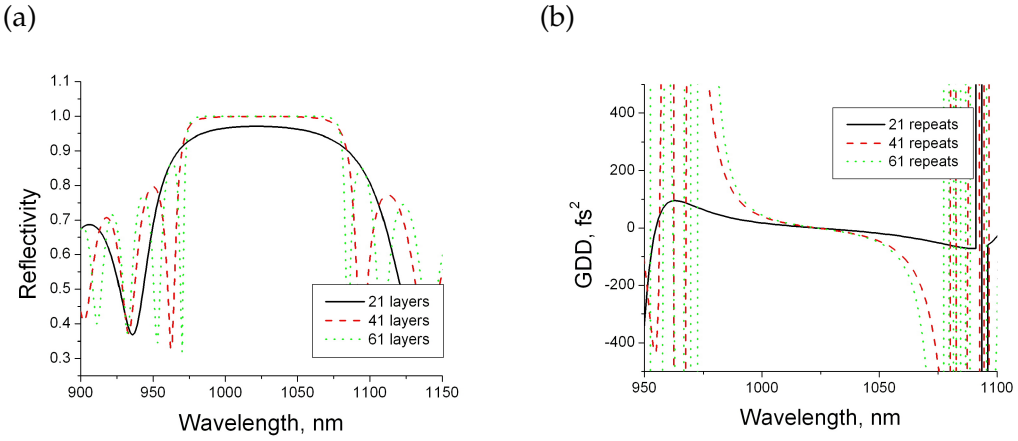

Figure 2.8: Reflectivity (a) and group delay dispersion (GDD) (b) of several DBRs with different numbers of layers. More layers give better reflectivity but at the price of a narrower stopband and more GDD.

The bandwidth of the DBR is of great importance in a modelocked VECSEL as large

lasing bandwidths are necessary to produce ultrashort pulses. In a low gain laser like a VECSEL even small changes in the reflectivity can have significant effects on the laser behaviour. Curvature of the stopband of the DBR is analogous to adding an intracavity wavelength filter, which is to be avoided if at all possible.

The phase change of light reflected from a DBR is also important. Material dispersion has a significant effect on the phase of the reflected light but, in addition different wavelengths of light are reflected at different effective depths in the DBR. This causes dispersion as the different wavelengths in an ultrashort pulse will experience different delays, resulting in pulse lengthening. This dispersion is minimised for high index contrast DBRs with a small number of repeats. Figure 2.8 (b) shows the second order dispersion of the same DBRs shown in figure 2.8 (a). The DBRs with fewer repeats can be seen to have lower second order dispersion.

As can be seen in figure 2.8, away from the centre wavelength a DBR introduces finite amounts of second order dispersion. DBRs can therefore be used to a limited extent as dispersion compensating elements, by choosing the centre wavelength of the DBR of a sample such that the desired amount of GDD will be experienced at the laser wavelength.

A DBR with 27.5 repeats is chosen for the gain samples used in this work as it provides a reflectivity of over 99.9% over a bandwidth greater than 100 nm and has suitably low dispersion. The centre wavelengths of the DBRs in individual samples are chosen to introduce the GDD required for dispersion compensation in a given laser.

2.5.2 Active region

The purpose of the active region is to provide laser gain. To this end it contains quantum wells which must be provided with carriers if they are to reach inversion and provide gain. The active region therefore also contains pump absorbing layers where pump radiation is absorbed to create carriers. These carriers must be generated close to the quantum wells so that they can reach the wells before they recombine.

Figure 2.9 shows a 1030 nm VECSEL active region containing six quantum wells and the standing wave field of 1030 nm light in the sample. Pump light arrives from the front surface of the sample and is absorbed in the GaAs. The quantum wells are

placed at the antinodes of the E-field in order to provide maximum gain. As the maximum gain for a single quantum well is 0.6% a sample with six wells has a maximum theoretical gain of 3.6%.

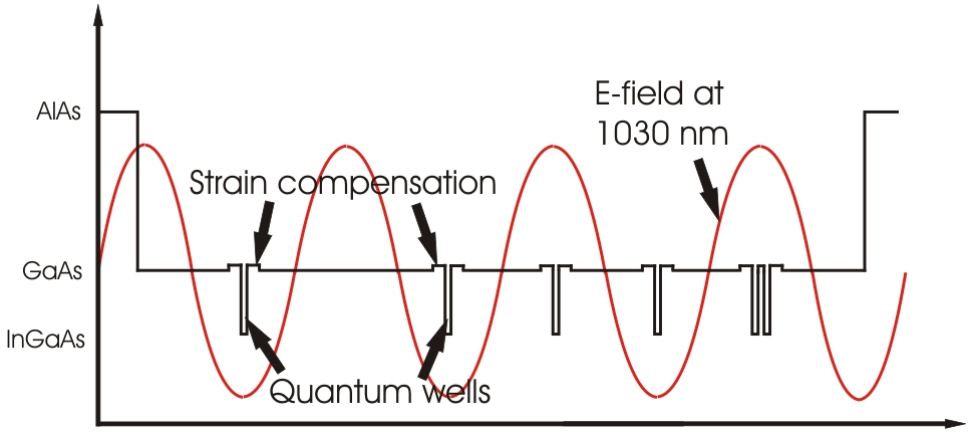

Figure 2.9: Active region of a VECSEL gain sample. The six quantum wells are spaced asymmetrically, with two wells at the first antinode of the E-field and a well missing from the second-to-last antinode.

The thickness of the active region is such that most of the pump radiation is absorbed. A 900 nm thick GaAs active region with an absorption coefficient of 1.2×10^4 cm^{-1} at 830 nm will absorb 70% of the pump radiation. The remaining 30% passes through the DBR and is lost. A thicker active region would absorb more pump but, as the pump is absorbed exponentially, the carrier density further away from the sample surface would quickly become too low to provide gain. If high efficiency is a priority then the DBR can be designed to reflect the pump wavelength back through the active region. This method results in a more complex DBR design and is not used in the gain samples used in this work.

The exponential absorption also determines the positions of the quantum wells, as the carrier density decreases exponentially away from the front surface of the sample. If the quantum wells were spaced evenly through the sample then the quantum wells nearer the front surface would recieve more carriers that those at the back. The different quantum wells would then have different gain spectra, resulting in inhomogeneous broadening. If the quantum wells are placed asymetrically, as shown in figure 2.9, with a double quantum well at the first antinode and one missing from the second-to-last antinode then the number of carriers recieved by each quantum well is approximately

the same.

The InGaAs quantum wells used in the samples in this work are not lattice matched to GaAs, leading to compressive strain in the wells. This is beneficial in that it increases the gain of the wells, but the overall compressive strain in the sample can reduce the device lifetime. In order to prevent this $GaAs_{0.94}P_{0.06}$ strain compensating layers can be placed either side of the quantum well. These layers are designed to have the same total amount of strain, but of the opposite sign. In this case the overall strain of the sample will be zero and the degradation prevented.

2.5.3 Gain sample microcavity and the longitudinal confinement factor

As can be seen in figure 2.6, a spacer layer of AlAs is grown on top of the active region, with a thin layer of GaAs is grown above it, next to the air interface to prevent the oxidation of the aluminium in the AlAs spacer layer. The thickness of the spacer layer decides whether the sample will be resonant or antiresonant depending on whether there is a node or an antinode of the E-field at the sample surface. Figure 2.10 shows the electric field in both resonant and antiresonant samples.

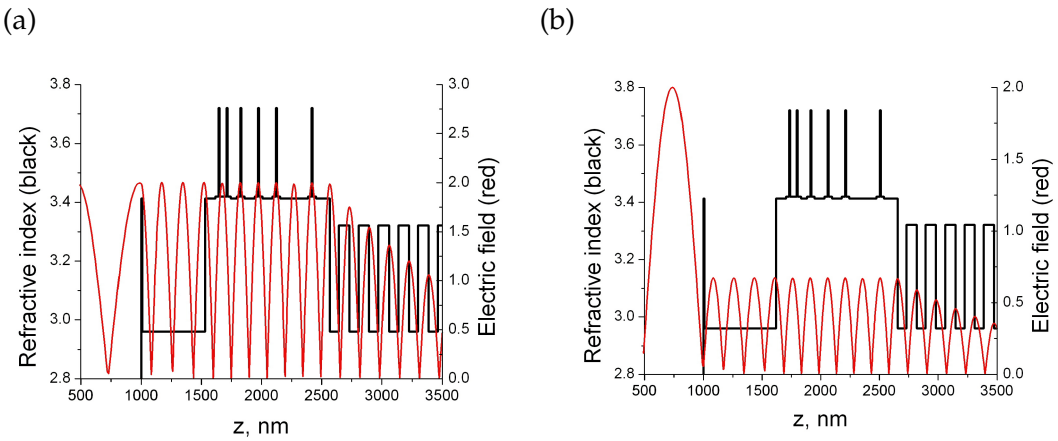

Figure 2.10: Electric field as a function of position inside both resonant (a) and antiresonant (b) gain samples. The resonant sample has an antinode at the surface and a high E-field amplitude inside the sample, the antiresonant sample has a node at the surface and a much weaker E-field inside the sample. The sample surface is at z = 1000nm.

At first glance a resonant sample seems more desirable as the electric field is larger inside this structure, giving a higher electric field on the quantum wells and there-

fore higher gain. Due to their higher gain, resonant samples are usually used for CW VECSELs. However, the resonant nature of the structure causes severe issues in mode-locked VECSELs due to dispersion and the gain filtering effect of the longitudinal confinement factor (LCF). The antiresonant structure has lower gain, but a much larger gain bandwidth and improved dispersive characteristics.

The longitudinal confinement factor, Γ_z, of a sample is a measure of the overlap between the electric field and the quantum wells. For a sample with n quantum wells it is defined as

$$\Gamma_z = \frac{\sum_n |E(z_n)|^2}{|E_0|^2} \tag{2.15}$$

where $|E(z_n)|^2$ are the squared moduli of the electric fields at the positions of the quantum wells and $|E_0|^2$ is the squared modulus of the electric field outside the sample. Figure 2.11 shows the LCF as a function of wavelength for ideal resonant and antiresonant samples. The LCF for the resonant sample has a higher value at the design wavelength indicating higher gain, but it is clear that using a resonant sample will restrict the sample to operating over a very small range of wavelengths. The LCF for the antiresonant sample is lower, meaning lower gain, but it is flatter over a larger wavelength range making it more suitable for the large bandwidths required for short pulse generation.

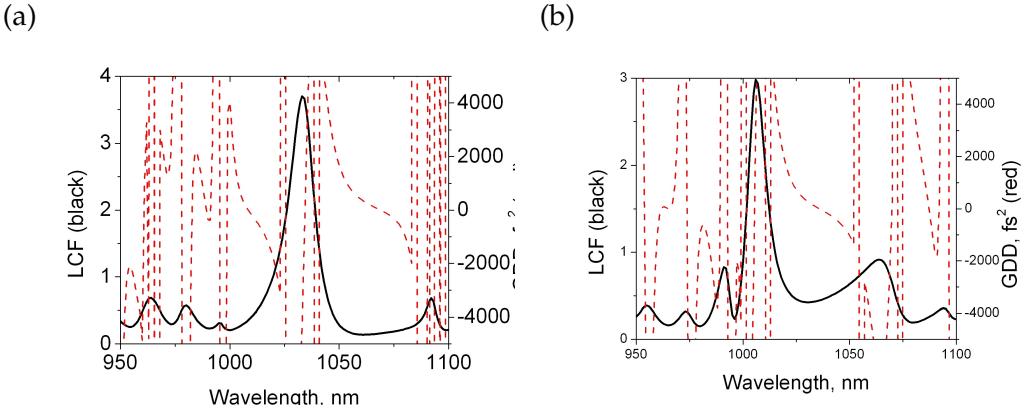

Figure 2.11: LCF (solid line) and GDD (dashed line) as a function of wavelength for both resonant (a) and antiresonant (b) gain samples. The design wavelength is 1035 nm.

Figure 2.11 also shows the group delay dispersion (GDD) in the two samples. In the resonant case the phase goes through large excursions at the design wavelength, resulting in very high values of GDD and of higher order dispersion. This is clearly

an issue for ultrashort pulse generation as such high values of dispersion will cause pulse distortion and lengthening. If the dispersion was solely second order then external compression could potentially be used to compress the output pulses down to the transform limit, but the large amounts of higher order dispersion present will make external compression impossible. The dispersion of the antiresonant sample is relatively flat over a broad bandwidth around the design wavelength resulting in low values of GDD and higher order dispersion.

2.5.4 Gain sample characterisation

Different characterisation methods can be used to examine different aspects of a gain sample. Reflectivity measurements can be used to characterise the DBR, whereas photoluminescence measurements are used to examine the quantum well performance and the length of the active region. Finally, CW lasing performance can assess the performance of the structure as a whole.

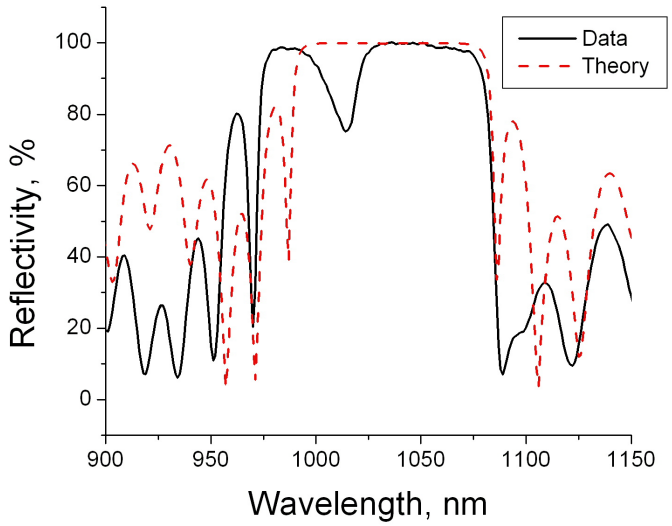

Figure 2.12: Measured and predicted reflectivity spectra for gain sample QT1544. Small errors in layer thickness have resulted in a slightly different centre wavelength. The dip in the stop band of the experimental spectrum is caused quantum well absorption being enhanced by a peak in the LCF spectrum.

The reflectivity of a gain sample, QT1544, is shown in figure 2.12 along with the

predicted reflectivity curve. The stop bands of the two curves can be seen to be centred at two slightly different wavelengths, but the stop band is wide enough that this will not prevent lasing. The dispersive characteristics of the DBR will be altered slightly, which may become important in modelocked operation.

The dip in the stop band is due to absorption in the quantum wells being enhanced at particular wavelengths by a peak in the LCF spectrum. This sample was designed to be antiresonant and should therefore have had a very flat LCF. This prominent dip is therefore an indication that the thickness of the microcavity could be incorrect. In fact, subsequent measurements found that the sample had been grown with a thicker spacer layer than intended, leading to a sharp peak in the LCF.

Reflectivity measurements can examine the DBR and can give some information about the LCF, but in order to assess the quantum wells photoluminescence (PL) measurements are required. PL measurements are spectral examinations of the photoluminescence emitted by the structure when pumped close to lasing conditions. PL is emitted into all angles by the quantum wells. Here, only the PL emitted from the sample surface, top PL, and the PL emitted from the sample edge, edge PL, are of interest. Top PL is of interest because photons emitted perpendicularly by the quantum well get caught in the sample microcavity. This introduces modulations to the top PL spectrum that are characteristic of the LCF of the sample. Edge PL is examined alongside top PL because it does not experience these modulations and therefore can be used to assess the quantum wells alone.

Figure 2.13 shows edge and top PL from sample QT1544 at 15 °C for different pump powers, with the pump laser focussed on to a 60 μm radius spot on the sample. An 850 nm long-pass filter was used to reduce the amount of pump radiation reaching the spectrometer. The edge PL can be seen to form a clean peak with a peak wavelength of 1015 nm. This is correct for a laser designed to operate at 1030 nm as a shift of approximately 15 nm is observed between the PL and lasing wavelengths.

The top PL has a distinctive peak at 1010 nm, but also has a series of smaller peaks trailing off to short wavelengths. These are the fringes of the microcavity etalon, and can be used to calculate an approximate thickness of 9.4 μm between the DBR and the sample surface.

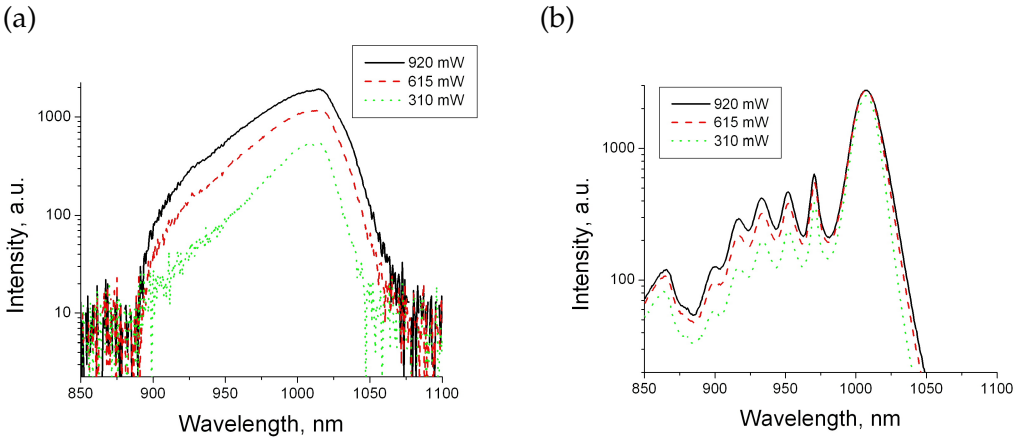

Figure 2.13: Edge (a) and top(b) photoluminescence spectra at 15 °C for different pump intensities. The edge PL has a peak wavelength of 1015 nm. The top PL shown modulations due to the etalon effect of the sample microcavity.

The final step in characterising a gain sample is to examine its CW lasing performance. Figure 2.14 shows the spectrum and the input/output power curve of a laser using sample QT1544 in a linear cavity with a 0.7% output coupler. The spectrum has a peak at 1040 nm, slightly longer than that predicted on the basis of the PL measurements. The input/output curve shows the power rising from a threshold power of 0.4 W with a slope efficiency of 21%. The laser reaches a maximum power of 123 mW at a pump power of 1000 mW. The curve doesn't roll off at high powers indicating that thermal rollover has not been reached.

These values of the efficiency and output power are sufficiently high that the laser will be able to tolerate the increase in loss caused by the insertion of a SESAM. The main factor that limits the output power of such a VECSEL is heating in the active region. Significant improvements can be made to both slope efficiency and output power by increasing the rate at which heat is removed from the active region. Techniques exist for either thinning the wafer down by removing the substrate, or bonding high thermal conductivity heatspeaders to the front surface of the sample.

Both of these methods have significant disadvantages for mode-locked VECSELs. Removing the substrate of a sample is inconvenient as it involves considerable post-growth processing, and using a crystalline heatspreader introduces an etalon to the laser cavity. This is not a significant problem for CW lasers but can severely restrict

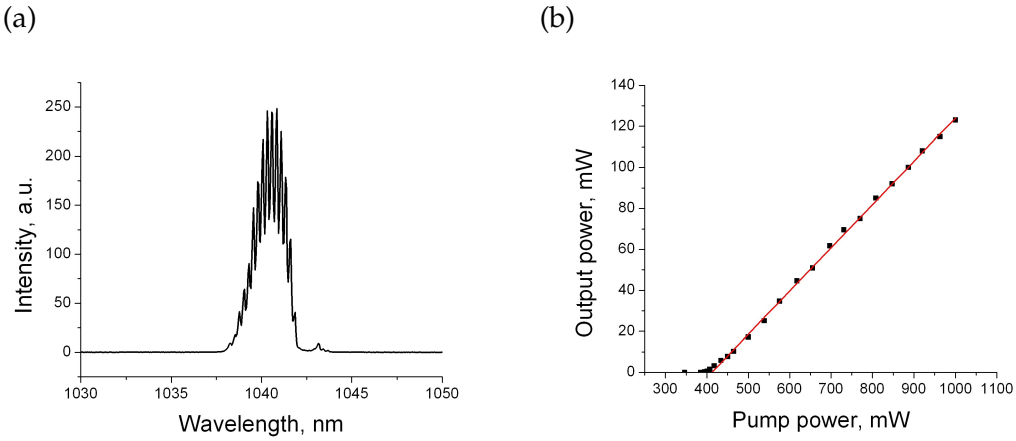

Figure 2.14: Optical spectrum (a) and input-output power curve for a CW VECSEL using gain sample QT1544. The spectrum shows a peak wavelength of 1045 nm and the input-output curve shows the laser reaching a maximum output power of 123 mW.

the bandwidth available for modelocking. The use of antireflection coated or angle polished heatspeaders can reduce the etalon effect. Throughout this work samples were used without any thermal management, resulting in low efficiencies and output powers but reducing the amount of sample processing required.

2.6 SESAM design

The design and characterisation of SESAMs for ultrashort pulse generation is described in detail elsewhere in this thesis (section 4.2.2, section 4.2.4). This section is therefore intended as a brief introduction to the major components of the type of SESAM used in this work, and not as a detailed description.

Figure 2.15 shows the major components of a SESAM. As with the gain sample, high reflectivity is provided by a multiple repeat DBR. This DBR may be identical to that used in the gain sample, or it may have a slightly offset centre wavelength if this gives better overall dispersion compensation. Saturable absorption is provided by a single quantum well. Maximum absorption will be achieved if the peak of the absorption spectrum coincides with the laser centre wavelength, but under certain circumstances, as described in section 3.2.3, shorter pulses can be achieved if they are offset. In the SESAMs used for ultrashort-pulse VECSEL modelocking the quantum well is

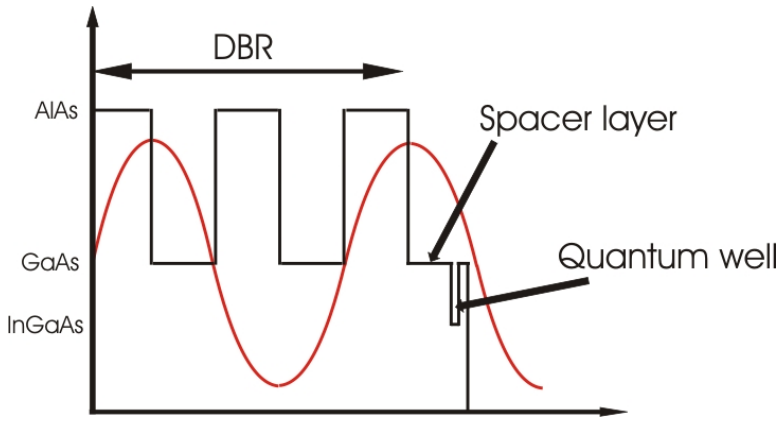

Figure 2.15: Typical SESAM used for VECSEL modelocking. A single quantum well is placed very close to the air interface with a spacer layer to control the size of the E-field at the quantum well position.

placed at the surface of the sample in order to take advantage of fast carrier recombination at surface defect sites. As with the gain sample, the spacing between the top of the DBR and the air interface is therefore crucial as it sets the magnitude of the E-field at the position of the quantum well. SESAMs with a higher E-field at the surface will have a higher modulation depth, but will also have higher non-saturable loss and less desirable dispersive characteristics, as described in section 4.2.4.

2.6.1 SESAM characterisation

As with the gain samples, SESAMs must be carefully characterised and their properties understood if the laser is to achieve its best performance. Reflectivity spectra can be measured to ensure that the DBR has been correctly grown, and that the reflectivity is sufficiently high at the design wavelength. Just as the absorption of the quantum wells in the gain sample caused a dip in the stop-band in figure 2.12, so the absorption of the quantum well in the SESAM will result in an absorption dip. As there is only a single quantum well in the SESAM, and as the magnitude of the electric field on the quantum well is significantly lower than in the gain sample, the absorption dip is much smaller.

Figure 2.16 shows the reflectivity of SESAM A4234. The absorption dip is shown in the inset, with a Lorentzian fit indicating an absorption resonance width of 32 nm. The absorption centre wavelength can also be found from this data to be 1028 nm. This

is of crucial importance if the VECSEL is to be mode-locked using the optical Stark effect (section 3.2.3), where the correct detuning between the absorption and lasing wavelengths is critical to achieving the shortest possible pulses. During laser operation this detuning can be varied by changing the SESAM temperature, thus shifting the absorption centre wavelength.

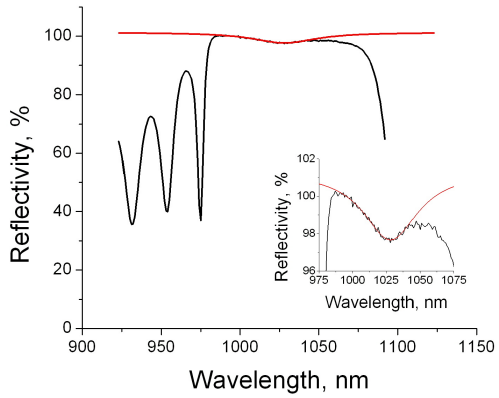

Figure 2.16: Reflectivity spectrum of SESAM A4234 with a Lorentzian fit to the quantum well absorption dip. Inset shows the absorption dip in detail

Several other SESAM parameters are of interest. The saturation fluence, F_{sat} determines how large a mode spot should be used on the SESAM. An accurate value of the saturation fluence is therefore essential to the design of the laser cavity. A second important parameter is the difference in loss between the bleached and unbleached states of the SESAM, referred to as the saturable loss, ΔR. This is important as it tells us about the strength of the absorber. A greater saturable loss results in a more pronounced difference between the bleached and unbleached states. For stable modelocking this must be large enough to switch the laser from a state where loss $>$ gain to a state where gain $>$ loss for the expected pulse fluences. Any real SESAM will also have a non-saturable loss, ΔR_{ns}, due to scattering losses etc. Clearly it is desirable to have as low a non-saturable loss as possible.

These three parameters can all be measured by firing laser pulses of varying intensity at a SESAM and measuring the difference in the reflectivity as a function of the pulse fluence. A graph of reflectivity versus pulse fluence can then be plotted, as shown in figure 2.17 for a SESAM designed for VECSEL modelocking at 850 nm. The

saturable loss can immediately be recognised as the difference between the reflectivity at low fluence and at high fluences. Likewise, the non-saturable loss is the difference between 100% reflectivity and the high fluence reflectivity. The saturation fluence is defined as the fluence at which the reflectivity has increased by 1/e (37%) of ΔR as defined by the equation [50]

$$R = \frac{R_{ns}}{S} \ln(1 + \frac{R_{lin}}{R_{ns}}(e^S + 1)), \tag{2.16}$$

where $R_{ns} = 1 - \Delta R_{ns}$, $R_{lin} = R_{ns} - \Delta R$ and the saturation parameter $S = F_p/F_{sat}$ where F_p is the pulse fluence. This equation can be used to fit the data in figure 2.17 allowing us to extract values of $F_{sat} = 107\mu J$, $\Delta R = 2.5\%$ and $\Delta R_{ns} = 2\%$ for this absorber.

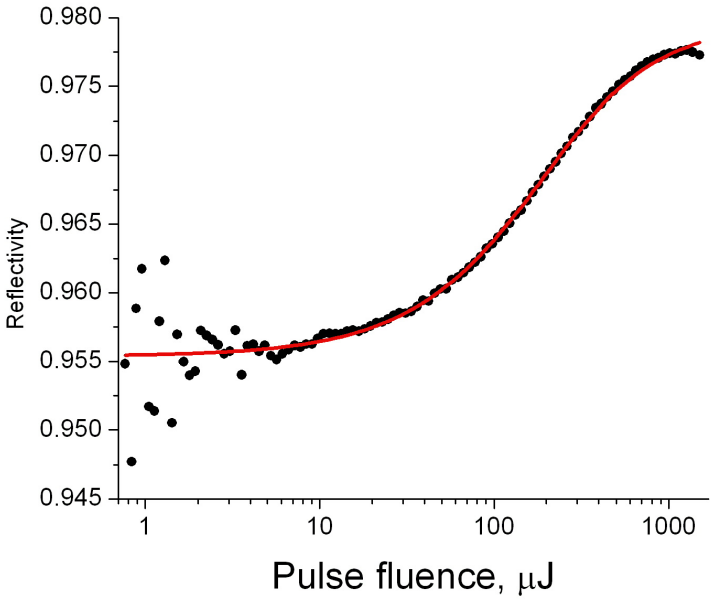

Figure 2.17: Saturation fluence measurement of an InP based SESAM designed for VECSEL modelocking at 850 nm. Fit parameters are $\Delta R_{ns} = 2\%$, $\Delta R = 2.5\%$ and $Fsat = 107\mu J$.

A fourth important parameter is the recovery time of the absorber, τ_r. When the absorber is bleached the absorbing elements are left in an excited state and cannot absorb further light until they have de-excited. This recovery will be brought about by different processes in different absorbers but will usually have the form of an exponential decay. The recovery time is then the time constant of this decay. Note that differ-

ent processes with different time constants can occur in the same absorber resulting in multi-exponential recovery curves. The recovery time of a SESAM depends on the material from which it is made and its structure, and just as the response time of an active modelocking element limits the pulse duration so the recovery time of a saturable absorber will limit the pulse duration of a passively mode-locked laser (This does not mean that pulses shorter than the recovery time cannot be produced. See section 3.2.2).

Recovery time is measured by pump-probe type experiments. Here an intense pump pulse bleaches the absorber before a weak probe pulse measures the reflectivity of the sample as a function of delay after the pump pulse. Figure 2.18 shows pump-probe data for a second SESAM designed for VECSEL modelocking at 855nm. Note that two recovery components can be seen. The spike at zero delay is a fast component whose response is below the resolution limit of the experiment. A slow component with an exponential recovery can also be seen. An exponential fit gives a recovery time of 227ps.

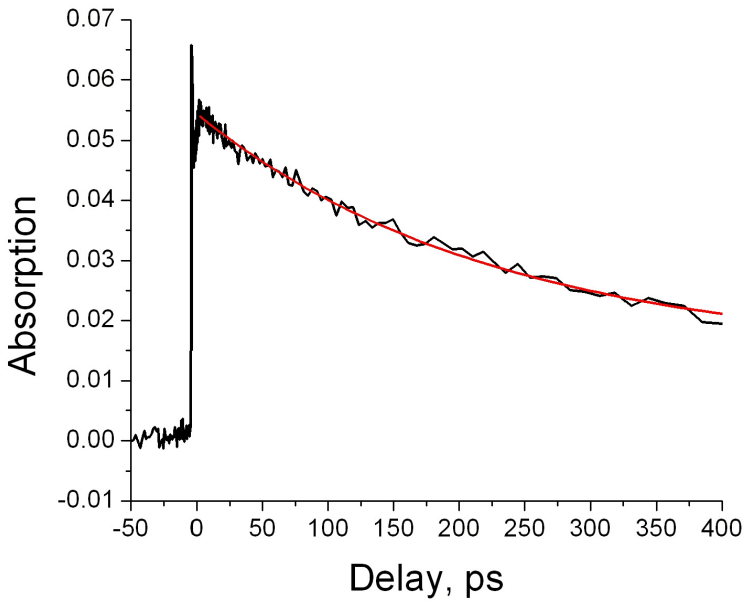

Figure 2.18: Pump-probe measurement of 855nm SESAM. An exponential fit gives a recovery time of 227ps.

Taken with the gain sample characterisation described above, these measurements allow one to design a suitable cavity for a modelocked VECSEL and to assess the oper-

ating conditions at which short pulses are likely to be generated.

2.7 Cavity designs for mode-locked VECSELs

There are several constraints placed on the cavity of a mode-locked VECSEL. Taken together these limit the range of cavities that are suitable for VECSEL modelocking.

One of the major constraints is that the cavity must have a tighter focus on the SESAM than on the gain sample. This is because, as described in section 3.2.2, in order to have stable modelocking the SESAM must saturate more quickly than the gain as a pulse passes through. This requires the laser to have a higher intensity on the SESAM for a given power level, and therefore a smaller mode area on the SESAM. We find empirically that stable modelocking is achieved with an area ratio of approximately 30.

The two other primary constraints on VECSEL cavities are caused by the upper state lifetime of the gain and the spot size and power available in the pump laser. The cavity length is restricted by the upper state lifetime. The time taken for a pulse to make one round trip must be significantly less than the upper state lifetime otherwise much of the gain will be lost as spontaneous emission. The upper state lifetime of our gain samples has not been measured, but we find that the efficiency of the laser starts to decrease in cavities longer than 60 cm.

The pump laser determines the possible range of mode areas on the gain sample. The pump lasers used in this work are all fibre coupled diode lasers with a core diameter of 60 μm. The minimum spot size on the gain is therefore also 60 μm diameter if 1:1 imaging optics are used to focus the pump. The maximum spot size is set by the point at which the carrier density generated by the pump is no longer high enough to reach lasing threshold and is therefore set by the available pump power.

Throughout this work 2:1 imaging optics were used to pump a 120 μm diameter spot on the sample. The mode area of the laser on the gain sample should be slightly smaller than the area of the pump spot. If the laser spot is too large then the mode will start to suffer loss where it extends beyond the pump spot, increasing the threshold and reducing slope efficiency. This is a more serious issue than the opposite situation, where the laser mode being smaller than the pump spot reduces the wallplug efficiency of the device and the maximum power, but doesn't compromise laser performance

significantly, though the wasted pump power will add slightly to the thermal load. In practice, the mode size in a particular laser is optimised to the value that gives the best threshold and output power.

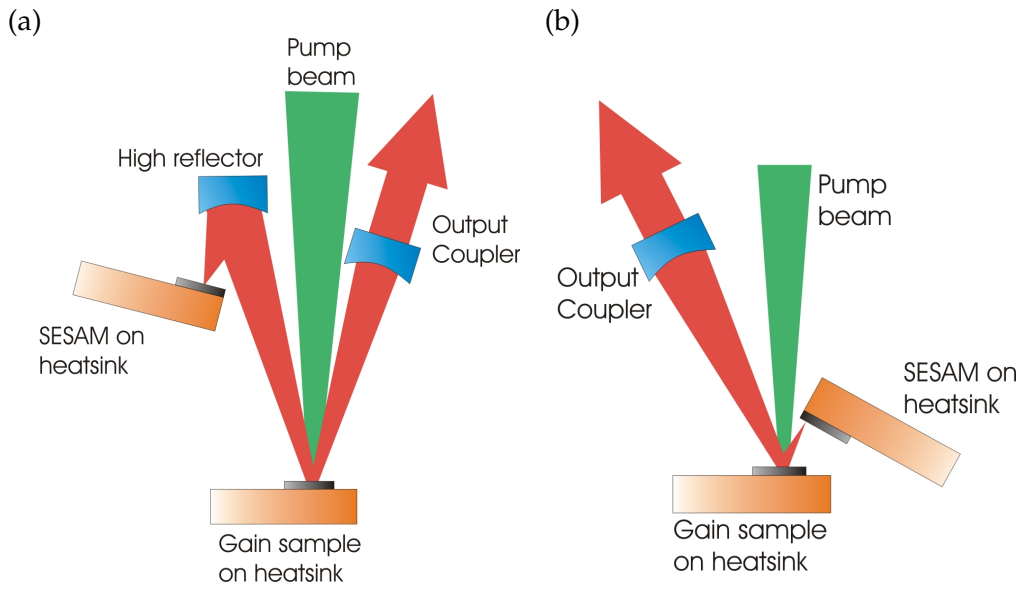

Figure 2.19: Two commonly used cavities for modelocked VECSELs. (a) Z-cavity, and (b) V-cavity. These types of cavities are used as they can give suitable ratios of spot sizes on the gain sample and SESAM. The cavities used throughout this work were Z-cavities with focal lengths of 50 mm for the output coupler and 25 mm for the high reflector.

Figure 2.19 shows the two most commonly used cavities. (a) is a 4-mirror Z-cavity, which is a suitable choice for lower repetition rate VECSELs. (b) is a V-cavity which is more compact and is therefore a better choice for higher repetition rates. All the lasers used in this work were Z-cavities with close to 1 GHz repetition rates. In this case the focal lengths of the cavity mirrors used are 50 mm for the output coupler and 25 mm for the high reflector.

The stability zones and mode sizes in this cavity can be calculated using transfer matrices. Figure 2.20 shows the mode sizes on the gain sample and SESAM for a 1 GHz Z-cavity as a function of the distance between the high reflector and the SESAM. We can use these curves to find the SESAM-to-high reflector distance at which the the mode size on the gain is matched to the pump spot and from this distance we can estimate the spot size on the SESAM.

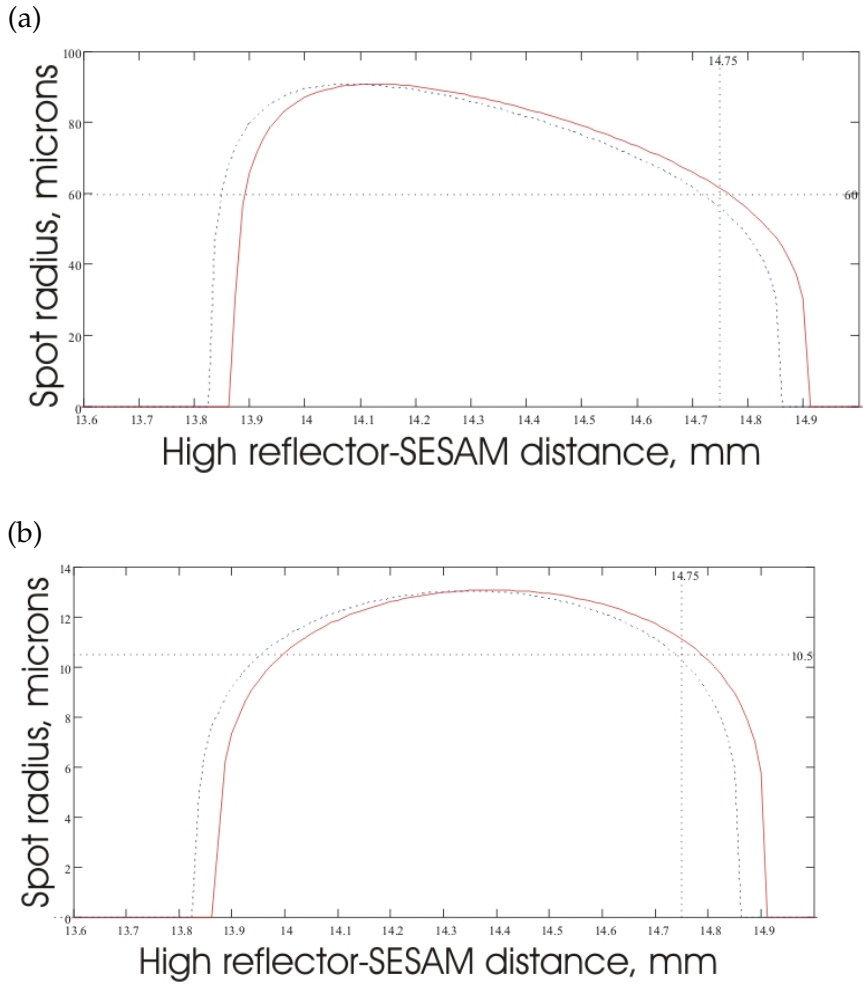

Figure 2.20: Spot sizes on the gain sample (a) and SESAM (b) calculated using transfer matrices for a 1 GHz Z-cavity. The approximate operating point of the lasers used in this work is shown by the crosshairs.

Chapter 3

Passive modelocking theory

3.1 Introduction

The cavity of a laser acts as an etalon, only allowing lasing at wavelengths corresponding to the fringes of the etalon. The wavelengths at which lasing is allowed are called the longitudinal modes of the laser. As the length of a laser cavity is typically several tens of centimeters the fringes will be very closely spaced, potentially allowing lasing on several thousand modes simultaneously. The optical field inside such a laser will therefore consist of several thousand standing waves with slightly different wavelengths. These standing waves will interfere with each other to produce peaks and dips in the laser intensity. If the relative phases of all the modes are locked together then the standing waves can be arranged such that they interfere constructively at a single point in space and interfere destructively elsewhere. This process, known as modelocking, results in an ultrashort pulse circulating in the cavity.

Modelocking works by introducing an element which modulates the loss of the cavity at the repetition rate of the laser. If the cavity loss is at a minimum at a particular time every round trip then a pulse will form at this low loss point. Modelocking systems can be divided into two categories depending on how the loss is modulated. In actively mode-locked lasers the loss is modulated by some active component which is driven by an external source whose frequency is matched to the cavity repetition rate. Active modelocking provides a very predictable and controllable modulation but is limited by the response times of the modulators. This generally limits the pulse

durations achievable from these systems to nanoseconds. Active modelocking also generally requires a complex system as the modulators used (typically acousto-optic modulators or electro-optic modulators) involve high frequency and often also high voltage electronics.

The alternative to active modelocking is passive modelocking, which is when the laser pulse itself is used to switch the modulator from its high loss state to its low loss state. Typically this involves the use of a saturable absorber. This is a component that will absorb light up to a certain threshold and then stop absorbing. A component with this property will exhibit a lower loss to a high intensity pulse than to a low intensity pulse, making it energetically favourable for the light to circulate in the cavity in the form of a short pulse.

In this chapter I will discuss several different regimes of passive modelocking that can be demonstrated by VECSELs modelocked by saturable absorbers.

3.2 Passive modelocking regimes

Lasers mode-locked using saturable absorbers can operate in several different regimes depending on the dynamic timescales of the gain and absorber, and on the dominant pulse shaping mechanism. Lasers operating in different regimes must be optimised for best performance in that regime. A clear understanding of the phenomena at work in each regime is therefore essential if one is to reach shorter pulse durations. Many different models have been used to describe passively mode-locked lasers. Here I focus on the models most applicable to the behaviour of mode-locked VECSELs.

3.2.1 Fast saturable absorber modelocking

Saturable absorbers can be categorised into 'fast' and 'slow' saturable absorbers. A fast saturable absorber is one whose recovery time is much shorter than the pulse duration, whereas for a slow saturable absorber the pulse duration is shorter that the absorber recovery time.

For a fast saturable absorber the degree of bleaching of the absorber, and therefore the decrease in loss, exactly follows the pulse profile. Figure 3.1 shows loss and gain

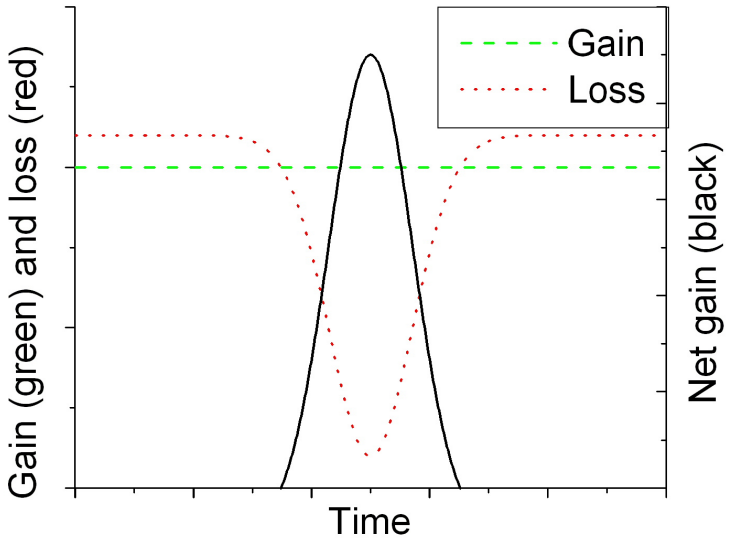

Figure 3.1: Schematic gain and loss curves as a function of time for a laser operating in the fast saturable absorber regime. The solid curve shows the net gain.

curves as a function of time for a fast saturable absorber. The passage of the pulse through the absorber can be seen to reduce the loss, opening a window of net gain and allowing a pulse to form. As the intensity is higher at the centre of the pulse than in the wings the centre of the pulse experiences less loss than the wings, resulting in pulse shortening. Figure 3.2 shows the net gain as a function of time as the pulse passes through the absorber. It is clear that the net gain is higher for the centre of the pulse than the wings, resulting in shortening.

For an ideal fast saturable absorber, i.e. one whose recovery is instantaneous, it is clear that this mechanism will continue to shorten the pulse indefinitely. In reality the absorber response will not be instantaneous, and there are also always pulse broadening effects present in a laser, most notably the finite gain bandwidth and the effects of dispersion. The final pulse duration of the laser will therefore be the duration at which the total shortening of the pulse per round trip due to the absorber is balanced by the total broadening per round trip from all broadening mechanisms. Due to the small thicknesses of material and the modest peak powers present in VECSELs, gain filtering is generally more important than dispersion.

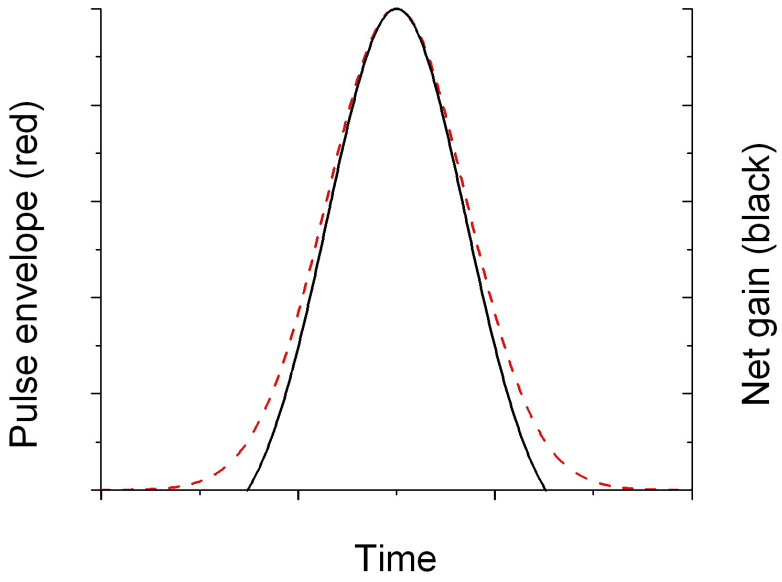

Figure 3.2: Schematic of the pulse envelope and net gain as a function of time for a fast saturable absorber.

This situation has been described by Haus [51], and analytical solutions for the pulse shape and the pulse duration in terms of the gain and absorber parameters have been found, given certain approximations. In addition to an ideal fast saturable absorber whose absorption coefficient could be evaluated from rate equations it was assumed that the gain had a parabolic frequency profile and that dynamic gain saturation did not occur. Finally, it was assumed that the pulse was only slightly altered by a single passage through any element.

In this situation the pulse profile was found to be a hyperbolic secant. The pulse duration, τ_p, can be related to gain and absorber properties by

$$\frac{1}{\omega_L \tau_p} = \left(\frac{g_0}{1+q} - 1 \right) \frac{q}{1+q} \frac{P_L}{4P_A} \omega_L T_P, \tag{3.1}$$

where ω_L is the laser bandwidth, g_0 is the small signal gain, q is the saturable absorber loss normalised to the cavity loss, P_L and P_A are the gain and absorber saturation powers and T_P is the round trip time.

3.2.2 Slow saturable absorber modelocking

In the slow saturable absorber regime the recovery time of the absorber is significantly longer than the pulse duration. As the pulse arrives the absorber becomes bleached and remains so, recovering over a period of many pulse durations. In this case it is the saturation of the gain that closes the window of net gain and allows a stable pulse to form. Figure 3.3 shows this process. First the absorber saturates as the pulse arrives, opening the window of net gain. The pulse then saturates the gain, depleting it to the extent where the window of net gain is closed. The gain will then also recover over a longer timescale depending on the pumping of the gain. Figure 3.3 demonstrates that the window of net gain can be much shorter than the recovery time of the absorber.

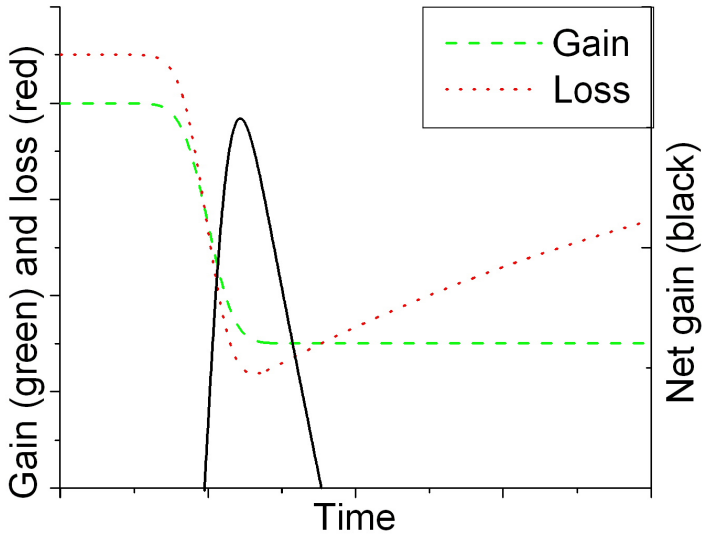

Figure 3.3: Schematic gain and loss curves as a function of time for a laser operating in the slow saturable absorber regime. The solid curve shows the window of net gain which, in this case, is approximately ten times shorter than the recovery time of the absorber.

It is clear that this modelocking regime will only be stable if the saturable absorber is saturated more quickly than the gain. In VECSELs this has important repercussions for the cavity design as discussed in section 2.7. Most mode-locked VECSELs use quantum wells for both the gain sample and the saturable absorber, and the two will tend therefore to have similar saturation fluences. It is therefore necessary to design a cav-

ity with a much tighter focus on the absorber than on the gain. This leads to a higher pulse fluence on the absorber than on the gain for the same laser power, meaning that the absorber will saturate first.

It is not immediately clear that symmetrical pulses will form in the slow saturable absorber regime as the SESAM absorbs power preferentially from the leading edge of the pulse. The trailing edge experiences very little absorption from the absorber, however the trailing edge also experiences lower gain as the gain has been partially saturated by the time it passes through, making the situation symmetrical.

It can be shown [52], that in the case where the absorber saturates much more quickly than the gain the net gain curve can be approximated by a parabola in the energy domain. In this case the pulse shape will again be a hyperbolic secant. Once again the pulse duration can be predicted from the laser parameters. If Ω_g is the gain bandwidth and E_p the pulse energy then the pulse duration is given by

$$\tau_p = \frac{f}{\Omega_g} \frac{1}{\sqrt{q} E_p}, \tag{3.2}$$

where f is a numerical factor between $9/16$ and $25/16$ depending of the height of the net gain parabola.

3.2.3 Optical Stark effect modelocking

The optical Stark effect is the instantaneous wavelength shift of an absorption peak due to the presence of an intense optical field. In the case of a semiconductor quantum well this blueshift arises from the Coulomb interaction between the real exciton absorption resonance and virtual excitons created by the optical field. As the virtual excitons are only present for the duration of the pulse the absorption recovers instantaneously once the pulse has passed. Experimental studies of the optical Stark effect in GaAs/AlGaAs quantum wells, for example [53], have shown shifts of $\sim$3 nm for applied pulse intensities of 10^9 - 10^{10} W/cm^2. This is similar to the peak intensities achieved within VECSEL cavities and, while these measurements were performed at 15 K, it is not unreasonable to expect similar shifts at room temperature.

The shift of the absorption peak with electric field can be used as a saturable absorption. If the absorber is designed in such a way that the intense electric field of

a laser pulse shifts the absorption peak away from the laser wavelength then the absorption experienced by the laser will decrease. Figure 3.4 illustrates this. The red line shows the absorber resonance without the optical field and the green line shows the Stark-shifted resonance. The change in absorption is shown in black, and is negative over a wavelength range on the long wavelength side of the resonance. It is clear that a laser whose wavelength lies within this region will experience a decrease in absorption caused by its own intensity. The response time of the OSE is near-instantaneous, meaning that an OSE modulator will be a near-perfect fast saturable absorber.

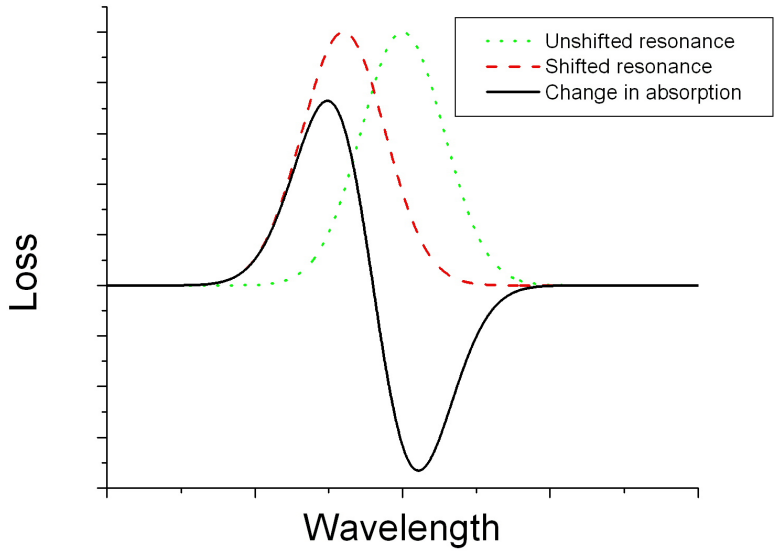

Figure 3.4: Unshifted and Stark shifted absorption resonances. The solid line shows the change in the loss due to the Stark shift.

More intense pulses will cause a greater shift, resulting in a larger change in absorption. An OSE absorber will therefore become more efficient as the pulses get shorter. However, it does not follow that a Stark effect saturable absorber can continue to shorten pulses indefinitely. Figure 3.4 clearly shows that the bandwidth over which there can be a saturable absorption is limited by the width of the absorber resonance, which is set by the dephasing time of the carriers in the quantum well. Modelling of a Stark effect absorber [54] implies that the Stark effect can shorten pulses down to a limit of twice the dephasing time of the medium.

3.2.4 Quasi-soliton modelocking

In a passively mode-locked laser, quasi-soliton modelocking can provide a further pulse shortening mechanism in addition to conventional saturable absorption [55, 56]. Quasi-soliton modelocking can occur when the GDD in the laser cavity has the opposite sign to an intensity-dependent second-order dispersion. Pulse shortening can occur in this case when the intensity-dependent dispersion results in a spectral broadening of the pulse, followed by compression to a new minimum pulse duration by the action of the fixed GDD. This effect can produce pulse shortening but cannot prevent the amplification of noise in the cavity. A quasi-soliton mode-locked laser therefore also requires a conventional saturable absorber to stabilise the laser against CW lasing. This modelocking mechanism has been used to good effect in several types of passively mode-locked ultrafast lasers, most notably dye lasers [57] and Ti:sapphire lasers [58], producing pulse durations of tens of femtoseconds.

In quasi-soliton mode-locked Ti:sapphire lasers the intensity-dependent dispersion is provided by self-phase modulation (SPM) resulting from the intensity-dependent refractive index modulation of the Kerr effect in the gain medium. This produces dispersion with a negative sign, which must be compensated by a positive intracavity dispersion, usually provided by using an intracavity prism pair. Neither of these dispersion sources are suitable for use in passively mode-locked VECSELs. The Kerr effect is negligible in such a laser as, despite the relatively high Kerr coefficient of GaAs and the tight focusses on both the gain sample and the SESAM, the pulses pass through such a small thickness of material that the total phase shifts are small. Prisms are not a suitable source of GDD due to their insertion losses and the short lengths of VECSEL cavities.

The refractive index of GaAs near the band edge is a strong function of carrier density. A laser pulse passing through a VECSEL gain sample will therefore experience significant SPM from the refractive index change as the carrier density is rapidly reduced by stimulated emission. In order to compensate for this negative dispersion, positive GDD can be provided by the multilayer structures of the gain sample and the SESAM, illustrating the importance of the correct choice of DBR centre wavelength and microcavity thickness discussed in sections 2.5.1 and 2.5.3.

One significant disadvantage of these sources of dispersion is the difficulty in changing their values. Optimal dispersion in the Ti:sapphire system described above can be found by changing the amount of GDD introduced by the prism pair. In a VECSEL tuning can be achieved by adjusting the temperatures of the gain sample and SESAM in order to shift the laser wavelength to give the correct GDD from the samples, and by changing the pump power to adjust the pulse energy to give an appropriate amount of SPM. None of these are independent however. Changes to any of these parameters will also change other properties of the laser.

Some contribution to pulse shortening due to quasi-soliton modelocking is to be expected in any VECSEL where the sample GDD is positive. It is difficult to assess the degree of pulse shortening due to this mechanism however, due to the difficulty in independently adjusting either the GDD or the SPM in a VECSEL cavity. Regardless, this discussion serves to illustrate the importance of correct dispersion compensation in mode-locked VECSELs. A simple consideration of the effects of the gain and SESAM on the pulse amplitude is not sufficient. Correct dispersion compensation can give pulse shortening, whereas very large values of total dispersion will cause significant pulse broadening and chirp.

Chapter 4

Sub-picosecond pulse generation and sample design

4.1 Introduction

In this chapter I will describe recent progress in the production of short pulses from mode-locked VECSELs, in particular the description of trains of multiple 70 fs pulses, and of the changes in sample design that have made them possible. A characterisation of the pulse train regime is presented, along with a brief theoretical description, and possible ideas for future sample designs are discussed.

The first VECSEL sample pair to produce sub-ps pulses were gain sample QT1544 and SESAM QT1627. These samples were grown by metal-organic chemical vapour deposition (MOCVD) by John Roberts at the National III-V Facility in Sheffield. Structures of the two samples are described below. The other samples described in this chapter, gain sample A4226 and SESAM A4234, were grown by molecular beam epitaxy (MBE) by Ian Farrer of the University of Cambridge. The 260 fs VECSEL characterisation and the modelocking onset measurements for the 500 fs VECSEL were performed by Keith Wilcox.

4.2 Sample design for short pulse generation

Understanding how to design suitable samples is crucial to the modelocking of the broad bandwidths that are necessary for the generation of femtosecond pulses. In this section I will describe the necessary features of the design, the evolution of both gain samples and SESAMs and the performance of the resulting lasers.

4.2.1 Gain sample QT1544

The structure of sample QT1544 is shown in figure 4.1. The sample consists of a 27.5 repeat GaAs/AlAs DBR grown on a GaAs substrate. This gives a stop band with a width of nearly 100 nm with a reflectivity at the centre wavelength of over 99.99%. Above the DBR is the active region which consists of a thickness of $7/2\lambda$ of pump absorbing GaAs whose thickness is chosen so that there are six antinodes of the electric field in the active region.

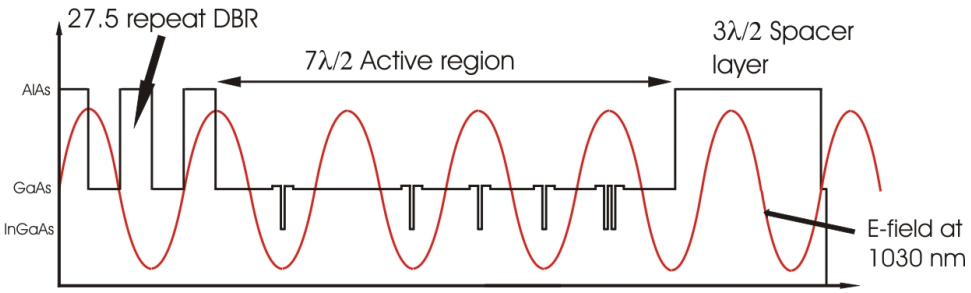

Figure 4.1: Layer structure of gain sample QT1544.

Within the GaAs are six $In_{0.25}Ga_{0.75}As$ quantum wells, designed for emission at 1025 nm, surrounded by $GaAs_{0.94}P_{0.06}$ strain compensation layers. The quantum wells are placed asymmetrically at the antinodes of the electric field in the active region, with two quantum wells under the first antinode and no quantum well under the second-to-last antinode. This spacing is chosen as more pump light is absorbed near the surface resulting in an unequal carrier density through the active region. By placing more quantum wells near the surface we ensure that the number of carriers in each quantum well is approximately equal.

The thicknesses of the active region and spacer layer of QT1544 were designed to give an antiresonant microcavity but the spacer layer was grown thicker than intended,

giving a slightly off-antiresonant sample. The longitudinal confinement factor of this sample was therefore between resonant and antiresonant, as described in section 2.5.4, resulting in a sample with some restriction on the lasing bandwidth but not as much as a resonant sample. The dispersion curve of this sample was also steeper than intended, imparing the sample's ability to produce short pulses. Figure 4.2 shows the LCF (a) and dispersion curves (b) of QT1544 and an ideal antiresonant sample calculated using the same transfer matrix method as described in section 2.5.1. It is clear that the antiresonant sample has flatter LCF and dispersion curves near the design wavelength.

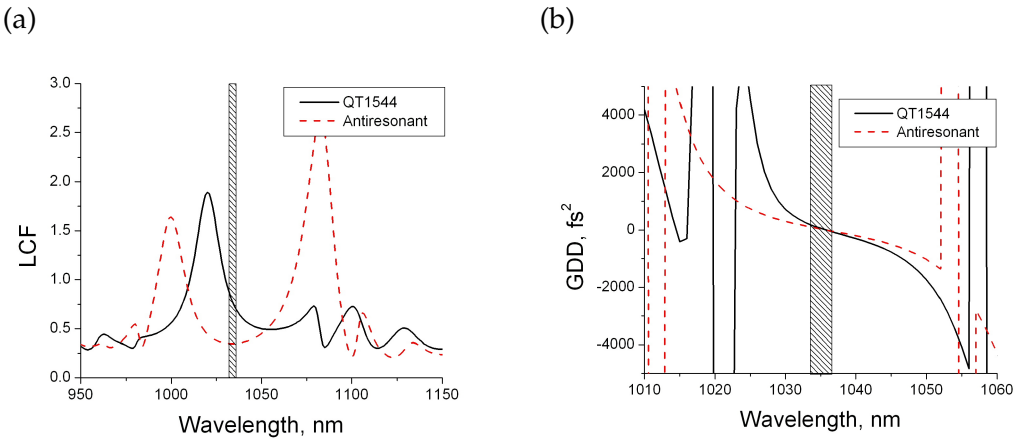

Figure 4.2: Theoretical longitudinal confinement factors (a) and GDD curves (b) for QT1544 and an ideal antiresonant sample. The hatched region indicates the design wavelength.

The six $In_{0.25}Ga_{0.75}As$ quantum wells are not lattice matched to the substrate, resulting in a sample with overall compressive strain. In sample QT1544, degradation of the sample is prevented by using layers of $GaAs_{0.94}P_{0.06}$ either side of the quantum wells to compensate for the strain in the quantum well.

4.2.2 SESAM QT1627

As dicussed in chapter 3, pulse durations produced by a passively mode-locked laser are limited by the recovery time of the absorber. It is therefore desirable to have a SESAM with the shortest possible recovery time. Various methods can be used to decrease the recovery time, however the most commonly used techniques also result in higher non-saturable losses which, while acceptable in higher gain solid state lasers,

cannot be tolerated by low gain VECSELs.

The recombination time for carriers in a typical InGaAs quantum well, surrounded by bulk GaAs, is of the order of a few nanoseconds. Methods for increasing the rate of recombination rely on introducing defects to the crystal lattice around the quantum well, as carriers can scatter off these defects and recombine several orders of magnitude more quickly. The most common method used in SESAMs is low temperature growth, which can reduce the recovery times from nanoseconds to picoseconds, but at the expense of increased scattering losses [59, 60].

Other methods have been used to introduce defects without such large increases in loss. If the quantum well is grown very close to the surface of the SESAM then carriers generated in the quantum well can tunnel through the potential barrier and recombine at defect sites on the surface of the sample. This method does increase the losses of the SESAM, as it means that the SESAM must be designed so as to have a large value of the electric field on its surface. This results in increased scattering losses from surface defects, however for a suitably high quality surface these losses can be small enough for a VECSEL to tolerate.

QT1627 was designed to use both surface recombination and the Stark effect (see section 3.2.3). The sample was grown with a DBR similar to that of sample QT1544. On top of the DBR a spacer layer 42 nm thick was grown in order to set the value of the electric field on the quantum well to be 20% of the electric field outside. The spacer layer thickness is instrumental in setting the modulation depth of the SESAM, which was found by saturation fluence measurements to be 0.3%. The quantum well had a design wavelength of 1020 nm and was covered by a 2 nm thick layer of GaAs. The layer structure of QT1627 is shown in figure 4.3.

The design wavelength was shorter than the intended laser wavelength in order to use the optical Stark effect for modelocking, as described in section 3.2.3. Figure 4.4 shows the calculated electric field as a function of position in the sample and also the dispersion of the sample and the squared electric field on the quantum well as a function of wavelength. A thinner spacer layer leads to a larger electric field on the quantum well, but as the spacer layer gets thinner the sample becomes more resonant and both the dispersion caused by the sample and the loss due to surface scattering

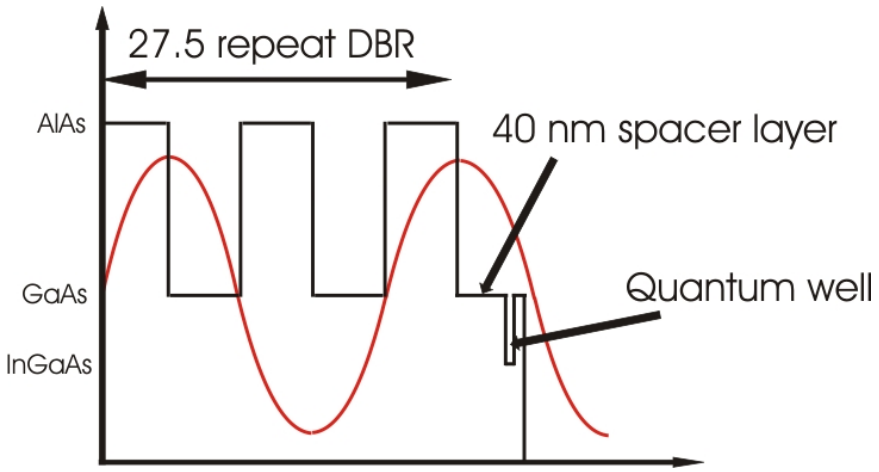

Figure 4.3: Layer structure of SESAM QT1627.

increase. The thickness of the spacer layer was therefore chosen carefully in order to give as large an electric field overlap as possible without either increasing the surface scattering losses beyond what was tolerable or introducing too much dispersion.

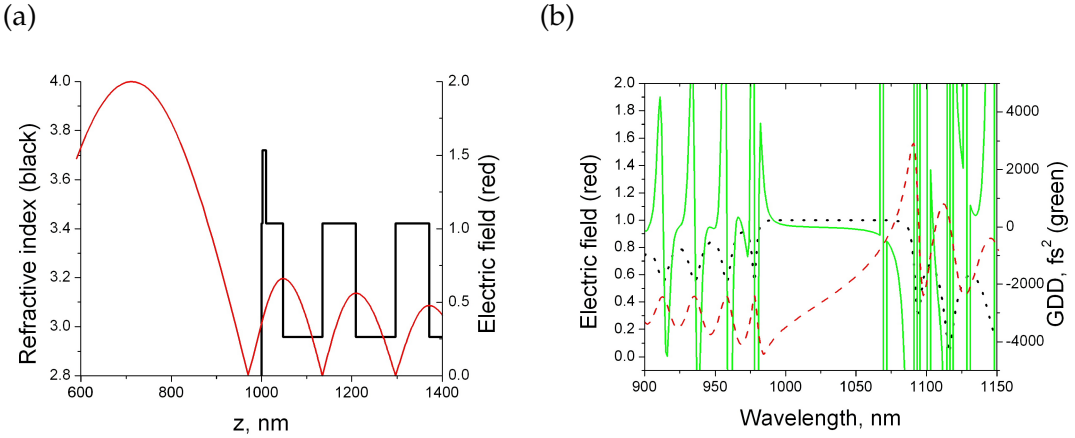

Figure 4.4: (a) Calculated electric field as a function of position inside SESAM QT1627. (b) Calculated electric field (dashed line) and GDD (solid line) as a function of wavelength. The dotted line shows the stop band of the DBR for reference.

4.2.3 500 fs pulses using samples QT1544 and QT1627

The combination of samples QT1544 and QT1627 has been shown to produce pulses as short as 450 fs when operating in the Stark regime [39, 42]. In this regime the gain sample temperature is adjusted so that the laser wavelength is detuned to the long wa-

velength side of the absorbing resonance as described in section 3.2.3. Figure 4.6 shows the autocorrelation and optical spectrum of a laser operating in this regime. Stark mode-locking has been demonstrated with these samples in cavities with repetition rates from 300 MHz to 10 GHz. In the laser presented here the cavity used was a 4-mirror Z-cavity of length 15 cm as described in section 2.7. This cavity gives waists of radius 60 μm on the gain sample and 10 μm on the SESAM. A 0.7% output coupler was used giving an output power of 40 mW. Figure 4.5 shows a schematic of the typical laser cavity along with the set-up used to measure optical spectra and autocorrelations.

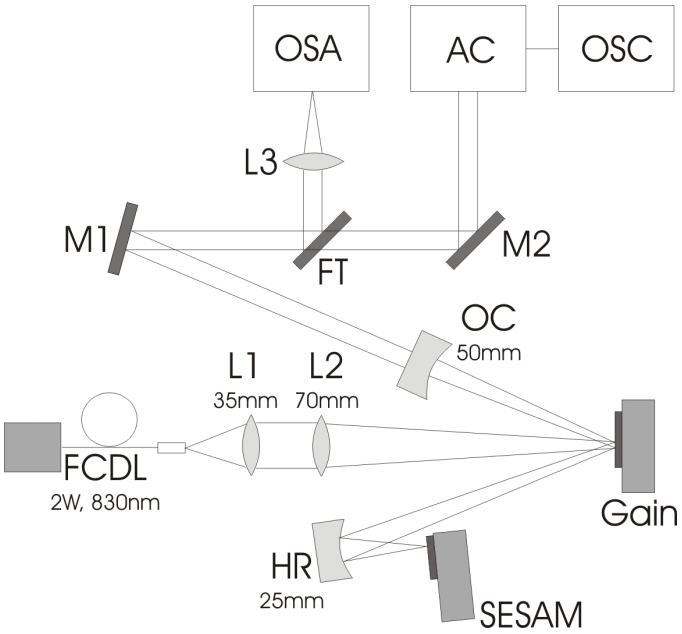

Figure 4.5: Schematic of a typical laser cavity and the set-up used for measurements of optical spectra and autocorrelations. OSA=optical spectrum analyser, AC=second harmonic autocorrelator, OSC=oscilloscope, M=metal mirror, L=lens, FT=flip-top mirror, OC=output coupler, HR=high reflector, FCDL=fibre-coupled diode laser. Gain sample and SESAM are mounted on temperature-controlled copper blocks.

The pulse duration is determined by the point at which the shortening per round trip in the SESAM is balanced by the pulse lengthening caused by the gain filtering effect discussed in chapter 3. This implies that there are two routes to shorter pulses: either increase the shortening per round trip by increasing the modulation depth of the SESAM or decrease the gain filtering by designing a gain sample with a flatter gain spectrum.

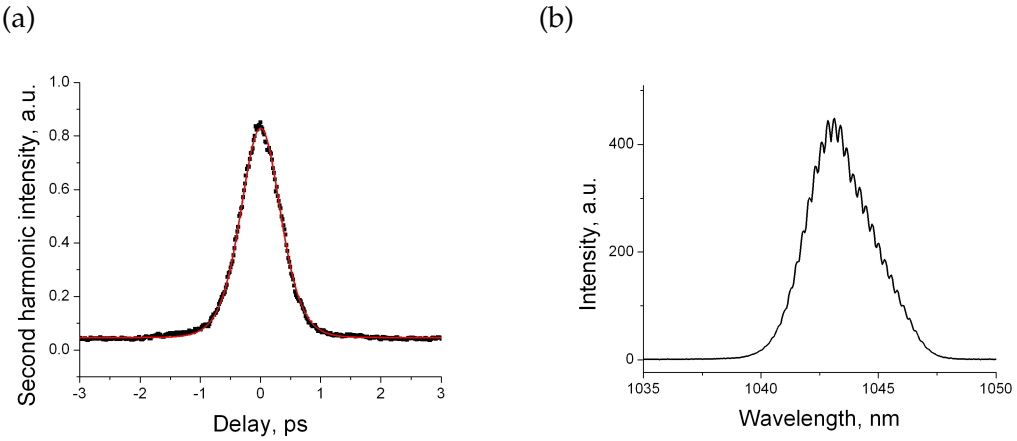

Figure 4.6: Second harmonic autocorrelation and optical spectrum of a laser producing 508 fs pulses. A sech squared fit to the autocorrelation gives a pulse duration of 508 fs and the optical spectrum has a bandwidth of 2.86 nm.

We can estimate the contributions from different pulse broadening and narrowing sources. If we assume that the gain coefficient can be approximated by a parabola with width σ_ω and central frequency ω_0 [61],

$$\alpha(\omega) = \alpha_0 \left(1 - \frac{(\omega - \omega_0)^2}{2\sigma_\omega^2}\right), \tag{4.1}$$

near the laser wavelength then, for an input pulse of length τ_0 the duration of the output pulse will be

$$\tau = \tau_0 \sqrt{1 + \frac{2\ln 2 \ln G_0}{\tau_0^2 \sigma_\omega^2}}, \tag{4.2}$$

for an intensity gain of G_0. Estimating a single-pass gain of 1.02 and a gain bandwidth of 16 nm gives a single-pass broadening of $\tau = \tau_0 \times 1.00006$ or a round trip broadening of

$$\tau = \tau_0 \times 1.00012. \tag{4.3}$$

The shortening per round trip due to the SESAM can be found experimentally from modelocking build up measurements. In these measurements the cavity is blocked by a chopper. When the cavity is unblocked the fundamental and second harmonic of the output are recorded as a function of the time after unblocking. The cavity fills with photons very quickly, so the fundamental signal rises very quickly and the pulses settle to their final energy, U. The second harmonic is proportional to U^2/τ, and rises more

slowly as the pulse duration decreases. Figure 4.7 shows the fundamental and second harmonic signals (a) and a plot of the fundamental signal squared over the second harmonic (b). This curve is proportional to τ/τ_0 and can be fit by an exponential decay from which one can extract the shortening per round trip. After one round trip a pulse with an initial duration of τ_0 will have a pulse duration of

$$\tau = \tau_0 \times 0.99987. \tag{4.4}$$

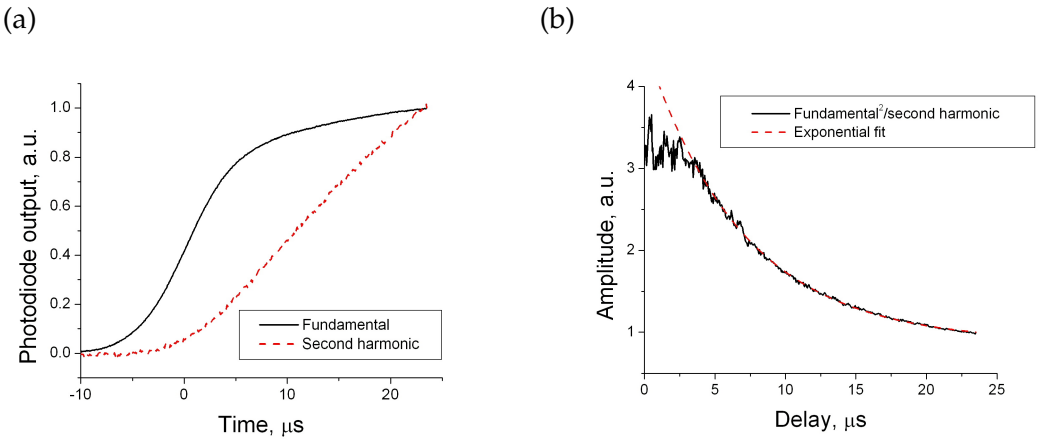

Figure 4.7: Modelocking rise time data (a) shows the fundamental signal increasing quickly as light fills the cavity and the second harmonic increasing more slowly as the pulse duration decreases. The curve plotted in (b) is proportional to the pulse duration and decreases exponentially as the pulse duration tends towards its final value.

The third major factor affecting pulse duration is dispersion. If, having taken into account gain dispersion, we attribute the remaining broadening to second order dispersion we can calculate the magnitude of the intracavity dispersion but not its sign. Given a GDD of G and a nearly transform-limited pulse,

$$\tau = \tau_0 \sqrt{1 + \left(\frac{G}{\tau_0^2}\right)^2}. \tag{4.5}$$

From this we can calculate $|G|$=1400fs^2. It is possible to calculate the GDD per pass on a sample from a multilayer calculation on the structure. Using this method we estimate the GDD per pass on the gain sample to be 600 fs^2 and -100 fs^2 on the SESAM, giving a total GDD of 1100 fs^2 per round trip. GDD from the samples can therefore

account for most of the observed GDD, though some additional dispersion may result from nonlinear effects in the laser. It should be noted that this calculation can only be expected to give very approximate values of the dispersion due to the difficulties in estimating several of the parameters involved, in particular, the gain and the gain bandwidth.

4.2.4 High modulation depth Stark SESAM A4234

As discussed in section 4.2.2, the modulation depth of a SESAM depends on the value of the electric field on the quantum well which, in turn, depends on the thickness of the spacer layer. A second Stark SESAM was designed, with a spacer layer thickness of 13.5 nm giving a modulation depth of 0.7%, more than double that of QT1627. The sample, A4234, was grown by molecular beam epitaxy (MBE) by Ian Farrer in Cambridge. Figure 4.8(a) shows the electric field as a function of position in the structure. Note that the amplitude of the electric field at the position of the quantum well in this structure is 44% of the field outside, compared to 20% for QT1627, as shown in figure 4.4. Figure 4.8 (b) shows the electric field as a function of wavelength and the GDD of the sample. This again shows the higher values of the electric field in this sample, but also that the thinner spacer layer has resulted in a steeper GDD curve. The increased losses due to surface scattering were partially offset by the higher surface quality of material grown by MBE compared to MOCVD.

When used with QT1544 the high modulation depth SESAM did indeed give shorter pulses. Figure 4.9 shows the autocorrelation and optical spectrum of a train of 280 fs pulses produced by these samples when used in a cavity identical to the one in section 4.2.3.

4.2.5 High bandwidth gain sample A4226

The 280 fs and 500 fs pulse duration VECSELs described in the previous sections have only managed to access a small fraction of the available gain bandwidth, 2.86 nm and 4.5 nm respectively, while the available gain bandwidth has been measured to be 32 nm FWHM using spectro-temporal methods [62]. One factor limiting the bandwidth used is the longitudinal confinement factor (LCF) of the samples used. The LCF strongly

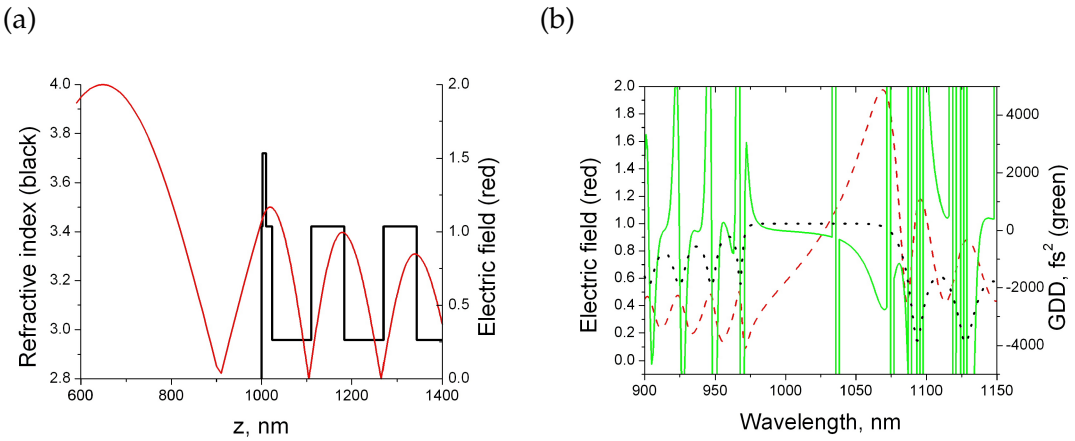

Figure 4.8: (a) Electric field as a function of position in sample A4234. (b) Electric field(dashed line) and GDD(solid line) as a function of wavelength. The dotted line shows the stop band of the DBR for reference.

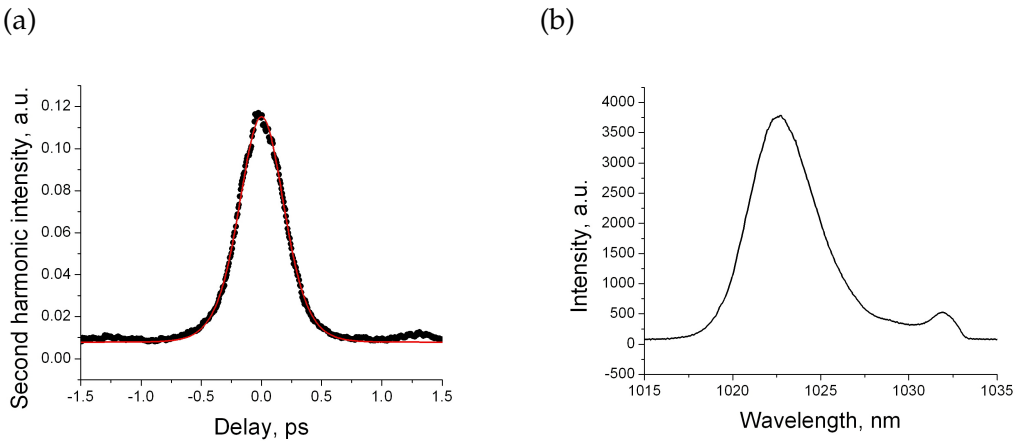

Figure 4.9: Second harmonic autocorrelation and optical spectrum of a laser producing 280 fs pulses. A sech squared fit to the autocorrelation gives a pulse duration of 280 fs and the optical spectrum has a bandwidth of 4.5 nm making the pulse 1.1 times transform limited.

affects the gain bandwidth as the laser will experience higher gain when there is a good overlap between the E-field and the quantum wells. The laser will therefore tend to operate at wavelengths where the LCF is highest. As described in section 2.5.3, the LCF can be maximised for a particular wavelength by designing the gain sample to be resonant at that wavelength, however this leads to a very sharp peak in the LCF spectrum which leads to a restriction in the bandwidth. For modelocking the ideal sample design is antiresonant as this gives the flattest possible LCF, leading to a broader gain bandwidth. In practice, this bandwidth comes at the price of reduced gain.

Sample QT1544, the gain sample used to achieve 500 fs pulses and 280 fs pulses was originally intended to be antiresonant but was misgrown, resulting in a sample with a thicker capping layer than intended. This made the sample slightly off-antiresonant as shown in figure 4.10. A second sample, A4226, was subsequently grown to a similar design to give a truly antiresonant gain sample. This second sample was grown by MBE rather than MOCVD. MBE is a more precise growth method which allows for finer control of layer thickness and gives a higher surface quality, resulting in lower scattering losses, but unfortunately, using this machine it was impossible to use phosphorus in the strain compensation layers. This resulted in a sample with overall compressive strain, which reduced the lifetime of the sample.

Figure 4.10 also shows the measured reflectivity spectra of samples QT1544 and A4226 and the typical bandwidth over which lasing is observed. The dip in the stop band of the reflectivity spectrum is caused by absorption in the quantum wells and is an approximate measure of the gain spectrum. It is clear that the flatter LCF of A4226 has resulted in a much less pronounced dip in the spectrum and therefore in a flatter gain bandwidth. Note that the absorption dip, the LCF and the lasing bandwidth do not line up. This is because the LCF and reflectivity data are calculated or taken at low excitation and at room temperature. Under laser operating conditions the quantum well PL and the microcavity dip would both be shifted towards longer wavelengths by both increased temperature and carrier density but at different rates.

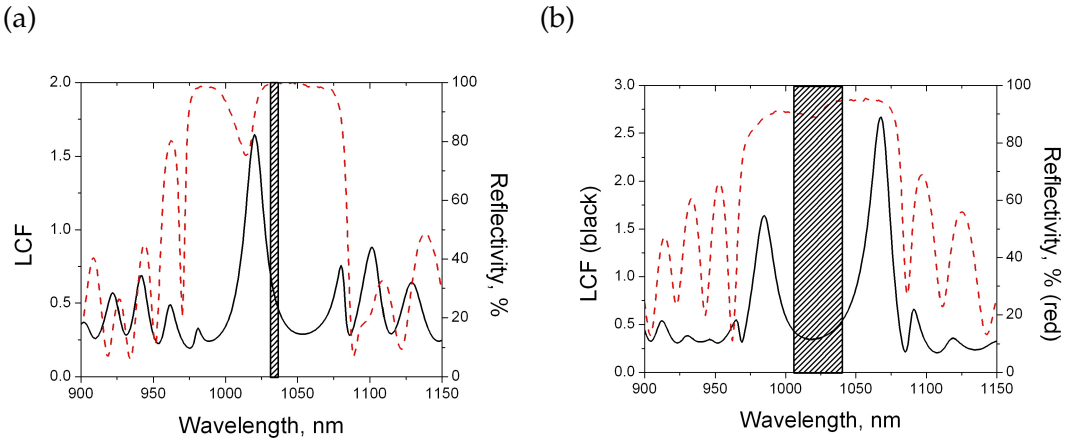

Figure 4.10: Theoretical Longitudinal Confinement Factors (solid line) and measured reflectivity spectra (dashed line) for samples QT1544 (a) and A4226 (b). The hatched box shows the typical bandwidth over which lasing occurs.

4.3 Lasers using samples A4226 and A4234

The combination of an antiresonant gain sample with a high modulation depth SESAM should allow Stark modelocking to occur over a larger bandwidth, thus producing shorter pulses. In fact, by changing the cavity configuration and by tuning the temperature of the gain sample it was possible to access three different regimes of modelocking using this sample combination.

If an intracavity etalon was used to restrict the available bandwidth then the laser gave 3 ps pulses with an optical spectrum that was tunable over a 14 nm range. Without the etalon restricting the bandwidth it was possible to see two different modelocking regimes. One was the familiar Stark modelocking regime, giving a single transform limited 300 fs pulse per round trip.

In the third regime the laser output consisted of trains of up to 70 pulses with durations as short as 70 fs and separated by between 300 fs and 1100 fs. The pulse shaping in this regime is still attributed to the optical Stark effect, but as the pulse duration drops below the carrier-phonon scattering time of the gain, the dynamic regime becomes strongly influenced by nonlinear gain saturation. This results in multiple pulsing as a single pulse can no longer extract all the energy stored in the gain.

All three regimes were investigated using the same 4-mirror cavity, similar to the ones used in sections 4.2.3 and 4.2.4. The total cavity length was 15 cm giving a repe-

tition rate of 1 GHz. The radii of the laser mode on the gain and SESAM respectively was 60 μm and 8 μm. An output coupling of 0.3% was used. The first two regimes are discussed briefly in the next two sections. The pulse train regime is discussed in detail in section 4.3.3.

4.3.1 Highly tunable picosecond laser

Lasers operating using gain sample A4226 and SESAM A4234 were found to be very spectrally versatile. This is to be expected given the flat gain profile of the sample, and is desirable in terms of short pulse generation, but it also meant that the laser was prone to operating in several different spectral regions with different regions corresponding to different behaviours. An etalon was therefore used in an attempt to restrict the available bandwidth allowing us to investigate one spectral region at a time. The constraints on the etalon are very severe if the transmitted bandwidth is to be large enough to produce sub-picosecond pulses. The most suitable commercially available solid core etalons were 25 μm thick fused silica etalons from Lightmachinery with a finesse of 0.7 and a free spectral range of 4023 GHz or 14.2 nm at 1030 nm.

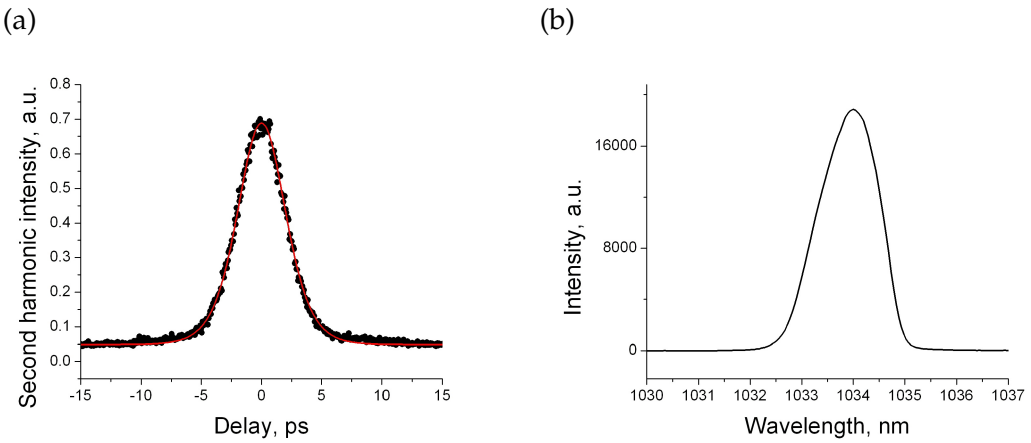

Figure 4.11: Autocorrelation (a) and optical spectrum (b) of pulses from a laser built using samples A4226 and A4234. A sech squared fit to the autocorrelation gives a pulse duration of 3.1 ps and the optical spectrum has a bandwidth of 1.4 nm.

One of these etalons was mounted in the cavity with its angle close to Brewster's angle. The angle of the etalon was adjustable so that the desired wavelength could be selected by changing the angle of the etalon and therefore its effective thickness. The

laser was found to give stable modelocking, with a sech-squared-fit pulse duration of 3.1 ps and a bandwidth of 1.4 nm corresponding to 3.9 times transform limited. By adjusting the angle of the etalon it was possible to tune the centre wavelength of the spectrum over the entire FSR of the etalon, 14.2 nm. This indicates that the SESAM can provide a saturable absorption over a wavelength range at least this broad. Figure 4.11 shows the autocorrelation and spectrum of the laser. As the etalon angle was shifted the autocorrelation remained the same and there was no observable change to the spectrum other than its centre wavelength. The insertion of the etalon increased the loss of the cavity, increasing the lasing threshold from 0.35 W to 0.55 W and decreasing the output power from 20 mW to 10 mW.

4.3.2 300 fs Stark mode-locked laser

Stark modelocking is only observed when the laser wavelength is detuned to the long wavelength side of the absorbing resonance by the correct amount. If the detuning is too large then the absorption will be too weak to sustain stable modelocking. If the laser is operating near the peak of the absorption spectrum then there will be little change in the absorption due to the Stark effect and therefore little pulse shortening. Using samples A4226 and A4234 it was possible to access the Stark regime by cooling the gain sample to -40 °C, thus shifting the peak gain wavelength to a suitable value. Figure 4.12 shows the autocorrelation and spectrum of the laser. The pulses are fit by a 298 fs duration sech-squared pulse and the spectrum has a bandwidth of 4.41 nm, giving pulses that are 1.2 times transform limited. The sech-squared pulse profile is consistent with fast saturable absorber modelocking, as described in section 3.2.1.

We can investigate the effect of changing the detuning by cooling the SESAM. This shifts the absorbing resonance towards shorter wavelengths at a rate of 0.3 nm/K. Figure 4.13 shows the effect on the pulse duration, bandwidth and time bandwidth product of the pulses. The time bandwidth product is expressed as 'times transform limited', that is, the time bandwidth product of the pulse divided by the time bandwidth product of an unchirped pulse. The laser was not entirely stable during the course of the measurement. In particular, the spectrum recorded for the -10 °C data point has a significantly different shape from the other four spectra, resulting in the large val-

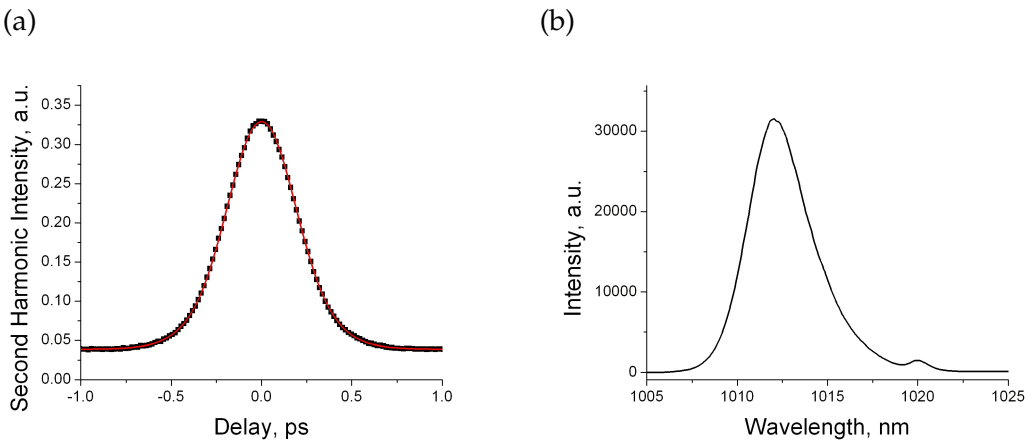

Figure 4.12: Autocorrelation (a) and optical spectrum (b) of pulses from a laser built using samples A4226 and A4234 operating in the Stark mode-locked regime. Pulse duration was 298 fs assuming a sech squared fit and bandwidth was 4.41 nm.

ues of both the bandwidth and the time-bandwidth product for this data point. If we ignore the -10 °C data point, the data shows both pulse duration and bandwidth reducing approximately linearly as the SESAM is cooled. The time bandwidth product also reduces approximately linearly towards the transform limit. Using linear fits to these graphs we can estimate that the temperature at which the transform limit will be reached is -26 °C and that the pulse duration at this temperature will be 284 fs. The obvious conclusion that can be drawn from the shortening of the pulses is that as the SESAM resonance is tuned the modulation depth of the SESAM is increased, increasing the pulse shortening per round trip.

The change in the time bandwidth product can be explained by the influence of increasing SPM as the pulses become shorter. It is possible to estimate the dispersion using a similar analysis to that in section 4.2.3. Modelocking onset measurements have not been performed for this laser but, using the fact that the modulation depth of this SESAM is double that of the SESAM used for the 500 fs laser, we can estimate the shortening per round trip based on the previous measurements. The gain dispersion is a function of pulse duration and can be calculated for each of the five SESAM temperatures.

If we attribute any excess broadening to dispersion we can calculate the magnitude of the total dispersion at each temperature. Figure 4.14 shows the magnitude of the

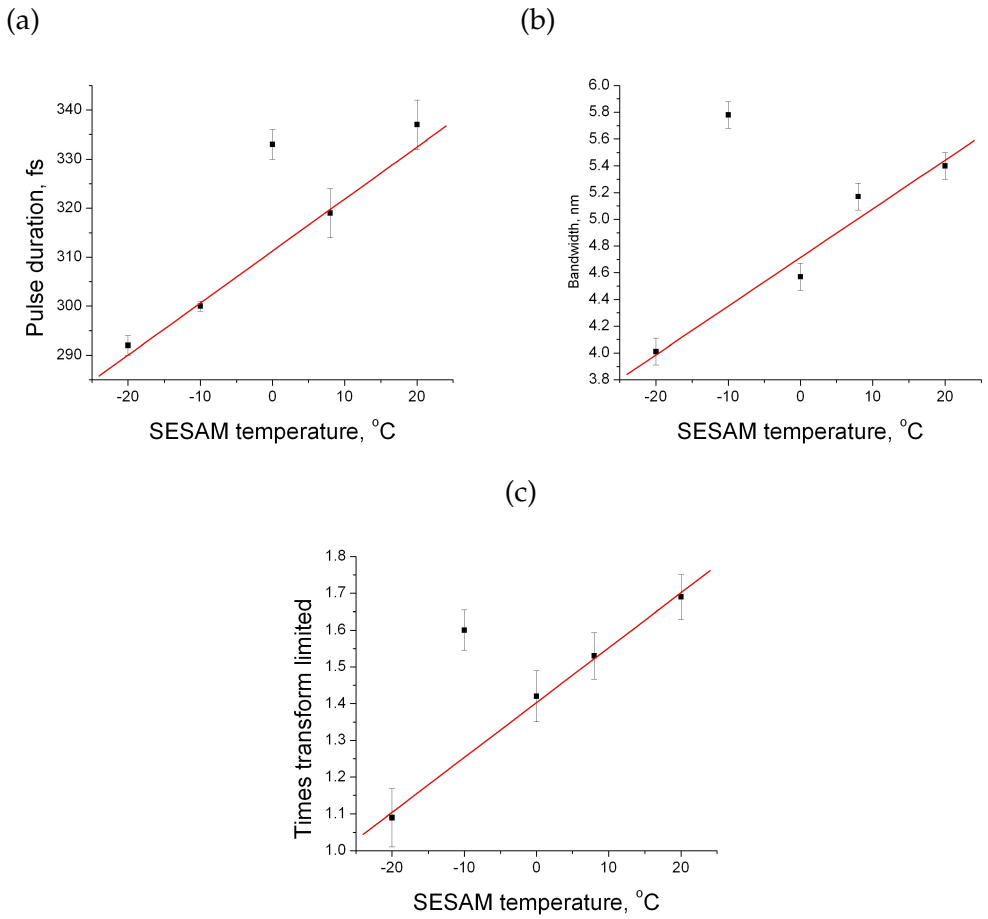

Figure 4.13: Pulse duration (a), bandwidth (b), and time-bandwidth product (c) as a function of SESAM temperature for the Stark mode-locked regime.

dispersion for the different SESAM temperatures. It is impossible to find the sign of the dispersion using this method but we expect the dispersion to become more negative towards higher pulse powers due to self phase modulation. This would mean that the overall dispersion here is positive. Figure 4.14 also shows the time bandwidth product at the five different SESAM temperatures. The larger dispersion of the longer pulses can be seen to cause increased chirp and thus a greater TBP.

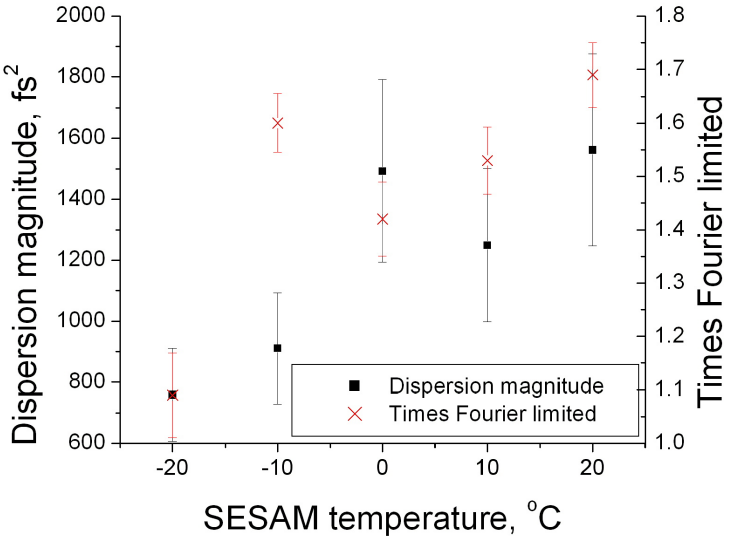

Figure 4.14: Calculated round-trip dispersion (squares) and time bandwidth product (crosses) as a function of SESAM temperature.

4.3.3 70 fs pulse train regime

In the third mode-locked regime seen with this sample combination the gain sample was held at a temperature close to 0 °C. This moved the peak gain wavelength away from the SESAM absorption resulting in a laser that could operate over a much larger bandwidth. The laser output consisted of groups of up to 70 pulses with durations as low as 70 fs. Figure 4.15 shows the optical spectrum of the laser along with a long-delay autocorrelation showing an entire group of pulses, and a short delay autocorrelation showing individual pulses in detail. Also shown is the RF spectrum of the laser. The clean first harmonic and equal powers in higher harmonics both indicate strong coupling between modes.

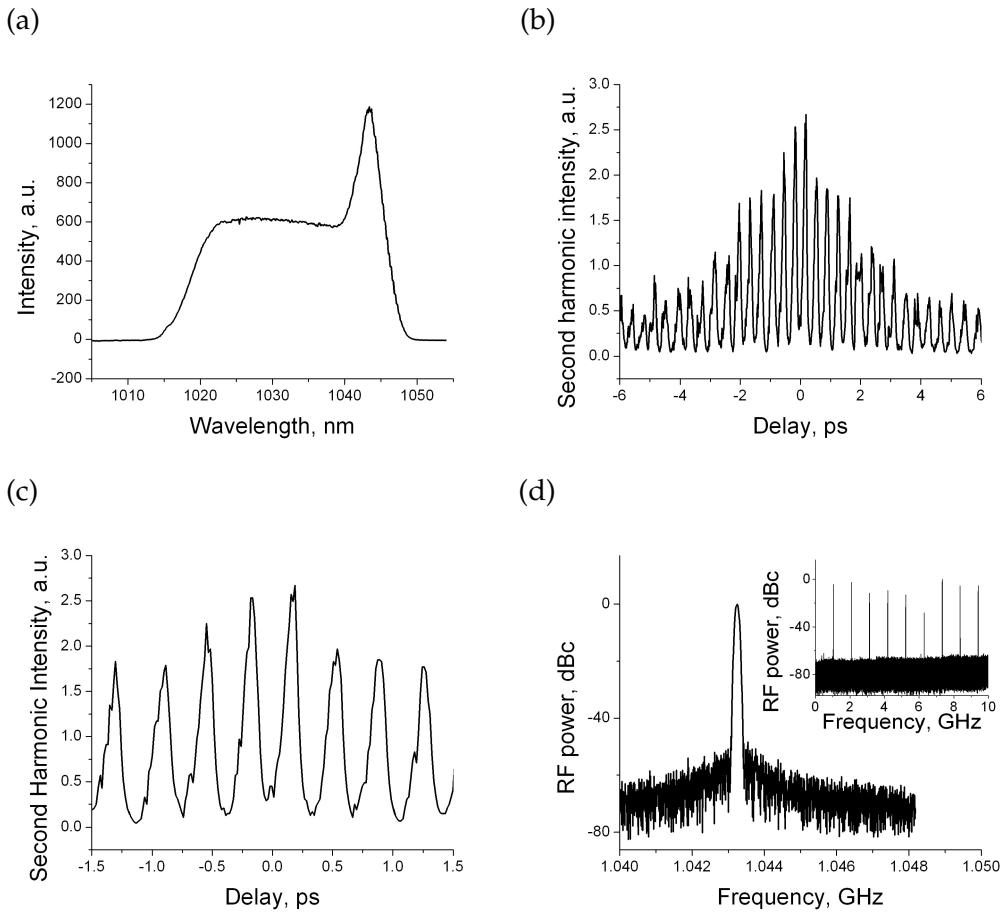

Figure 4.15: Optical spectrum (a) and long delay (b) and short delay (c) autocorrelations of a 70 fs pulse train. (d) shows the RF spectrum of the first harmonic and (inset) the first ten harmonics of the laser repetition rate.

This modelocking regime was highly unstable. Over a timescale of 30 s - 60 s the optical spectrum would collapse towards the sharp peak at the long wavelength end of the spectrum. The pulses in the autocorrelation would broaden and become less distinct until, once the spectrum had fully collapsed, pulses were no longer visible. Mode-locked operation could be restarted by moving to a different spot on the SESAM. However, if the SESAM was moved away and then moved back to the original position lasing continued but modelocking did not restart, indicating that the SESAM was suffering permanent damage, but that the damage did not extend to the DBR as this would have prevented lasing at all.

4.3.3.1 Avoiding SESAM damage

The peak powers on the sample are similar for both the single 300 fs pulses and the 70 fs pulses as, while the 70 fs pulses are significantly shorter, they also have lower energies as there are several pulses per round trip. The energy absorbed by the SESAM per round trip is higher for the 70 fs pulses as in this case the SESAM is bleached many times over per round trip instead of just once. It therefore seemed likely that the cause of the damage was heating of the SESAM. Whether the damage caused by the heat was structural or chemical in nature was unknown. However, it was clear that the damage was restricted to the SESAM surface as any damage deeper in the sample would have affected the DBR and prevented the laser from operating at all. Both a used and a brand new piece of SESAM A4234 were compared using a scanning electron microscope but no additional damage to the surface was visible.

The damage problem was addressed by applying thin layers of alumina to the surface of the SESAM by sputter coating. The coating was designed both to act as a heat spreader, allowing heat to be removed from the surface in two directions rather than just one, and as a coating to prevent water or oxygen from reacting with the surface. Alumina was used as it is transparent at 1 μm and had the highest thermal conductivity of the available sputter coating targets. At 44 $Wm^{-1}K^{-1}$ its thermal conductivity is similar to that of GaAs (45 $Wm^{-1}K^{-1}$) so a large proportion of the heat is still lost through the substrate, but heat is now be removed from the active region in both directions rather than just one.

Using alumina, with a refractive index at 1 μm of 1.58, the ideal thickness for such a coating would have been 162 nm as this would also have acted as an antireflection coating, reducing the Fresnel reflection from the surface of the SESAM and therefore increasing the electric field on the quantum well. It was found, however, that the coatings had to be applied extremely slowly in order for the temperature of the SESAM to stay low enough to not be damaged during the process. This limited the rate of deposition to approximately 4 nm per hour. Applying a 162 nm coating was unfeasible at this deposition rate so eventually films of between 15 nm and 20 nm were applied as these were the thickest films that could be achieved in a reasonable time.

The films were successful in preventing the damage. Broad spectra and short pulses were now observable for several minutes and were much less prone to fluctuations that before. Unfortunately, the coatings also significantly increased the loss of the SESAM resulting in laser thresholds that were approximately 50% higher than with uncoated SESAMs. In a high gain laser this would not have been such a serious issue but in this laser it made it much more difficult to access the short pulse regime. Changes to the sputtering recipe might have improved the optical quality of the coatings thus reducing the losses. In particular, removing any surface oxidation using HCl might have been a more effective way of preparing the SESAM surface than just cleaning the SESAM using acetone and isopropanol.

When the laser is operated with a sample at a temperature below the dew point of air, boil-off from a Dewar of liquid nitrogen is blown across the surface of the sample in order to prevent water condensing onto the sample. It was found that such a flow of nitrogen also largely prevented the damage to the SESAMs. This implies that the damage was due to reactions involving water or oxygen. Any cooling effect of the nitrogen is likely to be minimal as the nitrogen passes through several metres of tubing before reaching the sample and is therefore only marginally cooler than room temperature by the time it reaches the sample. The nitrogen flow was successful in that it prevented the damage but the resulting lasers were not as stable as those using the alumina coated samples. However, the lower loss and reduced complexity of the nitrogen-flow method made it preferable to the alumina coatings. Nitrogen flow was used to prevent SESAM damage in the pulse train laser investigated below.

4.3.3.2 Investigation of the pulse-train regime

The behaviour of the pulse train regime was investigated in the same way as the 300 fs pulse regime, that is, by varying the SESAM temperature. Again, as the SESAM was cooled pulse duration, bandwidth and time-bandwidth product all decreased. Figure 4.16 shows the variation of pulse duration, bandwidth (calculated as twice the variance of the spectrum), and time-bandwidth product with SESAM temperature. Pulse duration was found by taking the average of the durations of 5-7 adjacent pulses. The standard deviations of the durations found this way were typically around 5 fs. It can be seen that the pulse duration decreases with SESAM temperature until it reaches 75 fs where it then stays. It is likely that this limit is the fundamental limit of the modelocking mechanism as the pulse duration approaches the dephasing time as suggested by Daniell et al [54]. The mechanism behind the formation of pulse trains is thought to be dynamic gain saturation, as described in section 4.3.3.3.

It is possible to explain the change in the time bandwidth product using a similar analysis to that used for the 300 fs pulses. The only major change in the analysis is that the gain seen by each pulse is reduced due to the gain saturation effects described below. Figure 4.17 shows the calculated dispersion and the time bandwidth product. In this case, the peak power of the pulses, and therefore the SPM, increases with SESAM temperature. Once again, we cannot know the sign of the dispersion, but the increase in SPM at higher peak powers is expected to make the dispersion more negative, making it likely that the overall dispersion seen here is negative.

4.3.3.3 Dynamic gain saturation

The carrier distribution in a quantum well at thermal equilibrium is given by a Fermi-Dirac distribution whose characteristic temperature matches that of the lattice. Two thermalisation mechanisms are at work in maintaining the stability of such a distribution. Firstly, carrier-carrier scattering ensures that the carrier distribution remains thermal so that it can be described by a Fermi-Dirac distribution, and secondly, carrier-phonon scattering transfers energy between the carriers and the lattice, thus forcing the temperature of the carrier distribution to match that of the lattice.

These two processes occur over different timescales. These timescales have not

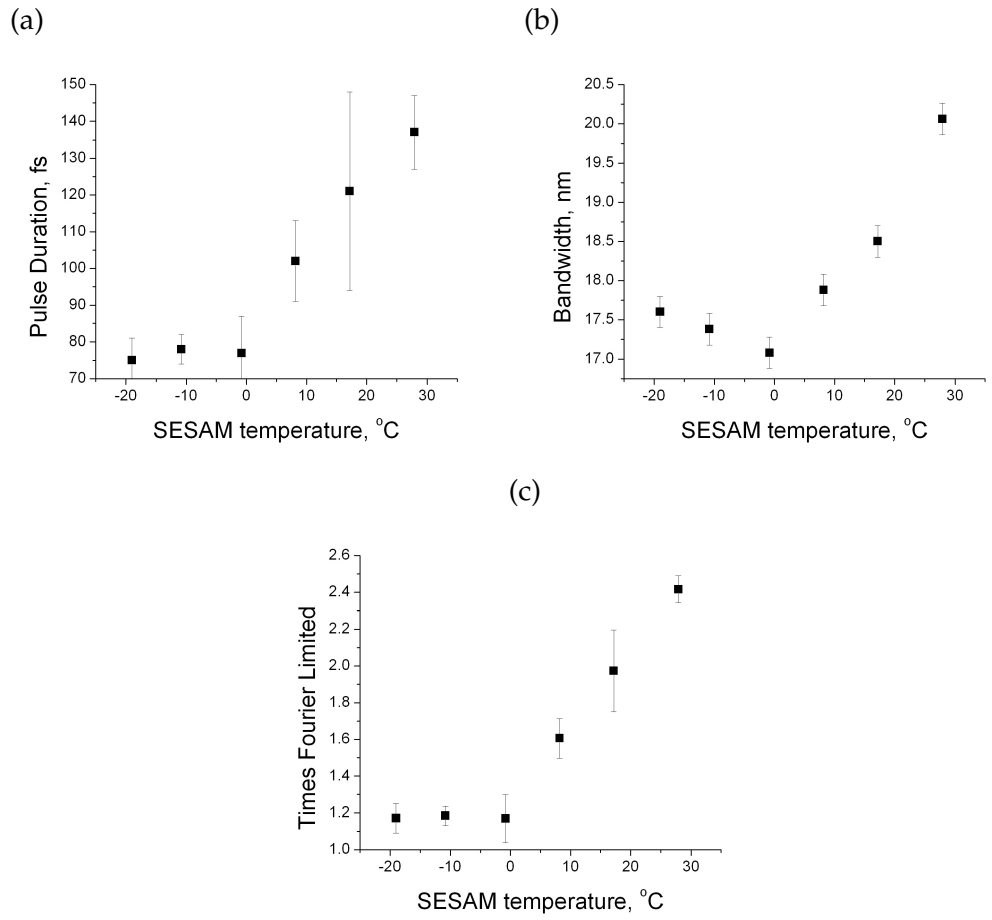

Figure 4.16: Pulse duration (a), bandwidth (b), and time-bandwidth product (c) as a function of SESAM temperature for the pulse train regime. Pulse duration decreases with temperature until a limit is reached at approximately twice the carrier-carrier scattering time.

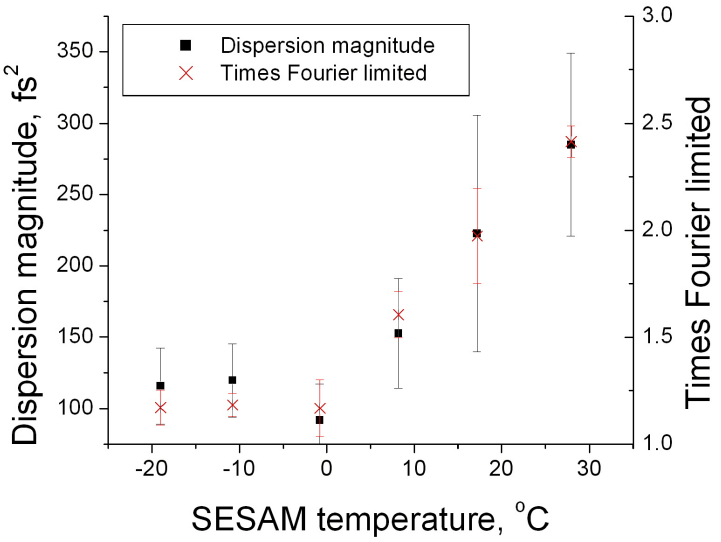

Figure 4.17: Calculated dispersion magnitude and time-bandwidth product as a function of SESAM temperature.

been measured for the quantum wells used in sample A4226, but literature values for similar quantum wells suggest that the carrier-carrier scattering time will be below 100fs [63] and the carrier-phonon scattering time will be of the order of a few hundred femtoseconds [64]. Sample A4234 contains a similar quantum well to those in sample A4226, and we can estimate the carrier-carrier scattering time of this quantum well by measuring the width of the absorbing resonance, though the carrier-carrier scattering time in the gain sample is expected to be lower under operating conditions as it reduces with both temperature and carrier density. For a homogeneously broadened quantum well whose recovery time is much longer than the carrier-carrier scattering time, we expect the width of the absorbing resonance to be set by the carrier-carrier scattering time. As described in figure 2.16, the width of the quantum well resonance of the SESAM can be found by taking reflectivity measurements of the SESAM. The absorption of the quantum well will produce a dip in the DBR stop-band. For SESAM A4234, a Lorentzian fit to this absorption dip gives a resonance width of 32 nm corresponding to a dephasing time of 35 fs, which is consistent with values from the literature. It is impossible to perform a similar measurement for A4226 as its absorption spectrum is complicated by the presence of the longitudinal enhancement factor.

If an ultrashort pulse with a bandwidth narrower that the gain bandwidth and a duration shorter than the carrier-carrier scattering time passes through the gain medium then spectral hole burning can occur. This is when the laser pulse only extracts carriers from the part of the carrier distribution whose transition energies match the wavelengths present in the pulse. This causes the carrier distribution to be depleted at certain energies, distorting it away from a Fermi-Dirac distribution. The carrier distribution will recover to a Fermi-Dirac distribution on the carrier-carrier scattering time as energy is transferred between the carriers, but the characteristic temperature of this distribution will be warmer than that of the original carrier distribution. The carrier distribution will exchange energy with the lattice over timescales similar to the carrier-phonon scattering time, cooling the temperature of the carrier distribution to that of the lattice.

Three possible regimes of laser behaviour exist then, depending on the pulse duration. If the pulse duration is long compared to the carrier-phonon scattering time then the pulse will experience homogeneous gain, with no pulse-duration-dependant gain saturation effects. If the pulse duration is less than the carrier-carrier scattering time then spectral hole burning may occur. A laser operating in this regime will have modelocking dynamics governed by coherent effects, requiring significant modification to the rate equation based modelocking models described in chapter 3, and possibly leading to phenomena like Rabi flopping of the induced polarisation [65], or self induced transparency [66].

The third possibility is if the pulse duration is shorter than the carrier-phonon scattering time but longer than the carrier-carrier scattering time. In this case spectral hole burning will not occur as the carrier-carrier scattering will ensure that a Fermi-Dirac distribution is maintained, but the temperature of this distribution will increase as the pulse removes the lower temperature carriers from the distribution. During the passage of the pulse the gain seen by the pulse will therefore be reduced as the temperature increases, until it is too small to overcome the cavity loss. At this point the window of net gain will close, localising the pulse and preventing it from extracting further energy from the gain.

The pulse will not have extracted all of the energy stored in the gain medium. Af-

ter the pulse has passed the carrier distribution will return to the lattice temperature over a timescale determined by the carrier-phonon scattering time. A second pulse can therefore form after the first to take advantage of the energy not extraced by the first pulse. This pulse will again heat the carrier distribution on passage through the gain meduim, closing the window of net gain. If there is still energy remaining in the gain medium then, once the carrier distribution has cooled, a third pulse can form and so on until all the energy has been extracted from the gain medium.

If the pulse duration is much less than the carrier-phonon scattering time then no cooling of the carrier distribution will occur during the pulse's passage. For longer pulses some energy will be transferred to the lattice during the pulses passage. This reduces the rate at which the pulse heats the carrier distribution meaning that more gain is available to the pulse. The gain seen by the pulse is therefore a function of the pulse duration. Figure 4.18 shows pulse duration and pulse energy as a function of SESAM temperature for the laser described above and clearly shows the pulse energy reducing as the pulse duration decreases.

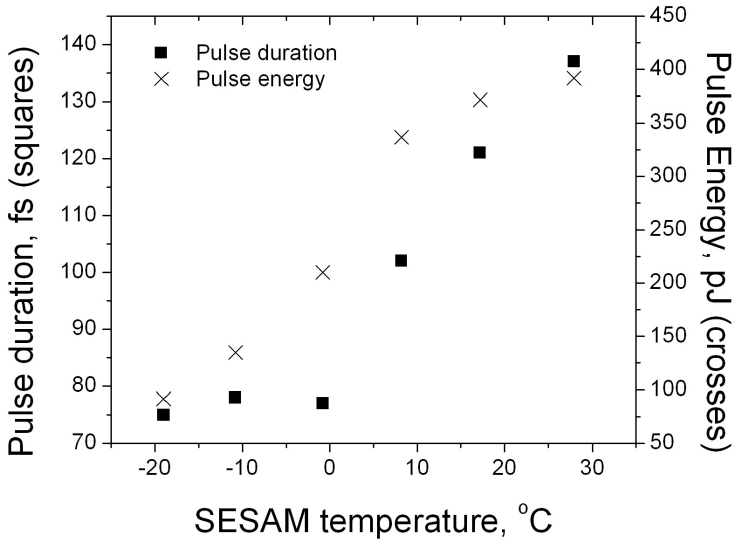

Figure 4.18: Pulse duration(squares) and intracavity pulse energy(crosses) as a function of SESAM temperature.

The separation between the pulses will depend on how quickly the gain recovers which, in turn, depends on the temperature that the carrier distribution has reached as

the laser passes through. This is a function of the pulse energy as more energetic pulses will cause greater heating. Figure 4.19 shows the separation between pulses and pulse energy as a function of SESAM temperature. It is obvious that the separation follows the pulse energy closely.

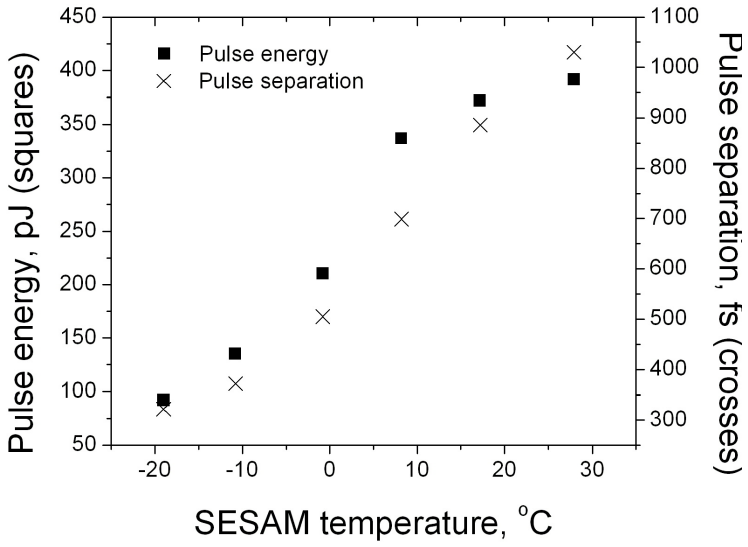

Figure 4.19: Comparing pulse separation to intracavity pulse energy in the pulse train regime. More energetic pulses result in stronger gain saturation and therefore a greater separation between pulses.

A dynamic gain saturation model can explain several of the features of the pulse-train laser output, assuming that the observed pulse durations lie between the carrier-carrier scattering time and the carrier-phonon scattering time. In particular it explains the formation of trains of pulses and the varying separation between the pulses, as well as making approximate predictions of the carrier-carrier scattering time and the carrier-phonon scattering time that are consistent with literature values. Further investigations are needed to fully understand this phenomenon. Measurements of the gain as a function of pulse duration, as well as pump-probe experiments of pumped gain samples would lead to a much clearer understanding of the dynamics of the gain saturation.

4.4 Future work

Further changes to the sample designs are necessary if still shorter pulses are to be produced. Increased gain, reduced gain filtering, and improved dispersive characteristics would all be desirable for improved VECSEL performance.

The lasing bandwidth of the laser in the pulse train regime ($\sim$20 nm) approaches the gain bandwidth ($\sim$30 nm). Gain sample design must therefore focus on increasing the gain bandwidth of the samples and, if necessary, also increasing the gain in order to accommodate the potentially higher losses of the next generation of SESAMs. The two factors limiting the gain bandwidth are the quantum well emission bandwidth and the longitudinal confinement factor. The emission bandwidth is difficult to modify without resorting to radical measures (for example, the use of a quantum dot gain medium). Thankfully, this is not necessary as a broader overall gain bandwidth can be achieved by changing the indium concentration of the different quantum wells in the sample. This will not increase the emission bandwidth of the individual quantum wells but it will increase the emission bandwidth of the gain sample as a whole. The additional inhomogeneity caused by having several different quantum wells may make the laser more susceptible to spectral hole burning.

The filtering of the longitudinal confinement factor can be reduced in two ways. Antireflection coatings could be applied to the sample post growth. This would eliminate the reflection at the sample surface therefore eliminating the microcavity altogether. This would also protect the surface from damage, and the alumina coating of the SESAMs also implies that this may also improve the stability of the lasers. The disadvantages of this method lie in its high cost and in the potential for damage to the sample during coating.

The second way of reducing the effect of the LCF would be to grow a gain sample with a thinner microcavity. This would require a thinner active region which has consequences for the efficiency of the laser as a thinner active region means less pump absorption in the active region and more pump absorption in the DBR. To compensate for this, a DBR that reflects the pump light back through the active region could be used, effectively doubling the length for absorption. This makes for a more complex DBR which may introduce more dispersion.

The most obvious way to increase the gain of the sample is to increase the number of quantum wells and to use a corresponding increase in pump power. In terms of design this can be relatively easily achieved, however, more gain means a steeper gain spectrum which would lead to stronger gain filtering. If more quantum wells were used it would almost certainly become necessary to offset the design wavelengths of the quantum wells in order to compensate for this effect.

Any further samples, either gain sample or SESAM, must be carefully designed in order to keep the total dispersion as close to zero as possible. It is difficult both to calculate accurate values of the theoretical dispersion from different sources and to accurately measure the phase structure of the output pulses. The phase structure of the output pulses can be measured using frequency resolved optical gating, but currently laser stability prevents this. Dispersion from samples could be accurately measured using a white light interferometer. Calculating theoretical values of the SPM generated is more difficult. In these lasers SPM is primarily generated by carrier density fluctuations in the gain sample, and without a clearer understanding of the carrier dynamics crude estimates such as that in section 4.3.3.2 must suffice.

4.5 Conclusions

Improved gain samples with reduced gain filtering, and high modulation depth optical Stark effect SESAMs have been shown to reduce the pulse durations from mode-locked VECSELs, enabling pulses with durations of less than the carrier-phonon scattering time to be produced for the first time in a semiconductor laser. Modelling of optical Stark effect modelocking [54] implies that the shortest pulses that can be generated by this mechanism have a duration of twice the carrier-carrier scattering time. The best estimate of the carrier-carrier scattering time in these quantum wells is 35 fs based on measurements of the quantum well absorption bandwidth, leading to a theoretical minimum pulse duration of 70 fs. This is consistent with the apparent limit of 75 fs seen in the SESAM temperature tuning experiments in section 4.3.3.2.

Once this threshold has been crossed the laser enters a radically different modelocking regime where the dynamics of the laser are dominated by dynamic gain saturation in the gain medium. In this regime the energy extracted from the gain becomes

a function of the pulse duration, reducing the gain seen by shorter pulses. Leftover energy after the passage of the pulse allows trains of pulses to form. Further investigation is needed, both experimental and theoretical, in order to fully understand the laser dynamics when pulse durations are comparable to carrier scattering timescales. In particular, pump probe measurements of an inverted gain sample would allow the gain to be measured as a function of pulse duration.

Chapter 5

Active stabilisation and timing jitter characterisation

5.1 Introduction

The pulses in the output of a mode-locked laser are not perfect replicas of each other. Properties such as the pulse amplitude, shape, and arrival time change from pulse to pulse due to a variety of noise sources. Jitter refers to the variations in these properties and is divided into different components depending on which property is being examined.

Different jitter categories attract different amounts of attention depending of their importance for a given application. Variations of the pulse shape, for example, have a limited effect on most measurements. Jitter of the optical phase only has a significant effect in lasers producing few-cycle pulses. Amplitude jitter is important for experiments where the laser is required to deliver precise amounts of energy, for example pump-probe measurements.

Timing jitter is important for a great many of the applications of mode-locked lasers. Communications and optical sampling both require very accurate pulse arrival times and the resolution of pump-probe and other time domain measurements often depends on the timing jitter. VECSELs have much to recommend them as pulse sources for these types of experiments due to their flexibility, low jitter and high repetition rates.

Many of these applications are improved by a high repetition rate pulse train, as

this increases sampling rates for measurements and transmission speeds in communications systems. Several types of pulse source are capable of reaching these repetition rates. Hybrid modelocking of diode lasers can easily reach these high repetition rates using fundamental or harmonic modelocking but struggles to produce pulse durations shorter than a few picoseconds [67]. Solid state lasers, for example Ti:sapphire [68] and Er:glass [69] systems can reach GHz repetition rates with short pulses, but have less potential for reaching the multi-GHz repetition rates demonstrated by VECSELs.

Longer cavities can be advantageous in terms of reaching low jitter values as a longer cavity means that noise sources act upon a pulse fewer times per second. Harmonic modelocking can allow lasers with long cavities to reach GHz repetition rates but this can leads to a large increase in the timing jitter due to supermode noise, where noise is coupled into harmonics of the repetition rate. Supermode supression is possible but requires very complex set ups [70]. There is therefore a trade-off between the noise related to cavity length and the supermode noise in harmonic modelocking.

Due to their active-mirror architecture and low gain lifetimes VECSELs are particularly well suited to short cavites, and therefore to fundamental modelocking at high repetition rates. Their theoretical minimum timing jitter is also very low, as discussed in section 5.2. This chapter presents the results of recent work on active stabilisation of VECSELs. Both measurement and stabilisation technques are described, likely sources of noise are identified and future work is proposed.

5.2 Noise sources in mode-locked VECSELs

Jitter in mode-locked lasers arises from many sources, for example mirror vibrations, temperature fluctuations and spontaneous emission noise. We can classify these as either classical or quantum noise sources. Classical noise sources, such as vibrations or temperature fluctuations can, in principle, be completely removed by improved laser design. Quantum noise sources are the fluctuations that are due to the quantum nature of the system. Spontaneous emission adds an inherent randomness that results in fluctuations in both the amplitude of the pulses and their arrival time. These fluctuations cannot be engineered away and therefore allow us to define a minimum limit to the jitter of a mode-locked laser.

5.2.1 Quantum noise sources

The fundamental limit to either the amplitude or the timing jitter of a mode-locked laser is set by shot noise. Single-photon fluctuations in a pulse will clearly affect the amplitude of the pulse but will also result in shifts of the pulses 'centre of mass', which is equivalent to timing jitter. Shot noise results in a two-sided spectral power density [71]

$$S_{\delta P}(f) = P_{av} h\nu, \tag{5.1}$$

where P_{av} is the average output power of the pulse train and ν is the optical frequency. Note that this spectral power density is independent of frequency and therefore corresponds to noise with a constant level at all frequencies. The timing jitter can be found by taking the variance of this spectrum and integrating over a measurement bandwidth, B, to give

$$\sigma_T^2 = 0.2647 \times 2B \frac{h\nu}{P_{av}} \tau_p^2, \tag{5.2}$$

where τ_p is the pulse duration and the numerical factor 0.2647 arises from the sech^2 pulse shape. For the laser used in section 5.6 the fundamental limit is 1 as in the bandwidth 300 Hz to 1.5 MHz.

This fundamental limit does not completely describe the effects of quantum behaviour on the timing jitter as it deals only with the discrete nature of the laser field itself and not with the interactions within the laser. The discrete nature of both spontaneous emission and loss results in additional contributions to the noise. For a laser with intensity gain g per round trip the spectral power density is

$$S_{\delta T}(f) = 0.5294 \frac{1}{(2\pi f)^2} \frac{h\nu}{E_p} \frac{g}{T_{rt}} \tau_p^2, \tag{5.3}$$

where E_p is the pulse energy, T_{rt} is the round trip time and f is the offset frequency. Quantum fluctuations also occur due to loss, and in the steady state loss equals gain so the loss will make an identical contribution to the noise, effectively doubling it. From the spectral power density we can calculate the timing jitter to be 30 fs for the same laser and measurement bandwidth as above. This is comparable to the quantum limit of the miniature Er:Yb:glass laser described in [69] and significantly lower than that of the Ti:sapphire in [68].

Shot noise presents a fundamental limit to the jitter of a laser but the limit set by quantum effects on gain and loss is not fundamental and can be compensated for by active stabilisation. Nor is this noise contribution frequency independent. It now scales with f^{-2}, meaning that at small offset frequencies this noise source will dominate, but at high frequencies the laser will reach the noise floor set by the fundamental quantum limit.

Jitter due to the quantum nature of the loss and gain also depends on the round trip time. Lasers with lower repetition rates will experience less jitter from this source. This is a common feature of many noise sources and results from the frequency with which the noise source acts on the laser. If a noise source adds a given amount of jitter per round trip then a laser with more round trips per second will suffer more jitter than a lower repetition rate laser. However, it is much more difficult to stabilise larger cavities against noise, particularly changes in cavity length, so in many cases high repetition rate lasers can have lower jitter.

5.2.2 Classical noise sources

Various different classical noise sources will also contribute to the total jitter of the laser. It is useful to have some idea of the magnitudes of some of these effects. Detailed calculations or experiments to find the noise spectra of different sources are possible but approximate calculations can suffice to give order of magnitude estimates of the contributions towards the total noise. There follow brief calculations to estimate the contributions from mirror vibrations and fluctuations in the temperature, the pump power and the gain and loss.

For a change in cavity length Δl the change in the arrival time of a pulse is $\Delta t = 2\Delta l/c$ where c is the speed of light. The timing jitter contribution due to cavity length fluctuations is simply the RMS of the pulse arrival time, therefore

$$\sigma_T = \frac{2}{c} \langle \Delta l \rangle \,, \tag{5.4}$$

where $\langle \Delta l \rangle$ is the RMS of the cavity length fluctuations.

In order to minimise the length fluctuations all cavity mirrors in this work were mounted on 5 cm diameter aluminium posts rather than the usual 12.5 mm diameter optical posts. Estimating a value of $\langle \Delta l \rangle$ =10 μ m due to mirror vibrations gives

σ_T =70 fs. This assumes that the vibrations are at frequencies within the measurement bandwidth of the experiment. It is likely that noise from the mirror vibrations will appear as spikes in the jitter spectrum rather than as white noise as the mechanical resonances of the components will appear over narrow ranges of frequencies.

Changes in the temperature will cause changes in the cavity length due to thermal expansion of the components. If a component has a thermal expansion coefficcient dx/dT, then the timing jitter due to temperature change ΔT will be

$$\sigma_T = \frac{2}{c}\frac{dx}{dT}\Delta T. \tag{5.5}$$

The thermal expansion coefficient of GaAs is 5.7×10^{-6} K^{-1}. The total thickness of GaAs in both the gain sample and SESAM is approximately 10 μm giving us a total jitter of 4×10^{-19} s for temperature fluctuations of one Kelvin. This is well below the quantum limit for the jitter of the VECSEL used and therefore is not significant.

A more significant source of cavity length change is thermal expansion of the steel breadboard. With a thermal expansion coefficient of 17×10^{-6} K^{-1} and a cavity length of 30 cm jitter of the order of 40 fs is expected. This is unlikely to have any effect on the noise data presented below, however, as due to the large thermal inertia of the breadboard, the timescales over which such shifts will occur are likely to be of the order of minutes and therefore will be outside the jitter measurement bandwidth. In an unstabilised, passively mode-locked laser this kind of cavity length drift would change the repetition rate significantly, but for an actively stabilised laser these low frequency drifts will be completely eliminated, as long as the required cavity length correction signal stays within the bandwidth of the phase-locked loop.

Changing temperature will also cause changes in the refractive index of the gain sample and the SESAM. This can be described in the same way as cavity length changes. GaAs has a refractive index change of $dn/dT = 2 \times 10^{-5}$ K^{-1} with temperature corresponding to a jitter of

$$\sigma_T = \frac{2}{c}\frac{dn}{dT}x\Delta T \tag{5.6}$$

for a thickness x of GaAs. For the values shown this calculation gives $\sigma_T = 1$ as which is similar to the quantum limit.

We saw above that fluctuations in the gain due to quantum effects add timing jitter but gain fluctuations also occur due to changes in the pump power. According to Haus

and Mecozzi [72], the timing jitter spectral density due to gain fluctuations is given by

$$S_T(f) = \frac{\Delta g}{T_{RT}\Omega_g}, \tag{5.7}$$

where Δg is the fluctuation of the round trip incremental gain, T_{RT} is the cavity round trip time and Ω_G is the gain bandwidth. From this one can calculate the timing jitter contribution

$$\sigma_T = \left(\frac{2S_T}{(2\pi f)^2}\right)^{1/2} = \left(\frac{2\Delta g}{(2\pi)^2 f \Omega_g}\right)^{1/2}. \tag{5.8}$$

If I estimate the fluctuations of the gain to be 1% of the gain value this calculation gives a value of $\sigma_T = 45$ fs showing that fluctuations of the gain due to the pump diode are predicted to have an effect of similar magnitude to the quantum gain fluctuations. This effect could potentially be reduced by using a temperature stabilised pump diode and a more stable diode driver to improve the stability of the pump source.

It is worth noting that loss can be treated in a similar manner to gain. This potentially allows one to calculate the jitter caused by changes of cavity alignment due to mirror vibrations. The necessary cavity stability calculations are complex. It is sufficient to note that the variations in loss cannot exceed the value of 1% used for the gain fluctuations above given the amplitude jitter measured in section 5.6.

A more complete treatment of the classical noise sources would follow the same approach as was used for the quantum noise sources, that is, to find the spectral density function of the noise source, and integrate this over the measurement bandwidth. While simple in principle this method would require experimental characterisation of the spectral density functions of the noise sources, which would be complex and time consuming.

5.3 Theory of power spectrum measurements

Time domain measurements of the jitter of VECSELs cannot be performed directly as the pulse-to-pulse jitter is too low to be measured. Several method exist for measuring the jitter of such a laser, mostly relying on frequency domain comparison of the pulse train with a lower noise reference oscillator. One disadvantage of these types of measurement is that the reference oscillator will also contribute some noise to the measured

value. The value of the jitter found by these methods will therefore always be an upper limit to the jitter of the laser. These methods are also better suited to actively mode-locked or actively stabilised lasers as they treat the jitter as a small deviation from a fixed round trip time. In an unstabilised passively mode-locked laser there is no restoring force moving the pulse towards this position potentially allowing the pulse to walk away from its expected position.

Self-heterodyne measurements can also be performed. These measurements eliminate the need for a stable reference oscillator by using the laser itself as a reference. The laser is delayed through several kilometers of fibre before being detected in a second photodiode and used as a reference. As long as the delay is long compared to the coherence time of the laser then the jitter in the two signals will be uncorrelated and the actual jitter can be extracted. As the jitter of the reference is identical to the jitter of the laser being measured the absolute jitter of the laser can be calculated as $\sqrt{2}$ of the jitter measured.

A commonly used method is to use the reference oscillator and the signal from a photodiode as inputs to an electronic mixer [73]. If the relative phase difference between the signals is $\pi/2$ then, for small deviations, the output voltage is proportional to the phase difference. This is a simple and convenient method provided the phase difference between the signals remains small so, once again, this method is better suited to actively mode-locked or actively stabilised lasers. A significant disadvantage of this method is that, unless great care is taken in the design of the electronics, amplitude modulation to phase modulation(AM-PM) conversion will occur in the mixer, causing a significant increase in the measured jitter. Again, the jitter measured includes the jitter of the oscillator, so a low noise oscillator is necessary in order for the jitter measured to represent the jitter of the laser.

A more sophisticated method which avoids many of the problems suffered by other methods has been proposed by Paschotta [74]. This method compares two lasers with similar repetition rates to a common reference oscillator using mixers, detects the resulting signals using an oscilloscope, and then subtracts the resulting signals from each other. In this way the noise of the reference oscillator is eliminated as both channels will have identical contributions from the oscillator noise. The remaining signal will reflect

the jitter of one laser relative to the other. If the lasers are identical then the jitter of a single laser is $\sqrt{2}$ of the relative jitter. This method has several advantages. As the noise of the reference oscillator has been subtracted from the final measured value this value will reflect the noise of the lasers only rather that the noise of the laser and the reference. This means that a low noise oscillator is no longer needed. This method is also immune to AM-PM conversion in the mixers as this depends only on the mixer offsets which are also eliminated when the signals are subtracted. The downside of this method is its complexity. Two similar lasers are required as well as a high bandwidth 2-channel digital oscilloscope or two high resolution digital sampling cards.

A commonly used jitter analysis method proposed by Von der Linde [3] relies on the analysis of the power spectrum of the photodiode output. Such a spectrum will consist of peaks at harmonics of the repetition rate of the laser. The sideband spectral density function of the μth peak, including amplitude jitter-timing jitter correlations, is shown to be given by

$$S_\mu(f) = S_A(f) + (2\pi\mu f_0)S_{AT}(f) + (2\pi\mu f_0)^2 S_T(f), \tag{5.9}$$

where $f = \omega_\mu/2\pi$ is the carrier offset frequency and S_A, S_{AT} and S_T are the spectral density functions of the amplitude jitter, the amplitude-to-timing jitter and the timing jitter. Integrating the power spectrum between two offset frequencies f_1 and f_2 then gives us the total noise in the bandwidth $f_2 - f_1$ in terms of contributions from the amplitude jitter σ_A, timing-to-amplitude jitter σ_{AT} and the timing jitter σ_t.

$$\int_{f_1}^{f_2} S_\mu(f)df = \frac{\sigma^2}{2} = \frac{\sigma_A^2}{2} + (2\pi\mu f_0)\frac{\sigma_{AT}^2}{2} + (2\pi\mu f_0)^2\frac{\sigma_T^2}{2}. \tag{5.10}$$

This analysis assumes that the pulse shape remains constant and ignores any jitter of the optical phase as phase information is lost when the laser signal is detected by the photodiode. It is important to notice that the contributions to the total noise from these different sources vary differently with the harmonic number μ. This enables one to separate out the contributions from the different sources of jitter.

Figure 5.1 shows a schematic of an RF power spectrum. Each harmonic consists of a delta function at the centre frequency plus contributions from the amplitude and timing jitter. Amplitude jitter forms a broad pedestal that does not vary with respect to harmonic number. Timing jitter forms a narrower spike whose intensity increases quadrat-

ically with respect to harmonic number. Amplitude-to-timing jitter is not shown in this figure. A quadratic fit to a graph of sideband area vs. harmonic number will allow σ_A, σ_{AT} and σ_T to be determined.

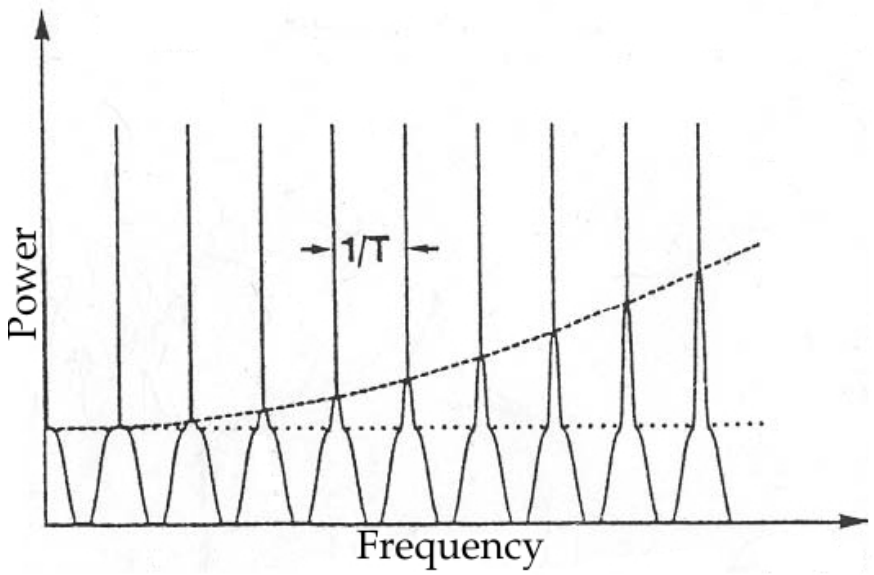

Figure 5.1: A schematic of an RF power spectrum of a mode-locked laser showing contributions to the sideband areas due to amplitude and timing jitter. From [3]

This method provides a fairly complete characterisation of the jitter of a laser, however it has several disadvantages. As discussed above, the jitter measured is the jitter relative to the reference oscillator, in this case the oscillator of the RF spectrum analyser. The jitter measured therefore represents an upper limit to the jitter of the laser, the measured value being a better representation of the absolute value if the jitter of the reference oscillator is significantly less than that of the laser. The second disadvantage comes from the necessity of measuring many harmonics. This makes the measurement very time consuming, requiring stable laser operation for several hours. The measurement is also more difficult for high repetition rate lasers as in order to measure the high harmonics of the spectrum of these lasers the bandwidths of the photodiode and RF spectrum analyser must be very large.

5.4 Previous work on active stabilisation of VECSELs

Active stabilisation works by using a phase-locked loop (PLL) to lock the laser repetition rate to a fixed value. A PLL works by detecting the deviation of the instantaneous repetition rate from a reference frequency and providing a restoring force to return the repetition rate to that frequency. In practice this is done by detecting the laser output using a photodiode, using a mixer to find the phase difference between this signal and a reference, and then using the resulting error signal to control a cavity mirror mounted on a piezoelectric translation stage. This shifts the cavity length so that the repetition rate matches the reference signal. Often proportional-integral-differential(PID) control is used to further improve the stabilisation.

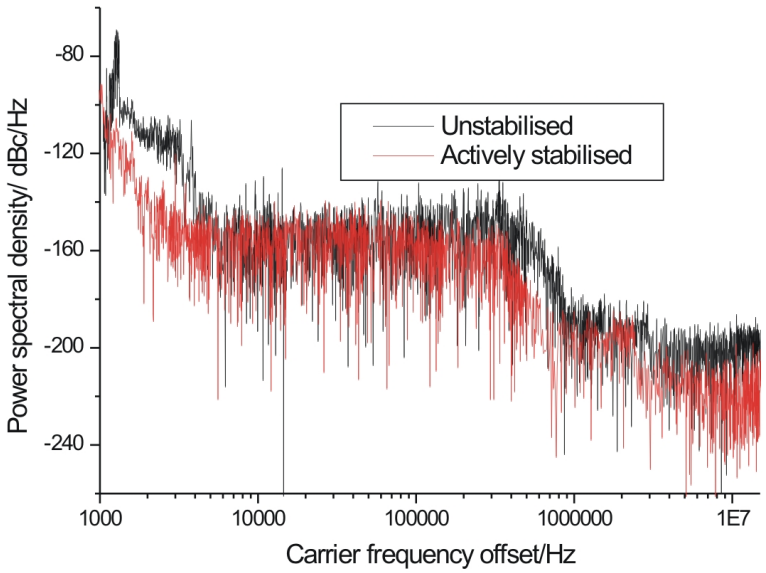

Figure 5.2: Unstabilised and actively stabilised RF power spectra of a 2.3 ps pulse duration VECSEL. Stabilisation has reduced the noise level up to frequencies of 5 kHz. From [4]

Previous work by Wilcox et al. [4] used this method to lock a VECSEL with a repetition rate of 897 MHz to an electrical reference oscillator at the same frequency. The jitter characteristics of the laser were measured with and without active stabilisation using the von der Linde method. Figure 5.2 shows the extracted jitter spectra with and without active stabilisation. Comparing the jitter spectra it is clear that the active sta-

bilisation has reduced the jitter over a bandwidth extending up to 5 kHz. The jitter has not been reduced at higher frequencies as the stabilisation bandwidth is limited by the response time of the piezoelectric stage. Passive stabilisation was also used by mounting the mirrors on stable posts and enclosing the laser in a box to prevent air flow and temperature changes.

The work presented here builds on this work in two ways. Firstly the VECSEL in the previous work was operating in a slow saturable absorber modelocking regime rather than the Stark modelocking regime and was therefore producing 2.3 ps pulses rather than sub-picosecond pulses. The modelocking build-up measurements performed by Keith Wilcox showed that slow saturable absorber modelocking produces a stronger pulse shaping per round trip and so could be expected to be less susceptible to perturbations than Stark modelocking. It was therefore desirable to characterise the noise of a Stark modelocked VECSEL.

Secondly, the VECSEL was locked to a reference oscillator whose frequency was the same as the laser repetition rate, whereas in this work a frequency divider is used to lock the laser to a reference with a much lower frequency. This means that a lower frequency reference oscillator can be used, which is an advantage as lower frequency oscillators are typically cheaper and have better noise characteristics than higher frequency oscillators.

5.5 Frequency-divider based stabilisation scheme

A schematic of the stabilisation electronics used in this later work is shown in figure 5.3. Part of the laser output was detected in a 25 GHz New Focus model 1414 photodiode. The resulting RF signal was amplified in a high bandwidth amplifier and used as the input signal to an Analog Devices model ADF4106 PLL frequency synthesizer chip. The reference signal for the system was a Stanford Research Systems model SC10 10 MHz ovenised oscillator. The PLL frequency synthesizer produces an output signal that is proportional to the phase difference between the two inputs. This signal is filtered above 10 kHz to reject frequencies higher than the bandwidth of the piezoelectric stage and then amplified and used to drive the translation stage.

The PLL frequency sythesizer consists of two major components. The first is an

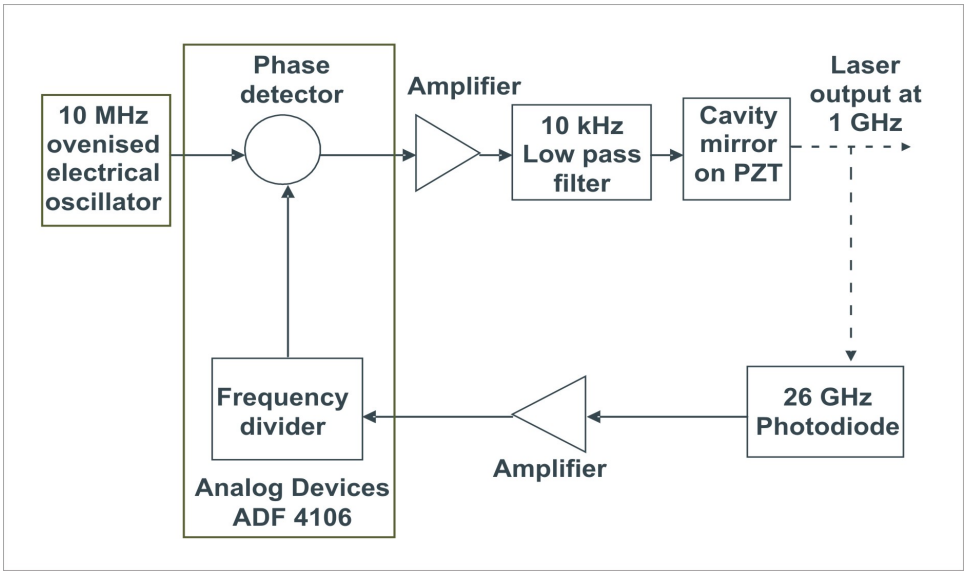

Figure 5.3: Schematic of the stabilisation scheme.

integer-N programmable frequency divider. This reduces the frequency of the input signal by an integer factor N by discarding $N-1$ out of every N pulses but letting the Nth pulse pass. For this work N was set to 100 in order to match the 1 GHz signal from the photodiode output to the 10 MHz reference signal.

The second component is a phase frequency detector (PFD). The PFD operates by emitting pulses of current that are proportional to the delay between the arrival times of the pulses from the reference signal and from the divided input signal. The current pulses are emitted at the frequency of the reference signal and are then integrated by the 10 kHz loop filter, which has the effect of converting the 10 MHz series of pulses to a continuously varying signal in the bandwidth DC to 10 kHz.

The use of a programmable divider makes this a highly versatile method as it allows lasers with a wide range of repetition rates to be stabilised to the same oscillator using the same electronics. It also allows the use of lower frequency reference oscillators which is particularly useful given the high repetition rates of VECSELs. The disadvantage of using a divider is that instead of locking every pulse to the reference only every Nth pulse is stabilised. Mathematically, this is equivalent to locking the laser to a reference oscillator whose phase noise is $20\log_{10}(\mathrm{N})$ larger than that of the actual oscillator used. This is not as severe a disadvantage is it may appear, as the

phase noise characteristics of low frequency oscillators are typically much better that high frequency oscillators.

5.6 Active stabilisation of a Stark mode-locked VECSEL

The laser used in this work was a 1 GHz Z-cavity using samples QT1544 and QT1627. The only significant differences between this laser and the one described in section 4.2.3 were that the output coupler mounted on a piezoelectric translation stage and that the cavity length was adjusted to give a repetition rate of exactly 1.00 GHz, as the repetition rate needs to be an integer multiple of the reference oscillator frequency. Passive stabilisation was also used. All cavity mirrors were mounted on stable 50 mm diameter posts to reduce vibrations and the whole laser was covered by a box made of insulating foam to reduce air currents and temperature fluctuations. The autocorrelation and optical spectrum of the laser are shown in figure 5.4. The output power of the laser was 40 mW.

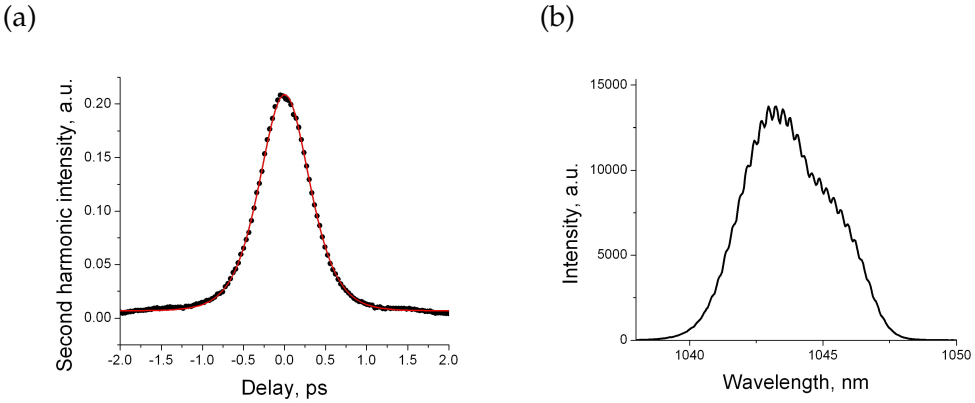

Figure 5.4: Second harmonic autocorrelation and optical spectrum of a laser producing 470 fs pulses. A sech squared fit to the autocorrelation gives a pulse duration of 470 fs and the optical spectrum has a bandwidth of 4.1 nm making the pulse 1.1 times transform limited.

Part of the output from the 25 GHz photodiode was amplified using a low noise broadband amplifier and analysed using an Advantest R3273 RF spectrum analyser. The sidebands of eight of the harmonics of the power spectrum were measured up to an offset frequency of 1.5 MHz. Each sideband measurement consisted of six scans

of the instrument with different frequency spans and resolutions in order to achieve a good data range and resolution within a reasonable acquisition time. Sidebands of the first, fifth and thirteenth harmonics are shown in figure 5.5. Jitter can be seen to be concentrated at offset frequencies below 3 kHz and the noise floor of the RF spectrum analyser was reached at offset frequencies above 1 MHz.

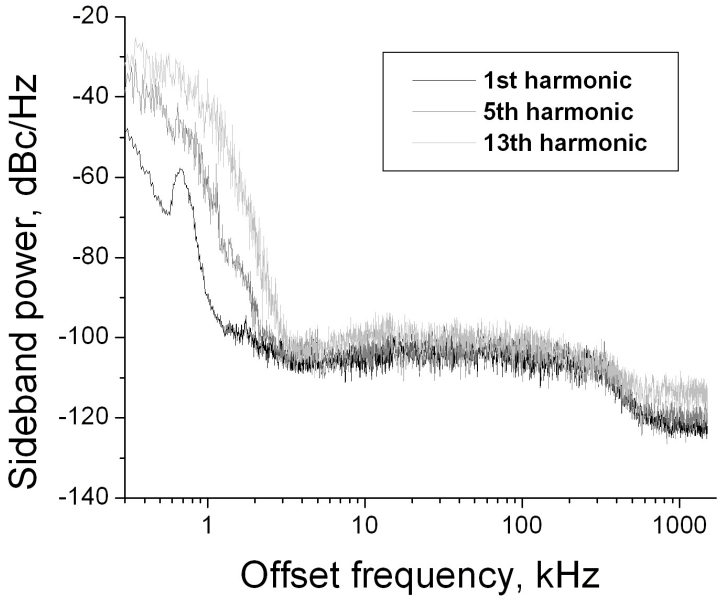

Figure 5.5: Sidebands of the 1st, 5th and 13th harmonics of the power spectrum.

The flat plateau extending up to 500 kHz is a result of the coherence time of the laser. Adjacent pulses in any laser will show a large degree of coherence, therefore the noise of the laser at high offset frequencies is very low. The degree of coherence is reduced towards lower offset frequencies as noise is added to the pulse every round trip. Once the coherence between pulses has reached a minimum level then this increase in the noise spectrum will cease, leading to a plateau. The frequency at which the plateau begins is called the corner frequency, and for a given type of laser it is proportional to the repetition rate, resulting in higher jitter in high repetition rate lasers.

By fitting a quadratic curve to a plot of area under the sideband versus harmonic number, as shown in figure 5.6, we can use the von der Linde method to extract values for the timing jitter and amplitude jitter according to equation 5.10. The rms timing jit-

ter was found to be 190±12 fs over the bandwidth 300 Hz to 1.5 MHz [75]. The rms amplitude jitter in the same bandwidth was 0.17±0.04%. These values represent an upper limit to the jitter of the laser, as the fluctuations measured in the power spectrum sidebands also include those from other noise sources, such as the RF spectrum analyser. As these values are similar to those measured by Wilcox et al. we can conclude that neither of the different modelocking mechanisms investigated has an inherently lower jitter.

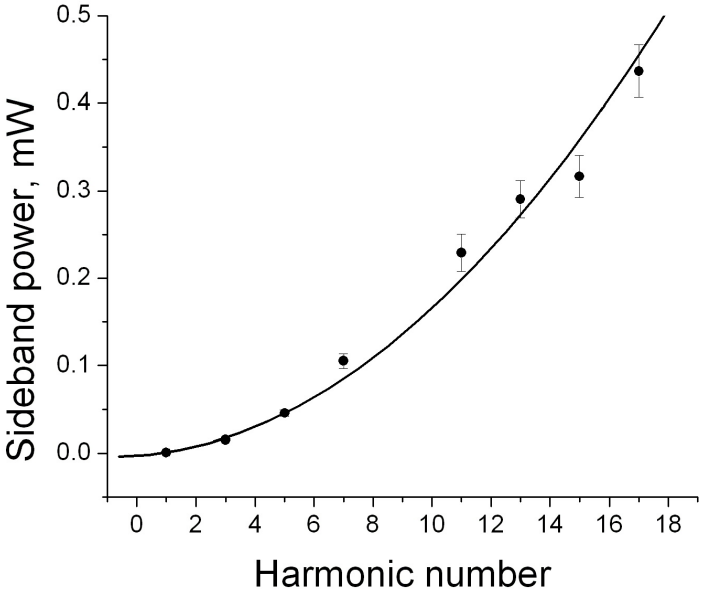

Figure 5.6: Area of the sidebands of the harmonics of the laser power spectrum as a function of harmonic number. From the quadratic fit a value for the timing jitter of 190 fs in the bandwidth 300 Hz to 1.5 MHz can be extracted.

The calculations in section 5.2 are crude but they nonetheless provide us with an insight into the main sources of the jitter seen in the experimental data. The values from the mirror vibrations (70 fs) and the quantum (30 fs) and classical (45 fs) gain and loss fluctuations are of the right magnitude to account for the observed timing jitter.

5.7 Future work

According to the calculations presented above the main sources of noise in mode locked VECSELs are likely to be mirror vibrations and pump fluctuations. Future work must therefore address these problems. The pump source is a 1 W fibre-coupled diode laser. Stabilising the drive current and diode temperature would improve the pump stability, but the largest improvement is likely to come from mounting the diode in such a way that the fibre is unable to move. Likewise, mirror vibration can be significantly reduced by mounting the entire laser on a stable base. Figure 5.7 shows such a stable base upon which two VECSELs can be mounted side by side.

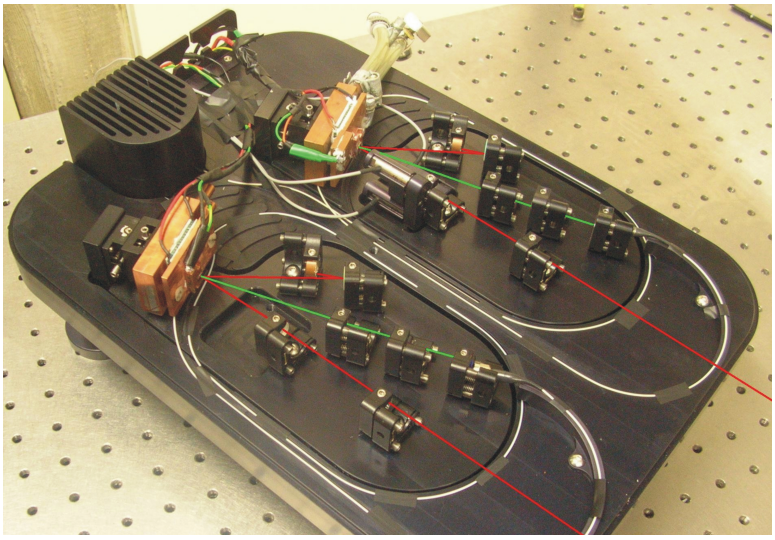

Figure 5.7: Photo of a stabilised base for two VECSELs. Red lines show the laser beam paths, green the pump lasers. Both the mirrors and the pump fibres are securely mounted to prevent vibration.

One of the obvious applications for stabilised VECSELs is in time domain pump-probe measurements such as terahertz time domain spectroscopy (TTDS). A typical TTDS set up is shown in figure 5.8. In this system each pulse in the train from a mode-locked laser is split into two and sent down two different beam paths. One pulse is focussed onto a biased dipole antenna which acts as a terahertz emitter. The resulting terahertz pulse passes through a sample before arriving at an unbiased antenna that acts as a terahertz detector. The other half of the laser pulse passes through a delay line before arriving at the detector antenna where it is used to gate the terahertz detec-

tion. As the delay line is scanned the detector pulse is scanned past the terahertz pulse allowing the temporal profile of the terahertz pulse to be measured. A Fourier transform of this profile decomposes it into its frequency components allowing the terahertz absorption spectrum of the sample to be found.

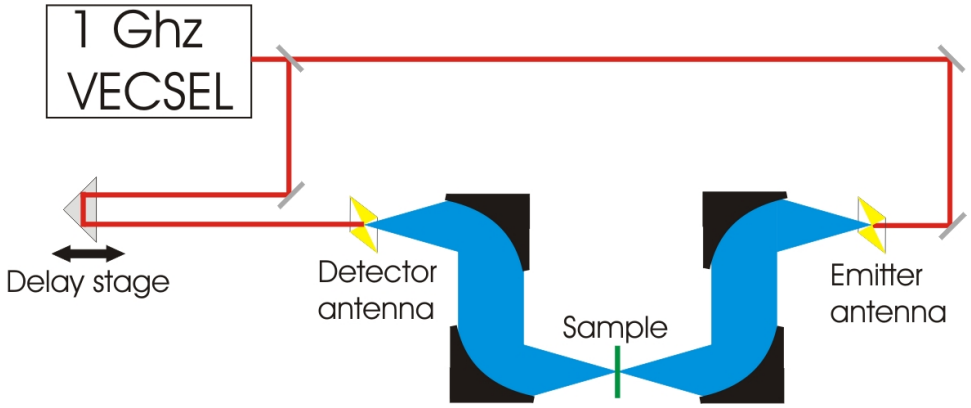

Figure 5.8: Schematic of a typical TTDS set up. Laser beam paths are shown in red, terahertz in blue.

A VECSEL has already been used to drive such a system [76] enabling the first demonstration of an all-semiconductor terahertz time domain spectrometer. The time resolution of such a system is limited by either the pulse duration of the laser or its timing jitter depending on which one is larger. For the system demonstrated the pulse duration was 480 fs. The jitter of this particular laser was not measured but, as it was a similar laser to the free running laser in [4], assuming a value of approximately 350 fs is not unreasonable. It is therefore likely that in this system the pulse duration was the limiting factor rather than the timing jitter. However, as VECSELs with shorter pulse durations become available it is clear that active stabilisation will be necessary if the timing jitter is not to become the limiting factor.

If, instead of a single laser, two lasers with slightly different repetition rates are used, with one driving the emitter and the other driving the detector, then the detector pulse will sweep through the entire delay range without the need for a mechanical delay stage. This technique, known as asynchronous optical sampling (ASOPS) [77], improves on the traditional time domain set-up in several respects. Mechanical delay lines are inconvenient as they can lead to changes in alignment and spot size when long delays are used. They also limit the speed at which the time delay can be scanned,

meaning that TTDS measurements typically take many minutes to complete. If faster scanning is required then a shaker can be used, but the achievable time delay is very small. ASOPS provides a solution to these problems. Changing the delay no longer affects the alignment allowing the entire time window between two successive pulses to be scanned, and the scanning speed is set by the difference between the laser repetition rates and can therefore be much quicker.

An ASOPS system is shown in figure 5.9. This system uses two similar lasers whose repetition rates differ by 10 kHz. One of the lasers is used as a reference oscillator for the other in a master-slave configuration. The repetition rate difference is maintained by shifting the reference signal by 10 kHz before it reaches the mixer. Using a 1 GHz repetition rate gives a total delay range of 1 ns, and a 10 kHz frequency offset will mean that this delay range is swept once every 100 μs. Many sweeps of the delay can be averaged to reduce the noise level. The active stabilisation scheme described in section 5.6 is suitable for application to this type of system as one of the key features of the scheme is that the master and slave oscillators have different frequencies. The frequency-divider based stabilisation scheme is much more appropriate, though some modifications would be necessary in order to reach the repetition-rate to frequency-offset ratios required for this experiment, for example the use of a fractional-N divider rather than an integer-N divider.

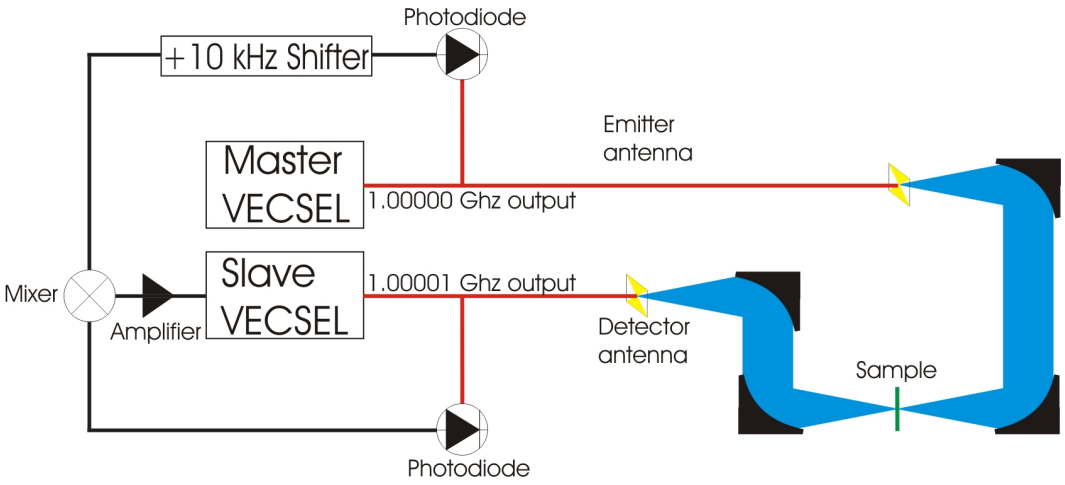

Figure 5.9: Schematic of an ASOPS TTDS set up. Laser beam paths are shown in red, terahertz in blue, electrical signals in black.

ASOPS eliminates the need for a mechanical delay stage, but it does place rather severe requirements on the data acquisition system. As the delay is shifted continuously, the sampling speed of the data acquisition must equal the repetition rate of the probe laser. Data acquisition cards are available at these speeds but they are expensive. Stabilising one laser with respect to another presents another possibility for delay line free pump-probe experiments without this disadvantage.

The ASOPS scheme presented above can be modified by replacing the frequency shifter with a variable phase shifter. In this case the lasers will be locked at the same repetition rate, but the arrival time of the pulses from the slave laser with respect to the pulses from the master can be adjusted electronically by using the phase shifter. The phase shifter then functions exactly as a delay stage would but without the disadvantages of alignment errors and slow scan speeds.

5.8 Conclusions

The work presented in this chapter represents a successful extension to the work previously carried out on the stabilisation of mode-locked VECSELs. The timing jitter of a Stark mode-locked VECSEL has been measured as 190 fs in the bandwidth 300 Hz to 1.5 MHz. As this is a similar value to that measured for a slow saturable absorber mode-locked VECSEL it can be concluded that any inherent difference in the noise characteristics of the two modelocking methods is small compared to other noise sources.

This work also presents a novel active stabilisation scheme which uses a frequency divider, producing a more flexible locking scheme and allowing cheaper and more stable low frequency reference oscillators to be used. The benefits of this will become more apparent if higher repetition rate VECSELs are used. The principal noise sources present in the system have been identified and future work proposed to reduce their impact on the timing jitter.

Chapter 6

Carbon nanotube saturable absorbers

6.1 Introduction

Various materials have been used as saturable absorbers for laser modelocking, as any material with absorption at the right wavelength and a suitable recovery time can, in principle, be used. In recent years SESAMs have become one of the most widely used saturable absorbers due to their flexibility and simplicity of use. However, significant disadvantages of SESAMs include the limited bandwidth of the absorbing resonance and the relatively long recovery times of buried semiconductor quantum wells. As discussed in chapter 3 shorter recovery times are necessary for the generation of sub-picosecond pulses.

Various methods have been used to reduce the recovery times of SESAMs. These all share the same principle; introduce defects close to the quantum well so that carriers can recombine non-radiatively at these defect sites. Commonly used methods are ion implantation, where the sample is bombarded by high energy ions post-growth, and low temperature growth, where the sample is grown at low temperature in order to allow defects to form during the growth. Both of these methods can reduce the recovery times from the order of nanoseconds to less than a picosecond, but this improvement comes at the price of increased insertion loss of the component.

Other methods for speeding up the recovery rely on changing the sample design

in order to place the SESAM close to some structure where rapid recombination is possible. Quantum wells placed very close to the air interface of the sample can have increased recovery rates, as carriers generated in the quantum well can tunnel from the quantum well to the surface, where they can recombine at surface defect sites. This can provide devices with lower loss than ion implanted or low temperature grown material, but these devices require a large electric field at the sample surface, increasing the scattering losses slightly and potentially causing significant GDD in the sample. Buried quantum wells can be surrounded by superlattice layers, which provide a similar recombination route without the need for a large surface E-field but at the cost of more complex sample growth.

A final method for achieving fast recovery in SESAMs is by using the optical Stark effect, as described in section 3.2.3. This can provide a fast response with low losses, and has been used to generate sub-100fs pulses in VECSELs. It is however, a very weak pulse shaping mechanism and requires careful control of the absorption wavelength. There also appears to be a fundamental limit to the duration of pulses shaped by the optical Stark effect. Modelling by Daniell et al. [54] suggests that this mechanism cannot form pulses shorter than twice the inverse resonance width. In this case the limited absorption bandwidth of SESAMs becomes an issue.

In view of the disadvantages of SESAMs it is desirable to investigate saturable absorbers based on other materials. Single-walled carbon nanotubes (SWCNTs) are single crystals of graphite-like carbon, with the form of a single sheet of graphene rolled into a cylinder, as shown in figure 6.1. They have highly promising properties for mode-locking at 1 μm, most notably a resonance width of over 100 nm and recovery times of the order of 700 fs. Carbon nanotube based absorbers have been used to mode-lock various types of laser successfully, including Er [78,79], Yb [80,81], Cr [82] and Nd [83] based solid state lasers, Yb [84,85], Er [86–88] and Tm [89] doped fibre lasers and semiconductor optical amplifiers [90], at wavelengths between 1 μm and 1.9 μm producing pulses as short as 68 fs.

Another advantage of SWCNTs over semiconductor devices is their relative ease of fabrication. Carbon nanotube saturable absorbers are usually made by preparing a solution of SWCNTs and a polymer and allowing this solution to dry on a substrate,

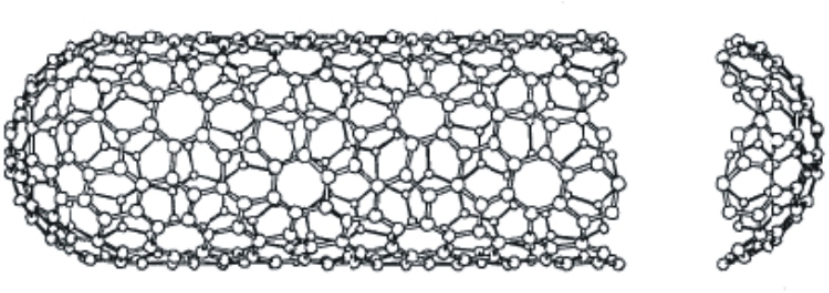

Figure 6.1: A chiral nanotube with a diameter of 1.03 nm. From [5]

leaving a polymer layer with nanotubes embedded in it. This simple solution processing can be done with standard laboratory equipment, in contrast with the highly expensive and specialised MBE and MOCVD reactors required for SESAM growth. This has the potential to make SWCNT saturable absorbers much cheaper, and it also allows absorbers to be made on a wide variety of substrates and over a wide variety of geometries.

This chapter will first describe the optical properties of SWCNTs and an attempt to fabricate a reflection-type SWCNT-based absorber suitable for VECSEL modelocking.

6.2 Optical properties of SWCNTs

SWCNTs can show different electronic behaviour, semiconducting or metallic, depending on the chirality of the nanotube. Figure 6.2 shows a sheet of graphene. Rolling the sheet into a nanotube has the effect of positioning the point given by vector **L** over the origin. Primitive translation vectors **a** and **b** are also shown allowing us to write $\mathbf{L} = n_a\mathbf{a} + n_b\mathbf{b}$. The vector **L** is called the chiral vector and describes both the diameter of the nanotube and the orientation of the hexagons on the tube surface. Only certain values of n_a and n_b are geometrically possible, as described by the equation

$$n_a + n_b = 3N + \nu, \tag{6.1}$$

where N is an integer and $\nu = -1, 0, 1$.

By calculating the band structure using an effective mass approximation [6] it can be shown that SWCNTs with $\nu = 0$ are metallic whereas SWCNTs with $\nu = -1, 1$ are

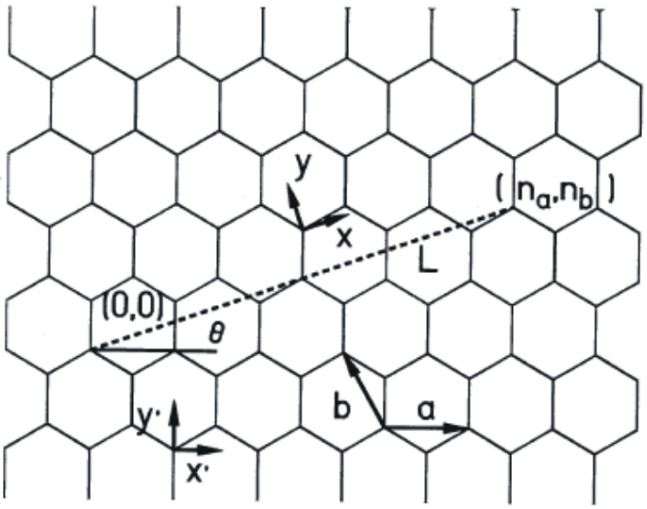

Figure 6.2: Graphene sheet with chiral vector **L** and primitive translation vectors **a** and **b**. A carbon nanotube with chiral vector **L** is represented by wrapping such a sheet into a tube such that the atom at position (n_a, n_b) lies at the origin. From [6]

semiconducting. Figure 6.3 shows the predicted band structure of metallic and semiconducting nanotubes of diameter 0.7 nm. The size of the bandgap for the semiconducting nanotubes is inversely proportional to the diameter of the nanotube according to the equation [6]

$$E_g = \gamma \left| \frac{2\pi}{3L} \right|, \tag{6.2}$$

where $L = |\mathbf{L}|$ and $\gamma = 1.29 \times 10^{-9}$ eVm.

Only semiconducting nanotubes are suitable for use in a saturable absorber. Any metallic nanotubes in the absorber will serve only to increase the non-saturable loss of the absorber. Most methods for producing SWCNTs produce approximately equal numbers of $\nu = -1, 0,$ and 1 nanotubes, therefore giving approximately half as many metallic as semiconducting nanotubes. This is not acceptable in a VECSEL where non-saturable losses must be kept to an absolute minimum. Various methods exist for sorting nanotubes in solution, usually by using their different electronic properties [91] or by allowing them to react with functional groups with different affinities for the different chiralities [92].

Many methods also exist for synthesising carbon nanotubes including arc synthesis [93], laser ablation [94] and catalysed chemical vapour deposition [95, 96]. Most

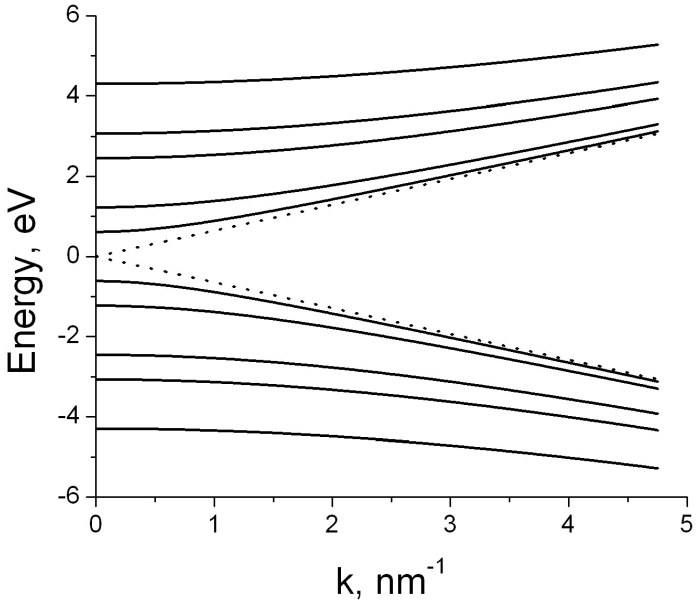

Figure 6.3: Predicted energy levels of a 0.7 nm diameter nanotubes. Solid lines show semiconducting nanotubes, dashed lines show metallic nanotubes.

of these methods produce both metallic and semiconducting nanotubes, but recently improvements in catalytic growth methods have made it possible to selectively grow SWCNTs with a particular chiral vector to a purity of up to 90%. This gives the potential for an acceptable ratio of saturable to non-saturable loss without additional purification. The SWCNTs used in this work were produced in this way by SouthWest NanoTechnologies (SWeNT) and were used without further purification. Just as importantly, the same methods allow the growth of batches of nanotubes with a small range of diameters. As the bandgap of a nanotube depends on its diameter this allows for samples closely tailored to a particular laser wavelength.

Pump probe measurements have been performed on various types of SWCNT absorber, including transmission-type and reflection-type polymer film absorbers and nanotube powder samples [79–81, 97]. These measurements have all found recovery times of the order of 700 fs, significantly faster than the surface quantum wells used in samples QT1627 and A4234. SWCNTs are also expected to show a significant Stark shift. If used for optical Stark modelocking then SWCNTs could potentially produce pulses as short as 20 fs based on the limit set by the resonance width, as discussed in

section 3.2.3.

The saturation fluences of several SWCNT-polymer composites have also been measured, yeilding values of approximately 1-2 μJ cm^{-2} [80,81,86,97]. This is significantly less than the SESAMs used elsewhere in this work whose saturation fluences were of the order of 50-100 μJ cm^{-2}. A VECSEL using a SWCNT saturable absorber would therefore require a much larger spot on the absorber than a VECSEL using a SESAM for stable modelocking. This has implications for the cavity design of a SWCNT modelocked VECSEL as discussed below in section 6.4.

6.3 Methods used to produce SWCNT saturable absorbers

A wide variety of different methods have been used to prepare SWCNT saturable absorbers. This section provides a brief review of these methods.

Most of the SWCNT saturable absorbers used for laser modelocking have been produced by preparing a solution containing both SWCNTs and a polymer and allowing the solvent to evaporate [88,98]. For transmission type absorbers the solution is typically coated onto a substrate and allowed to dry to form a film several microns thick. These films are usually used in fibre lasers as the high gain of these lasers can easily overcome any losses caused by imperfections in the film. In this case the film is removed from the substrate and then sandwiched between two fibre end ferrules as part of a fibre ring cavity.

Reflection type absorbers start from the same types of solution but in this case the solution is coated onto a cavity mirror, usually by spin coating, and then allowed to dry [78]. Films formed this way typically have lower non-saturable loss due to the higher homogeneity of spin coated layers. However, spin coated layers tend to be thinner, limiting the number of nanotubes present and therefore the modulation depth of the absorber. Reflection-type absorbers are therefore generally more suitable for low gain lasers.

Absorbers for fibre lasers have also been produced by embedding tapered fibres in a polymer-nanotube composite [99]. In these absorbers the evanescent field of the light propogating in the fibre interacts with the nanotubes without the pulse itself passing through the absorber. Figure 6.4 shows all three geometries described above.

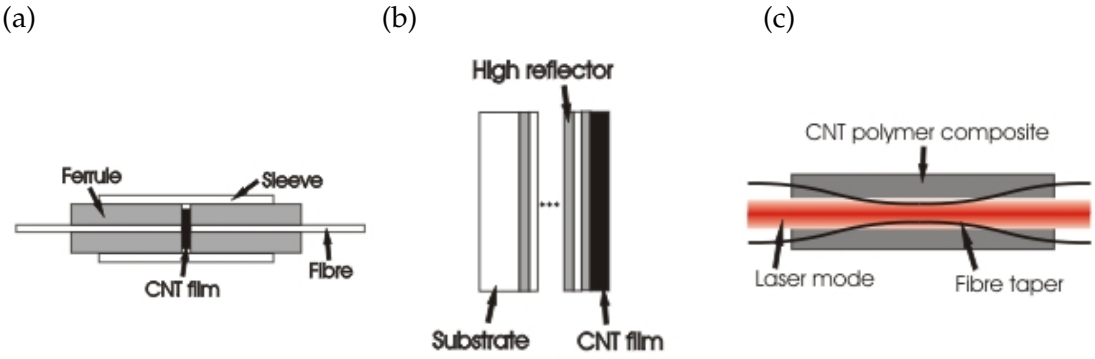

Figure 6.4: Three commonly used SWCNT absorber geometries. (a) A thin CNT/polymer film is sandwiched inside a fibre ferrule. (b) A high reflector is coated with a CNT/polymer film. (c) A tapered fibre is embedded in a CNT/polymer composite.

Methods other than polymer-nanotube solution processing exist for coating substrates. Solutions of nanotubes alone can be sprayed onto a substrate using an airbrush [79]. In this case there is no polymer fixing the nanotubes in place. They are held in place by the strong van der Waals forces resulting from their large surface area. Great care must be taken to avoid inhalation of nanotubes when preparing samples by this method.

Nanotubes have also been precipitated directly from solution onto fibre ends [85]. In this case a fibre end is suspended in a nanotube solution, allowing nanotubes to become attached to the fibre. The process can be accelerated if CW radiation is passed through the fibre. Local heating on the fibre end causes thermophoresis, resulting in nanotubes being attracted to the fibre end and increasing the deposition rate.

All of the methods above start from a nanotube solution. This can present difficulties as nanotubes are highly insoluble. Their large surface areas mean that the van der Waals forces between nanotubes are very strong, resulting in clumping. A solvent must have a very high affinity to nanotubes in order to overcome this tendency to clump. Of common solvents, nanotubes are most soluble in 1,2-dichlorobenzene (DCB), where concentrations up to 95 mgL^{-1} can be achieved [100].

Nanotube solubility can be significantly enhanced by using surfactants. These are molecules that have a high affinity for nanotubes, allowing them to penetrate nanotube clumps and separate nanotubes out into a solution. Good surfactants for nanotubes

tend to be polymers, the mechanism for solubilisation being that the polymer molecule can wrap itself around the nanotube, preventing it from coming into contact with other nanotubes and clumping. Several polymers compatable with different solvents have been demonstrated, including carboxymethylcellulose in water [88] and polyvinyl alcohol [98] and PMMA [101] in various organic solvents.

Absorbers have also been prepared directly from solid nanotubes rather than from a solution [86]. Nanotube powder is placed between two substrates. The absorber can then have the form of a nanotube layer sandwiched between the substrates. Alternatively, high pressure can be used to contact bond the nanotubes to one of the substrates before removing the other. These methods can give very high nanotube densities and have produced modulation depths of several tens of percent.

6.4 Fabrication of a SWCNT saturable absorber

The SWCNT saturable absorbers described in this work were made from two different SWCNT-polymer solutions. The two polymer-solvent combinations used were polymethylmethacrylate (PMMA) in DCB and carboxymethylcellulose (CMC) in water. DCB was chosen as it is the organic solvent in which SWCNTs are most soluble. PMMA was a convenient polymer to use with DCB as it is highly soluble in DCB, allowing a large range of SWCNT:PMMA concentrations in solution. The CMC-water combination was chosen as an alternative as much more concentrated SWCNT solutions are possible if a surfactant is used. CMC was a convenient choice of surfactant as it can also form the matrix of the polymer-SWCNT composite. Both CMC and PMMA are highly transparent at 1 μm, making them suitable for use inside a VECSEL cavity, thought the solubility of CMC in water may affect the lifetimes of devices using CMC.

The proposed method was to apply thin films of SWCNT-polymer solutions to standard multilayer high reflector mirrors by spin coating. Once the solution had dried a SWCNT-polymer composite would remain on the mirror. Careful control of the SWCNT density and film thickness would allow the modulation depth to be matched to that required for VECSEL modelocking.

It is useful to know what kind of SWCNT density is needed in order to reach a given modulation depth. From values in the literature [102] we can estimate the absorption

cross-section of a single 500 nm SWCNT to be approximately $\sigma \approx 10^{-18}$ m^2. (This is assuming that the cross-section at 1 μm is similar to that at 1.5 μm. Much of the work in the literature is done for nanotubes around 1.5 μm rather than 1 μm as this wavelength range is of particular interest for communications.)

The Beer-Lambert absorption law is given by the equation

$$I = I_0 \exp\left(-\frac{n\sigma x}{2}\right), \tag{6.3}$$

where I_0 and I are the initial and transmitted intensities, n is the number density of nanotubes and x is the layer thickness. The factor of 2 arises because of the double pass through the absorbing layer in a mirror geometry. If we aim to reach a total absorption of 1% then, using the Beer-Lambert absorption law, we can find the required product of number density and layer thickness to be $nx \approx 1 \times 10^{16}$ m^{-2}. We can now calculate the required film thickness given a particular nanotube concentration.

As discussed in section 6.2 the saturation fluence of SWCNTs is much lower than that of quantum wells. In order to reach saturation at the same power levels a SWCNT-SA mode-locked VECSEL must have a spot size of approximately 100 μm on the absorber, compared to 10-15 μm in a SESAM mode-locked VECSEL. Cavities for VECSELs using carbon nanotube saturable absorbers must therefore be modified to give a much larger spot on the absorber.

Figure 6.5 (a) shows a similar Z-cavity to those used in chapters 4 and 5. Focal lengths of 38 mm for the output coupler and 50 mm for the high reflector can been used to give a 100 μm spot on the absorber and a 60 μm spot on the gain sample. Alternatively, the SWCNT-polymer layer could be applied to a curved output coupling mirror. This would allow a hemispherical cavity to be built with a flat gain sample at one end of the cavity and a focussing mirror/saturable absorber/output coupler at the other. This case is shown in figure 6.5 (b).

The following sections will describe the attempts to make a successful saturable absorber using these two combinations. In section 6.4.1 I will describe the DCB-PMMA work and in section 6.4.2 the CMC-water work. Section 6.5 will discuss conclusions and possible future work.

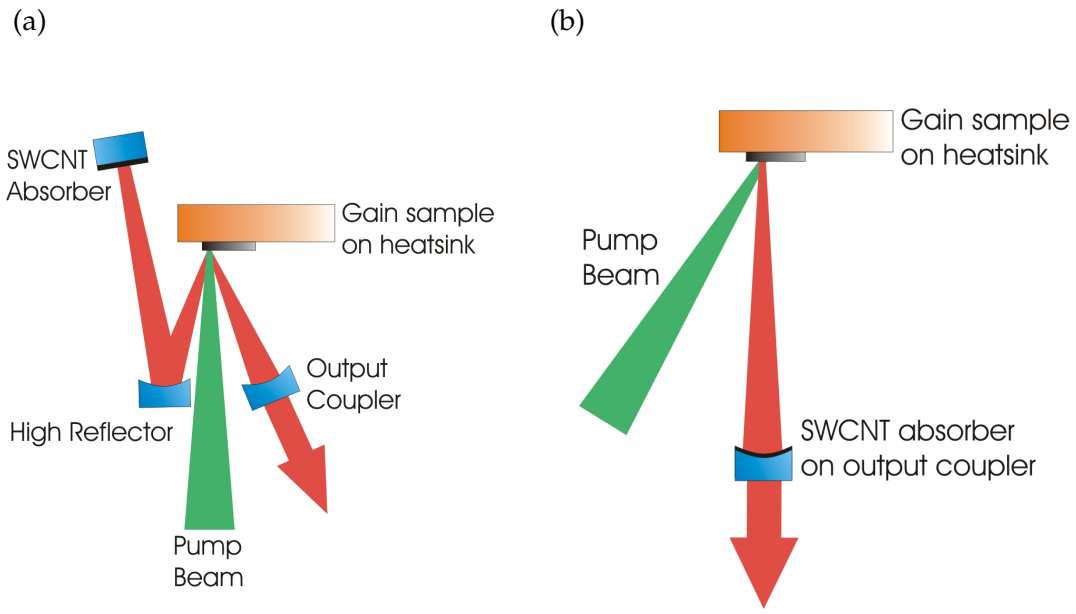

Figure 6.5: Cavities designed for large spot size on the absorber. (a) modified Z-cavity with focal lengths of 38 mm for the output coupler and 50 mm for the high reflector, (b) hemisperical 2-mirror cavity.

6.4.1 SWCNT saturable absorbers from SWCNT-PMMA-DCB solutions

The first attempts at producing SWCNT/PMMA films used solutions with concentrations of 95 mg/L of SWCNTs and 10 g/L of PMMA. By using estimates of the molecular masses of PMMA and SWCNT molecules and the density of PMMA we can estimate the number density of SWCNTs in a film made from this solution to be $\approx 2 \times 10^{22}$ m^{-3}. A film with this number density would require a layer 500 nm thick to achieve an absorption of 1%.

Solutions were prepared by first preparing a SWCNT/DCB mixture with over 95 mg/L of SWCNTs. This oversaturated solution was sonicated for several hours and then centrofuged to remove any undissolved SWCNTs. A quantity of PMMA was then added to the resulting saturated SWCNT/DCB solution before sonicating again to dissolve the PMMA.

This solution was applied to both high reflectors and glass slides using a standard photoresist spin coating recipe. Reflection/transmission spectra of the samples were taken in order to find the absorption due to the nanotubes, but no change due to the nanotubes could be measured. The high reflector still worked as a laser mirror with

only a slight increase in threshold, probably due largely to increased scattering losses. No sign of modelocking was observed in either autocorrelations of RF spectra. It was therefore concluded that any layers were far too thin to have a significant effect on the laser.

As a first attempt at increasing the layer thickness, samples were prepared by spin coating multiple layers from the same solution, with heating steps in between coats to completely dry the layers. Transmission spectra of glass slides coated in this way showed an increase in absorption with a spectrum consistent with SWCNTs. By subtracting the transmission of an uncoated slide from a coated one the absorption due to the nanotube-containing film can be found. Figure 6.6 (a) shows the absorption of such a film made from 20 spin coated layers. The peak at 1000 nm corresponds to the bandgap of a nanotube with a diameter of 0.7 nm. The peak at 1150 nm most likely represents contamination of the sample by nanotubes with a larger diameter. For comparison, figure 6.6 (b) shows the absorption spectrum of nanotubes from the same nanotube batch as measured by the supplier prior to shipping.

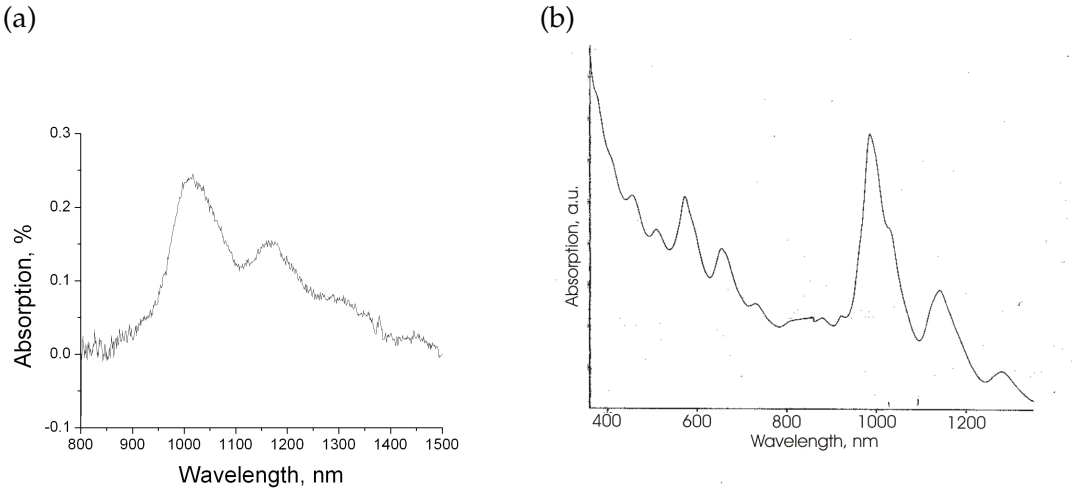

Figure 6.6: (a) SWCNT absorption spectrum extracted from the transmission spectrum of a glass slide coated in 50 nm thick SWCNT/PMMA composite. (b) SWCNT absorption data provided by the supplier for the batch of SWCNTs used.

An atomic force microscope was used to find the layer thickness. A metal point was used to scratch the film on a glass slide and the AFM used to measure the height profile across the resulting step. Figure 6.7 shows this profile. The film thickness can be

seen to vary between about 30 nm and 50 nm. It is possible that the film thickness did very this drastically but subsequent scanning electron microscope images of similar films (for example figure 6.8) showed them to be very uniform. The variations in the thickness are therefore likely to be due to the scratching of the slide.

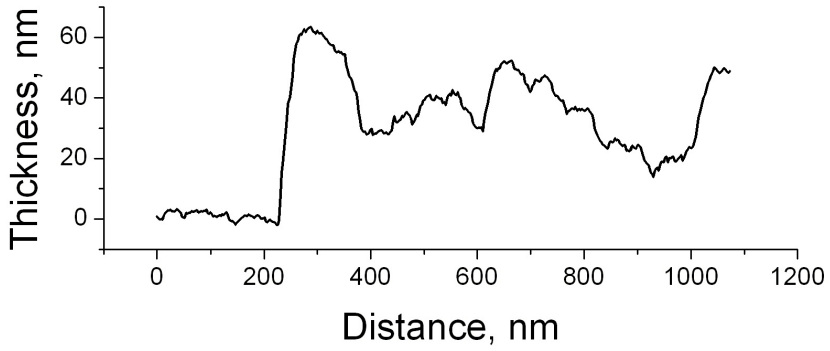

Figure 6.7: Thickness profile across the edge of a SWCNT/PMMA film measured using an AFM. The film thickness is approximately 40 nm.

As the thickness and the absorption of the film are known, it is possible to calculate the number density using the Beer-Lambert law. Using the value of the single nanotube cross section from above we can find $n \approx 10^{23}$ m^{-3}. This is an order of magnitude higher than the number density calculated above from the solution concentrations, though this calculation is likely to be an overestimate as it attributes all losses to the nanotubes and ignores any contribution due to imperfections in the film.

Mirrors coated using the same method as this glass slide did not significantly affect laser performance. This is not surprising as a 40 nm thick film would barely be exposed to the laser field as there is an antinode of the field at the surface of such a mirror. Taking into account the standing wave of the laser field, a film would be required to be 1 μm thick in order to give an absorption of 1%. Using this solution this would require an impractical 400 spin coated layers.

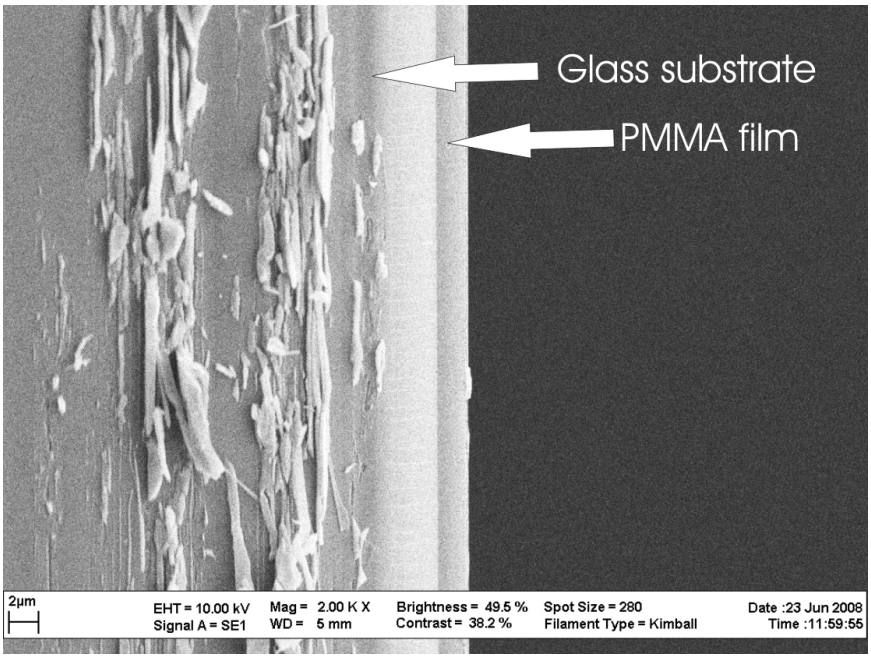

Figure 6.8: Side-on SEM image of a spin coated PMMA film on a glass substrate demonstrating the uniformity of the film.

Spin coating works by applying a droplet of polymer solution to a subtrate and then spinning it at high speed so that the solvent spreads into an even layer. If the original solvent thickness is above a certain value then the final thickness of the spin coated layer doesn't depend on the original thickness. If we assume that the rate of evaporation is proportional to the square root of the speed of rotation then the final film thickness can be modelled by the equation [103]

$$h \propto f^{-1/2}\nu_0^{1/3}, \tag{6.4}$$

where f is the rotation speed and ν_0 is the initial viscosity. The two routes to thicker films are therefore lower spin speeds or higher viscosity solutions.

Using these solutions, the spin speed can only be reduced to approximately 1000 rpm before the resulting films become non-uniform, and the speeds used to spin coat the films described above are already close to this limit. It is therefore necessary to increase the viscosity of the films by increasing the polymer concentration. As a model for the dependance of solution viscosity on polymer concentration we use the equation

$$\nu_0 = \nu_{solvent} + \nu_{polymer}c^{\gamma}, \tag{6.5}$$

where $\nu_{solvent}$ and $\nu_{polymer}$ are the solvent and polymer viscosities and c is the concentration of the polymer. γ is a numerical factor that depends on the polymer and solvent used. For the PMMA/DCB combination we assume that it is approximately 2.5. If we assume that the viscosity is dominated by the polymer then equation 6.4 can be rewritten as

$$h \propto f^{-1/2}(\nu_{solvent} + \nu_{polymer}c^{\gamma})^{1/3} \propto f^{-1/2}c^{5/6}. \tag{6.6}$$

Increasing the concentration will lead to thicker layers but will not give films with a higher absorption. This is because the number density of nanotubes in the film is inversely proportional to the polymer concentration, giving an overall dependance of the absorption coefficient on PMMA concentration of $\alpha \propto c^{-1/6}$.

If multiple layers are spun then an increased concentration may still be useful. When the solvent is applied on top of a polymer film then some of the film will be dissolved away during spin coating. If the solution has a higher concentration then the dissolution will be slower meaning that less of the previous layer is removed. Equally, if each individual layer is thicker, albeit less absorbing, then less of it will be removed by this process. Even so, many layers would need to be applied in order to reach a suitable absorption.

The ideal solution would be to increase the concentration of nanotubes, however we are already using a saturated solution. There are surfactants that are compatable with DCB and PMMA but they are typically very expensive. A more convenient solution is to move to a system where higher SWCNT concentrations are achievable.

6.4.2 SWCNT saturable absorbers from SWCNT-CMC-water solutions

The problems suffered using the PMMA/DCB combination can be solved by using either solutions with a higher nanotube concentration or with a higher viscosity for a given polymer concentration. The CMC/water combination offers both of these advantages. The use of a surfactant enables solutions to be prepared with much higher concentrations of nanotubes and CMC/water solutions have very high viscosities.

SWCNT/CMC/water solutions were prepared by first dissolving the required amount of CMC in water by sonication. SWCNTs were added to the CMC solution and were sonicated for several hours in order to dissolve as many nanotubes as possible. Again,

the solution was centrofuged to remove any undissolved nanotubes then sonicated further to make sure the solution was well mixed.

CMC/water solutions become very viscous very rapidly as the CMC concentration is increased. This presents difficulties for both the dissolution of the nanotubes and the centrofuging. If the solution is too viscous then the nanotubes cannot disperse well enough through the solution to dissolve. Also, undisolved clumps of nanotubes will require very high centrofuging speeds in order for the acceleration to overcome the viscosity of the solution and separate them.

The CMC/water combination also presents certain difficulties during spin coating. Water evaporates much more slowly than DCB, meaning that the sample must be spun for several minutes until the film has dried entirely. The high viscosity of these solutions is desirable but they also have a large surface tension. This means that the solution needs a faster spin speed in order to be evenly spread over the substrate. Both of these effects make it more difficult to spin coat high quality films using CMC/water. Using CMC with a lower degree of polymerisation would have helped this issue by reducing the surface tension without affecting the molecules ability to act as a surfactant.

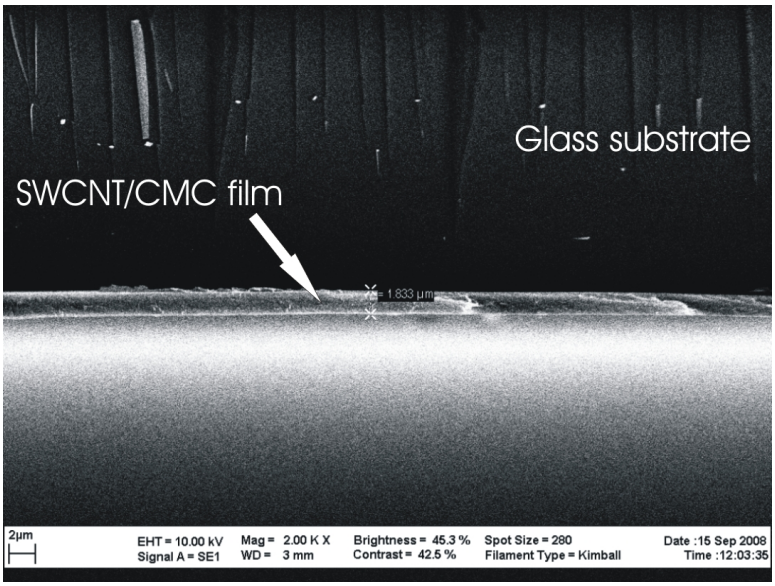

Figure 6.9: Side-on SEM image of a SWCNT/CMC film on a glass slide. The thickness of the film can be measured to be 1.8 μm

Some success was had in spin coating SWCNT/CMC films. The thickness of the films could be measured by cleaving a coated glass slide then using a scanning electron

microscope to image the film side-on. Films were measured at several points on the slide to estimate the uniformity of the film. Figure 6.9 shows an SEM image of a 1.8 μm thick layer of SWCNT/CMC composite on a glass slide. This film was made of 5 layers, spin coated at 500 rpm from a solution containing 250 mg/L of SWCNTs and 9.25 g/L of CMC. The film thickness was found to vary between 1.6 μm and 2.3 μm, though these variations only occur over millimeter distances on the film. The number density of SWCNTs in the film can be calculated in the same way as in section 6.4.1 leading to a theoretical value of 3% for the absorption of a 1.8 μm thick film.

The same solution was spin coated onto a high reflector using the same recipe. Figure 6.10 shows the stop band of the reflectivity spectrum of the resulting mirror, with the reflectivity spectrum of an uncoated high reflector for comparison. A dip in the reflectivity spectrum with a depth of 3% is visible at 1000 nm. This dip is consistent with the theoretical absorption predicted from the solution calculations. There is however, an overall loss increase of 7% compared to the uncoated high reflector.

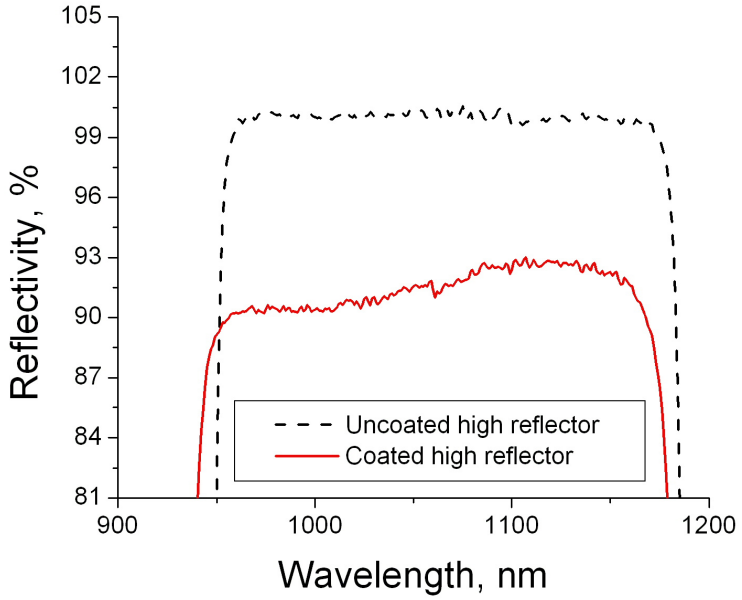

Figure 6.10: Close up of the stop band of both an uncoated high reflector and a high reflector coated with a SWCNT/CMC film. The decrease in reflectivity at 1000 nm due to the SWCNTs can be seen to be approximately 3%.

Assuming that the entire SWCNT absorption dip is saturable, then the ratio of sat-

urable to non-saturable loss for this film is 0.42. This is much worse than the SESAMs used for VECSEL modelocking, SESAM QT1627 has a much better ratio of 1.36 for example. If the thickness of such a film was reduced so that its modulation depth matched that of QT1627 then the non-saturable loss would be 0.7% compared to 0.2% for QT1627. The extra 0.5% loss is at the limit of what is tolerable for a VECSEL.

Thinner films could be prepared from the same solution to try to reduce the losses to a level suitable for VECSEL modelocking. Reducing the number of layers or increasing the spin speed would both give thinner films with lower losses. It is not known whether this ratio of saturable to non-saturable losses would be maintained in thinner films. The main sources of non-saturable loss are likely to be scattering losses and clumped nanotubes. The loss due to clumped nanotubes could be expected to decrease with film thickness, but the scattering loss depends primarily on the interface quality. Spin coating fewer layers and at higher speeds are likely to improve the surface quality, but it is not clear that the saturable to non-saturable ratio will be maintained.

6.5 Conclusions and future work

In theory, carbon nanotube saturable absorbers can have significantly faster recovery times and absorption bandwidths than the SESAMs currently used for VECSEL modelocking. Faster recovery times typically lead to shorter pulses and are therefore desirable. A large absorption bandwidth not only makes the absorber more wavelength-flexible but should also allow optical Stark effect modelocking to produce shorter pulses. Carbon nanotube saturable absorbers can also be made using standard solution processing techniques, which are much cheaper and more flexible than the epitaxial techniques used to grow SESAMs. Carbon nanotube saturable absorbers have been used to modelock a range of lasers at wavelengths between 1 μm and 1.9 μm, producing pulses with durations below 100 fs. The main obstacle to their use as modelocking elements for VECSELs lies in their high non-saturable losses.

In this chapter techniques are developed for making a carbon nanotube saturable absorber suitable for use with VECSELs. Different polymer/solvent combinations have been explored and their advantages and disadvantages identified. An acceptable ratio of saturable to non-saturable loss is achieved, but only with losses too high for use

with VECSELs. The overall loss could be decreased by reducing the layer thickness, but without further work it is not clear what effect this would have on the saturable to non-saturable loss ratio.

Several measures could be taken to further reduce the non-saturable losses. SEM images of the spin-coated films show that the film thickness varies by as much as 40% over the whole substrate. It is clear then, that the spin coating process could be improved on. Spin coating at higher speeds or using CMC with a lower molecular mass would improve film quality, as would spinning fewer layers onto the substrate.

Another source of loss is clumps of nanotubes. While most of the clumps of undissolved nanotubes were removed by centrofuging it is likely that some remained. Once again, lower molecular mass CMC would have been useful as the high viscosity of the CMC solutions reduced the effectiveness of centrofuging. Equally, a more powerful centrofuge would have been useful.

A final source of loss is the presence of metallic nanotubes and catalyst contaminants in the nanotube sample. The nanotube sample from the manufacturer is estimated to be over 80% semiconducting nanotubes, but this still leaves a significant source of loss from the remaining 20%. Methods exist for further purifying the sample, but are complex and time consuming and should only be used if absolutely essential.

Reflectivity measurements are a necessary tool for the analysis of saturable absorbers but other measurement equipment would be very valuable in order to fully characterise the absorbers. Most useful would be saturation fluence measurements, not so much as a tool for measuring the saturation fluence itself, but more to accurately measure the saturable and non-saturable losses. Pump-probe measurements would also be interesting, but are less useful regarding absorber design. There is also a clear consensus in the literature about the recovery times of SWCNTs making such measurement less crucial.

In conclusion, progress has been made towards a carbon nanotube saturable absorber. Suitable solution processing techniques have been identified, as have the necessary methods of analysis. Future work should focus on reducing the losses, particularly the non-saturable loss, to levels more suitable for VECSELs, and on improving the available characterisation apparatus to include saturation fluence measurements.

Chapter 7

Conclusions

7.1 Major results presented in this work

The work presented in this thesis represents significant progress towards the goal of mode-locked VECSELs as a practical source for applications such as terahertz generation and optical sampling. The 100 fs pulse duration threshold has been passed, making VECSELs competitive with other widely used sources. In particular, the performance of VECSELs is approaching that of mode-locked fibre lasers, especially at high repetition rates, where fibre lasers are limited by their long cavities.

The question of jitter is of great importance for these practical applications. Previous work by Wilcox et al. [4] has shown that VECSELs are capable of relatively low jitter values. The stabilisation scheme demonstrated in this work builds on this by achieving jitter values below 200 fs in the bandwidth 300 Hz to 1.5 MHz, suitable for these applications, by using a very simple, highly flexible and low cost set-up.

On a more fundamental level, the pulse trains emitted by the 70 fs VECSEL are indicative of a dynamic modelocking regime never before seen in semiconductor oscillators. A stronger optical Stark effect SESAM and a broader gain bandwidth have enabled pulses shorter that the carrier-phonon scattering time to be produced. Investigations of this regime indicate that below this threshold the dynamic saturation of the gain medium causes multiple very closely spaced pulses.

Despite their many successes, SESAMs have certain limitations in terms of producing ultrashort pulses, in particular their picosecond recovery times and limited spectral

bandwidths. Carbon nanotubes offer significant improvements in these respects. The work presented here has investigated the production of a carbon-nanotube-based saturable absorber via solution processing. While unsuccessful in producing a working absorber, the necessary techniques have been developed and difficulties identified.

7.2 Future work

Several aspects of mode-locked VECSEL performance still need to be improved if they are to reach their full potential. While pulse durations are now competitive with other similar sources, the behaviour of VECSELs in the pulse train regime is not well understood. A more complete picture of the carrier dynamics in the gain sample is needed if the multiple pulsing in these lasers is to be controlled. Pump-probe experiments on inverted gain samples would be particularly useful in this respect.

Work by Daniell et al. [54] implies that 70 fs is a limit to the pulse duration that can be reached using a optical Stark effect absorber with a given bandwidth. Shorter pulses could be produced by using an optical Stark effect saturable absorber with a larger bandwidth, for example one based on carbon nanotubes. Alternatively, an additional modelocking mechanism could be used to shorten pulses further, for example Kerr lens modelocking or quasi-soliton modelocking.

If VECSELs are to produce shorter pulses then broader gain spectra will be needed. This will require both an increase in the emission bandwidth of the laser medium and a reduction in the filtering caused by the sample microcavity. The microcavity effect could be reduced by using a thinner sample but antireflection coatings would provide a better solution. The emission bandwidth could be increased either by using a quantum dot based gain medium or by offsetting the peak wavelengths of the different quantum wells in the sample.

Another aspect of mode-locked VECSEL performance where significant improvements are possible is in the average power. One of the major selling points of the VECSEL architecture is the possibility for power scaling by increasing the emitting area on the gain sample. Improved heat removal by sample processing has also allowed CW VECSELs to achieve average powers of tens of watts. It is likely that sub-picosecond VECSELs could also give multi-watt outputs with suitable sample processing.

Research on VECSELs has lead to significant progress in the 12 years since their first demonstration. Frequency-doubled CW VECSELs have emerged as highly efficient sources of visible radiation. The first commercial high-power green VECSELs have been released recently as pump sources for Ti:sapphire lasers, but it is likely that these types of lasers will see greater use as RGB sources for laser projection systems, as their potential for high efficiencies and compact packaging make them strong competitors for these applications.

Mode-locked VECSELs have also seen significant improvements in performance, confirming their potential to produce ultrashort pulses at watt power levels and multi-gigahertz repetition rates. Two main approaches to improving their performance have emerged, with the main foci of research being either shorter pulse durations or greater compactness via sample integration. Ultimately, the progress made in these areas is likely to result in very compact, high repetition rate sources of femtosecond pulses, with great potential for wavelength flexibility. These sources would have a wide range of potential applications in areas such as optical clocking and sampling, communications, terahertz generation, and many others.

References

[1] http://kottan-labs.bgsu.edu/teaching/workshop2001/chapter5_files/image079.jpg.

[2] http://www.sc.ic.ac.uk/∼q_pv/ingaas.html.

[3] D. von der Linde. Characterization of the noise in continuously operating mode-locked lasers. *Applied Physics B-Photophysics and Laser Chemistry*, 39(4):201–217, 1986.

[4] KG Wilcox, HD Foreman, JS Roberts, and AC Tropper. Timing jitter of 897 MHz optical pulse train from actively stabilised passively modelocked surface-emitting semiconductor laser. *Electronics Letters*, 42(3):159–160, 2006.

[5] R. Saito, M. Fujita, G. Dresselhaus, and M. S Dresselhaus. Electronic structure of chiral graphene tubules. *Applied Physics Letters*, 60(18):2204–2206, 1992.

[6] Hiroshi Ajiki and Tsuneya Ando. Electronic states of carbon nanotubes. *Journal of the Physical Society of Japan*, 62(4):1255–1266, 1993.

[7] M. Kuznetsov, F. Hakimi, R. Sprague, and A. Mooradian. High-power (>0.5-W CW) diode-pumped vertical-external-cavity surface-emitting semiconductor lasers with circular TEM00 beams. *Photonics Technology Letters, IEEE*, 9(8):1063–1065, 1997.

[8] S. Lutgen, T. Albrecht, P. Brick, W. Reill, J. Luft, and W. Spath. 8-W high-efficiency continuous-wave semiconductor disk laser at 1000 nm. *Applied Physics Letters*, 82(21):3620–3622, 2003.

[9] Jun Ho Lee, Jun Youn Kim, Sang Moon Lee, Jae Ryung Yoo, Ki Sung Kim, Soo Haeng Cho, Seong Jin Lim, Gi Bum Kim, Sung Min Hwang, Taek Kim,

and Yong Jo Park. 9.1-W high-efficient continuous-wave end-pumped vertical-external-cavity surface-emitting semiconductor laser. *Photonics Technology Letters, IEEE*, 18(20):2117–2119, 2006.

[10] J Chilla, S Butterworth, A Zeitschel, J Charles, A Caprara, M Reed, and L Spinelli. High power optically pumped semiconductor lasers. In *Solid State Lasers XIII: Technology and Devices*, volume 5332, pages 143–150, 2004.

[11] William J. Alford, Thomas D. Raymond, and Andrew A. Allerman. High power and good beam quality at 980 nm from a vertical external-cavity surface-emitting laser. *J. Opt. Soc. Am. B*, 19(4):663–666, 2002.

[12] A. Härkönen, S. Suomalainen, E. Saarinen, L. Orsila, R. Koskinen, O. Okhotnikov, S. Calvez, and M. Dawson. 4 W single-transverse mode VECSEL utilising intra-cavity diamond heat spreader. *Electronics Letters*, 42(12):693–694, 2006.

[13] K.S. Kim, J.R. Yoo, S.M. Lee, S.J. Lim, J.Y. Kim, J.H. Lee, S.H. Cho, T. Kim, and Y.J. Park. Highly efficient InGaAs QW vertical external cavity surface emitting lasers emitting at 1060nm. *Journal of Crystal Growth*, 287(2):629 – 632, 2006.

[14] Marc Schmid, Sarah Benchabane, Firuz Torabi-Goudarzi, Richard Abram, Allister I. Ferguson, and Erling Riis. Optical in-well pumping of a vertical-external-cavity surface-emitting laser. *Applied Physics Letters*, 84(24):4860–4862, 2004.

[15] S.-S. Beyertt, M. Zorn, T. Kubler, H. Wenzel, M. Weyers, A. Giesen, G. Trankle, and U. Brauch. Optical in-well pumping of a semiconductor disk laser with high optical efficiency. *Quantum Electronics, IEEE Journal of*, 41(12):1439–1449, Dec. 2005.

[16] Nicola Schulz, Marcel Rattunde, Christian Ritzenthaler, Benno Rosener, Christian Manz, Klaus Kohler, Joachim Wagner, and Uwe Brauch. Resonant optical in-well pumping of an AlGaIn/AsSb-based vertical-external-cavity surface-emitting laser emitting at 2.35 mu m. *Applied Physics Letters*, 91(9):091113, 2007.

[17] Changling Yan, Yongqiang Ning, Li Qin, Dafu Cui, Yun Liu, Yanfang Sun, Zhenhua Jin, Huiqing Li, Getao Tao, Chao Wang, Lijun Wang, and Huilin Jiang. High-

power vertical-cavity surface-emitting laser with an extra Au layer. *Photonics Technology Letters, IEEE*, 17(8):1599–1601, 2005.

[18] S. Illek, T. Albrecht, P. Brick, S. Lutgen, I. Pietzonka, M. Furitsch, W. Diehl, J. Luft, and K. Streubel. Vertical-external-cavity surface-emitting laser with monolithically integrated pump lasers. *Photonics Technology Letters, IEEE*, 19(24):1952–1954, 2007.

[19] B. Rudin, A. Rutz, M. Hoffmann, D. J. H. C. Maas, A.-R. Bellancourt, E. Gini, T. Südmeyer, and U. Keller. Highly efficient optically pumped vertical-emitting semiconductor laser with more than 20 W average output power in a fundamental transverse mode. *Opt. Lett.*, 33(22):2719–2721, 2008.

[20] V.-M. Korpijärvi, M. Guina, J. Puustinen, P. Tuomisto, J. Rautiainen, A. Härkönen, A. Tukiainen, O. Okhotnikov, and M. Pessa. MBE grown GaInNAs-based multiwatt disk lasers. *Journal of Crystal Growth*, 311(7):1868 – 1871, 2009.

[21] Li Fan, Chris Hessenius, Mahmoud Fallahi, Jorg Hader, Hongbo Li, Jerome V. Moloney, Wolfgang Stolz, Stephan W. Koch, James T. Murray, and Robert Bedford. Highly strained InGaAs/GaAs multiwatt vertical-external-cavity surface-emitting laser emitting around 1170 nm. *Applied Physics Letters*, 91(13):131114, 2007.

[22] H. Lindberg, M. Strassner, E. Gerster, and A. Larsson. 0.8 W optically pumped vertical external cavity surface emitting laser operating CW at 1550 nm. *Electronics Letters*, 40(10):601–602, 2004.

[23] H. Lindberg, M. Strassner, and A. Larsson. Improved spectral properties of an optically pumped semiconductor disk laser using a thin diamond heat spreader as an intracavity filter. *Photonics Technology Letters, IEEE*, 17(7):1363–1365, 2005.

[24] Jussi Rautiainen, Jari Lyytikäinen, Alexei Sirbu, Alexandru Mereuta, Andrei Caliman, Eli Kapon, and Oleg G. Okhotnikov. 2.6 W optically-pumped semiconductor disk laser operating at 1.57-μm using wafer fusion. *Opt. Express*, 16(26):21881–21886, 2008.

[25] J.-M. Hopkins, N. Hempler, B. Rösener, N. Schulz, M. Rattunde, C. Manz, K. Köhler, J. Wagner, and D. Burns. High-power, AlGaIn/AsSb semiconductor disk laser at 2.0 μm. *Opt. Lett.*, 33(2):201–203, 2008.

[26] Jonna Paajaste, Soile Suomalainen, Riku Koskinen, Antti Härkönen, Mircea Guina, and Markus Pessa. High-power and broadly tunable GaSb-based optically pumped VECSELs emitting near 2μm. *Journal of Crystal Growth*, 311(7):1917 – 1919, 2009.

[27] M. Rahim, F. Felder, M. Fill, and H. Zogg. Optically pumped 5 μm IV-VI VECSEL with Al-heat spreader. *Opt. Lett.*, 33(24):3010–3012, 2008.

[28] J.E. Hastie, J.-M. Hopkins, S. Calvez, Chan Wook Jeon, D. Burns, R. Abram, E. Riis, A.I. Ferguson, and M.D. Dawson. 0.5-W single transverse-mode operation of an 850-nm diode-pumped surface-emitting semiconductor laser. *Photonics Technology Letters, IEEE*, 15(7):894–896, 2003.

[29] Jennifer Hastie, Stephane Calvez, Martin Dawson, Tomi Leinonen, Antti Laakso, Jari Lyytikäinen, and Markus Pessa. High power CW red VECSEL with linearly polarized TEM00 output beam. *Opt. Express*, 13(1):77–81, 2005.

[30] J. Rautiainen, A. Härkönen, V.-M. Korpijärvi, P. Tuomisto, M. Guina, and O. G. Okhotnikov. 2.7 W tunable orange-red GaInNAs semiconductor disk laser. *Opt. Express*, 15(26):18345–18350, 2007.

[31] JunHo Lee, SangMoon Lee, Taek Kim, and YongJo Park. 7 W high-efficiency continuous-wave green light generation by intracavity frequency doubling of an end-pumped vertical external-cavity surface emitting semiconductor laser. *Applied Physics Letters*, 89(24):241107, 2006.

[32] Li Fan, Ta-Chen Hsu, Mahmoud Fallahi, James T. Murray, Robert Bedford, Yushi Kaneda, Jorg Hader, Aramais R. Zakharian, Jerome V. Moloney, Stephan W. Koch, and Wolfgang Stolz. Tunable watt-level blue-green vertical-external-cavity surface-emitting lasers by intracavity frequency doubling. *Applied Physics Letters*, 88(25):251117, 2006.

[33] Jennifer E. Hastie, Lynne G. Morton, Alan J. Kemp, Martin D. Dawson, Andrey B. Krysa, and John S. Roberts. Tunable ultraviolet output from an intracavity frequency-doubled red vertical-external-cavity surface-emitting laser. *Applied Physics Letters*, 89(6):061114, 2006.

[34] Hans Lindberg, Mahdad Sadeghi, Mathias Westlund, Shumin Wang, Anders Larsson, Martin Strassner, and Saulius Marcinkevicius. Mode locking a 1550 nm semiconductor disk laser by using a GaInNAs saturable absorber. *Opt. Lett.*, 30(20):2793–2795, 2005.

[35] Jussi Rautiainen, Ville-Markus Korpijärvi, Janne Puustinen, Mircea Guina, and Oleg Okhotnikov. Passively mode-locked GaInNAs disk laser operating at 1220 nm. *Opt. Express*, 16(20):15964–15969, 2008.

[36] S. Hoogland, S. Dhanjal, A.C. Tropper, J.S. Roberts, R. Haring, R. Paschotta, F. Morier-Genoud, and U. Keller. Passively mode-locked diode-pumped surface-emitting semiconductor laser. *Photonics Technology Letters, IEEE*, 12(9):1135–1137, 2000.

[37] K.G. Wilcox, Z. Mihoubi, S. Elsmere, A. Quarterman, H.D. Foreman, S. Hashimoto, T. Sudmeyer, U. Keller, and A. Tropper. Passively modelocked 832 nm vertical-external-cavity surface-emitting semiconductor laser producing 15.3 ps pulses at 1.9 GHz repetition rate. *Electronics Letters*, 44(25):1469–1470, 2008.

[38] A. Aschwanden, D. Lorenser, H. J. Unold, R. Paschotta, E. Gini, and U. Keller. 10 GHz passively mode-locked external-cavity semiconductor laser with 1.4 W average output power. *Applied Physics Letters*, 86(13):131102, 2005.

[39] A. Garnache, S. Hoogland, A. C. Tropper, I. Sagnes, G. Saint-Girons, and J. S. Roberts. Sub-500-fs soliton-like pulse in a passively mode-locked broadband surface-emitting laser with 100 mW average power. *Applied Physics Letters*, 80(21):3892–3894, 2002.

[40] Peter Klopp, Florian Saas, Martin Zorn, Markus Weyers, and Uwe Griebner. 290-fs pulses from a semiconductor disk laser. *Opt. Express*, 16(8):5770–5775, 2008.

[41] D. Lorenser, D.J.H.C. Maas, H.J. Unold, A.-R. Bellancourt, B. Rudin, E. Gini, D. Ebling, and U. Keller. 50-GHz passively mode-locked surface-emitting semiconductor laser with 100-mW average output power. *Quantum Electronics, IEEE Journal of*, 42(8):838–847, 2006.

[42] S. Hoogland, A. Garnache, I. Sagnes, J.S. Roberts, and A.C. Tropper. 10-GHz train of sub-500-fs optical soliton-like pulses from a surface-emitting semiconductor laser. *Photonics Technology Letters, IEEE*, 17(2):267–269, 2005.

[43] A. Strittmatter, T.D. Germann, J. Pohl, U.W. Pohl, D. Bimberg, J. Rautiainen, M. Guina, and O.G. Okhotnikov. 1040 nm vertical external cavity surface emitting laser based on InGaAs quantum dots grown in Stranski-Krastanow regime. *Electronics Letters*, 44(4):290–291, 14 2008.

[44] T.D. Germann, A. Strittmatter, U.W. Pohl, D. Bimberg, J. Rautiainen, M. Guina, and O.G. Okhotnikov. Quantum-dot semiconductor disk lasers. *Journal of Crystal Growth*, 310(23):5182 – 5186, 2008.

[45] M. Hoffmann, Y. Barbarin, D. J. H. C. Maas, M. Golling, I. L. Krestnikov, S. S. Mikhrin, A. R. Kovsh, T. Sdmeyer, and U. Keller. Modelocked quantum dot vertical external cavity surface emitting laser. *Applied Physics B: Lasers and Optics*, 93(4):733–736, 2008.

[46] D. J. H. C. Maas, A.-R. Bellancourt, B. Rudin, M. Golling, H. J. Unold, T. Suedmeyer, and U. Keller. Vertical integration of ultrafast semiconductor lasers. *Applied Physics B-Lasers and Optics*, 88(4):493–497, 2007.

[47] Keith G. Wilcox, Zakaria Mihoubi, G. J. Daniell, Stephen Elsmere, Adrian Quarterman, Ian Farrer, David A. Ritchie, and Anne Tropper. Ultrafast optical Stark mode-locked semiconductor laser. *Opt. Lett.*, 33(23):2797–2799, 2008.

[48] A.H. Quarterman, K.G. Wilcox, Z. Mihoubi, S.P. Elsmere, I. Farrer, D.A. Richie, V. Apostolopoulos, and A.C. Tropper. 70-fs transform limited pulses emitted by InGaAs/GaAs quantum well laser. Submitted to Nature Photonics, 2009.

[49] L.A. Coldren and S.W. Corzine. *Diode lasers and photonic integrated circuits*. Wiley interscience, 1995.

[50] M Haiml, R Grange, and U Keller. Optical characterization of semiconductor saturable absorbers. *Applied Physics B-Lasers and Optics*, 79(3):331–339, 2004.

[51] H. A. Haus. Theory of mode-locking with a fast saturable absorber. *Journal of Applied Physics*, 46(7):3049–3058, 1975.

[52] H. A. Haus. Theory of mode-locking with a slow saturable absorber. *IEEE Journal of Quantum Electronics*, 11(9):736–746, 1975.

[53] A. Mysyrowicz, D. Hulin, A. Antonetti, A. Migus, W. T. Masselink, and H. Morkoç. "dressed excitons" in a multiple-quantum-well structure: Evidence for an optical stark effect with femtosecond response time. *Phys. Rev. Lett.*, 56(25):2748–2751, 1986.

[54] G. J. Daniell, Z. Mihoubi, K. G. Wilcox, and A. C. Tropper. Numerical model of the optical Stark effect as a mode-locking mechanism for femtosecond vertical-external-cavity surface-emitting semiconductor lasers. In *2008 Conference on Lasers and Electro-Optics & Quantum Electronics and Laser Science Conference, vols 1-9*, pages 919–920, 2008.

[55] O. E. Martinez, R. L. Fork, and J.P. Gordon. Theory of passively mode-locked lasers including self-phase modulation and group-velocity dispersion. *Optics Letters*, 9(5):156–158, 1984.

[56] H. A. Haus and Y. Silberberg. Laser mode-locking with addition of nonlinear index. *IEEE Journal of Quantum Electronics*, 22(2):325–331, 1986.

[57] J. A. Valdmanis, R. L. Fork, and J. P. Gordon. Generation of optical pulses as short as 27 femtoseconds directly from a laser balancing self-phase modulation, group-velocity dispersion, saturable absorption, and saturable gain. *Opt. Lett.*, 10(3):131–133, 1985.

[58] P. F. Curley, Ch. Spielmann, T. Brabec, F. Krausz, E. Wintner, and A. J. Schmidt. Operation of a femtosecond Ti:sapphire solitary laser in the vicinity of zero group-delay dispersion. *Opt. Lett.*, 18(1):54–56, 1993.

[59] U. Keller, D. A. B. Miller, G. D. Boyd, T. H. Chiu, J. F. Ferguson, and M. T. Asom. Solid-state low-loss intracavity saturable absorber for Nd:YLF lasers: an antiresonant semiconductor Fabry-Perot saturable absorber. *Opt. Lett.*, 17(7):505–507, 1992.

[60] S. Gupta, J.F. Whitaker, and G.A. Mourou. Ultrafast carrier dynamics in III-V semiconductors grown by molecular-beam epitaxy at very low substrate temperatures. *Quantum Electronics, IEEE Journal of*, 28(10):2464–2472, 1992.

[61] A.E. Siegman. *Lasers*. University science books, 1986.

[62] S. Hoogland, A. Garnache, K.G. Wilcox, Z. Mihoubi, S. Elsmere, A. Quarterman, and A. Tropper. Spectrotemporal gain bandwidth measurement in an InGaAs/GaAsP quantum well vertical-external-cavity surface-emitting semiconductor laser. In *2008 Conference on Lasers and Electro-Optics (CLEO)*, page 2 pp., 2008.

[63] W. H. Knox, C. Hirlimann, D. A. B. Miller, J. Shah, D. S. Chemla, and C. V. Shank. Femtosecond excitation of nonthermal carrier populations in GaAs quantum-wells. *Physical Review Letters*, 56(11):1191–1193, 1986.

[64] Chi-Kuang Sun, Boris Golubovic, Hong-Kyun Choi, Christine A. Wang, and James G. Fujimoto. Femtosecond investigations of spectral hole burning in semiconductor lasers. *Applied Physics Letters*, 66(13):1650–1652, 1995.

[65] J. D. Harvey, J. M. Dudley, P. F. Curley, C. Spielmann, and F. Krausz. Coherent effects in a self-mode-locked Ti:sapphire laser. *Opt. Lett.*, 19(13):972–974, 1994.

[66] Victor V. Kozlov. Self-induced transparency soliton laser via coherent mode locking. *Phys. Rev. A*, 56(2):1607–1612, 1997.

[67] T. Yilmaz, C.M. Depriest, A. Braun, J.H. Abeles, and Jr. Delfyett, P.J. Noise in fundamental and harmonic modelocked semiconductor lasers: experiments and simulations. *Quantum Electronics, IEEE Journal of*, 39(7):838–849, 2003.

[68] D. E. Spence, J. M. Dudley, K. Lamb, W. E. Sleat, and W. Sibbett. Nearly quantum-limited timing jitter in a self-mode-locked Ti sapphire laser. *Optics Letters*, 19(7):481–483, 1994.

[69] A. Schlatter, B. Rudin, S. C. Zeller, R. Paschotta, G. J. Spühler, L. Krainer, N. Haverkamp, H. R. Telle, and U. Keller. Nearly quantum-noise-limited timing jitter from miniature Er:Yb:glass lasers. *Opt. Lett.*, 30(12):1536–1538, 2005.

[70] T.R. Clark, T.F. Carruthers, P.J. Matthews, and III. Duling, I.N. Phase noise measurements of ultrastable 10 GHz harmonically modelocked fibre laser. *Electronics Letters*, 35(9):720–721, 1999.

[71] R. Paschotta. Noise of mode-locked lasers (part II): timing jitter and other fluctuations. *Applied Physics B: Lasers and Optics*, 79(2):163–173, 2004.

[72] H. A. Haus and A. Mecozzi. Noise of mode-locked lasers. *IEEE Journal of Quantum Electronics*, 29(3):983–996, 1993.

[73] M.J.W. Rodwell, D.M. Bloom, and K.J. Weingarten. Subpicosecond laser timing stabilization. *IEEE Journal of Quantum Electronics*, 25(4):817–827, 1989.

[74] R Paschotta, B Rudin, A Schlatter, GJ Spuhler, L Krainer, SC Zeller, N Haverkamp, HR Telle, and U Keller. Relative timing jitter measurements with an indirect phase comparison method. *Applied Physics B-Lasers and Optics*, 80(2):185–192, 2005.

[75] A.H. Quarterman, K.G. Wilcox, S.P. Elsmere, Z. Mihoubi, and A.C. Tropper. Active stabilisation and timing jitter characterisation of sub-500 fs pulse passively modelocked VECSEL. *Electronics Letters*, 44(19):1135–1137, 2008.

[76] Z. Mihoubi, K. G. Wilcox, S. Elsmere, A. Quarterman, R. Rungsawang, I. Farrer, H. E. Beere, D. A. Ritchie, A. Tropper, and V. Apostolopoulos. All-semiconductor room-temperature terahertz time domain spectrometer. *Optics Letters*, 33(18):2125–2127, 2008.

[77] A. Bartels, R. Cerna, C. Kistner, A. Thoma, F. Hudert, C. Janke, and T. Dekorsy. Ultrafast time-domain spectroscopy based on high-speed asynchronous optical sampling. *Review of Scientific Instruments*, 78(3):8, 2007.

[78] T. Schibli, K. Minoshima, H. Kataura, E. Itoga, N. Minami, S. Kazaoui, K. Miyashita, M. Tokumoto, and Y. Sakakibara. Ultrashort pulse-generation by saturable absorber mirrors based on polymer-embedded carbon nanotubes. *Opt. Express*, 13(20):8025–8031, 2005.

[79] Kok Hann Fong, Kazuro Kikuchi, Chee S. Goh, Sze Y. Set, Rachel Grange, Markus Haiml, Adrian Schlatter, and Ursula Keller. Solid-state Er:Yb:glass laser mode-locked by using single-wall carbon nanotube thin film. *Opt. Lett.*, 32(1):38–40, 2007.

[80] Jong Hyuk Yim, Won Bae Cho, Soonil Lee, Yeong Hwan Ahn, Kihong Kim, Hanjo Lim, Gunter Steinmeyer, Valentin Petrov, Uwe Griebner, and Fabian Rotermund. Fabrication and characterization of ultrafast carbon nanotube saturable absorbers for solid-state laser mode locking near 1 μm. *Applied Physics Letters*, 93(16):161106, 2008.

[81] Andreas Schmidt, Simon Rivier, Günter Steinmeyer, Jong Hyuk Yim, Won Bae Cho, Soonil Lee, Fabian Rotermund, Maria C. Pujol, Xavier Mateos, Magdalena Aguiló, Francesc Díaz, Valentin Petrov, and Uwe Griebner. Passive mode locking of Yb:KLuW using a single-walled carbon nanotube saturable absorber. *Opt. Lett.*, 33(7):729–731, 2008.

[82] Won Bae Cho, Jong Hyuk Yim, Sun Young Choi, Soonil Lee, Uwe Griebner, Valentin Petrov, and Fabian Rotermund. Mode-locked self-starting Cr:forsterite laser using a single-walled carbon nanotube saturable absorber. *Opt. Lett.*, 33(21):2449–2451, 2008.

[83] Dmitry V. Khudyakov, Anatoly S. Lobach, and Viktor A. Nadtochenko. Nonlinear optical absorption of single-wall carbon nanotubes in carboxymethylcellulose thin polymer film and its application as a saturable absorber for mode-locking in pulsed Nd:glass laser. *Appl. Opt.*, 48(8):1624–1627, 2009.

[84] Samuli Kivistö, Tommi Hakulinen, Antti Kaskela, Brad Aitchison, David P. Brown, Albert G. Nasibulin, Esko I. Kauppinen, Antti Härkönen, and Oleg G. Okhotnikov. Carbon nanotube films for ultrafast broadband technology. *Opt. Express*, 17(4):2358–2363, 2009.

[85] J. W. Nicholson, R. S. Windeler, and D. J. DiGiovanni. Optically driven deposition of single-walled carbon-nanotube saturable absorbers on optical fiber end-faces. *Opt. Express*, 15(15):9176–9183, 2007.

[86] S.Y. Set, H. Yaguchi, Y. Tanaka, and M. Jablonski. Laser mode locking using a saturable absorber incorporating carbon nanotubes. *Lightwave Technology, Journal of*, 22(1):51–56, Jan. 2004.

[87] Fumio Shohda, Takafumi Shirato, Masataka Nakazawa, Junji Mata, and Jun Tsukamoto. 147 fs, 51 MHz soliton fiber laser at 1.56 μm with a fiber-connector-type SWNT/P3HT saturable absorber. *Opt. Express*, 16(25):20943–20948, 2008.

[88] A. V. Tausenev, E. D. Obraztsova, A. S. Lobach, A. I. Chernov, V. I. Konov, P. G. Kryukov, A. V. Konyashchenko, and E. M. Dianov. 177 fs erbium-doped fiber laser mode locked with a cellulose polymer film containing single-wall carbon nanotubes. *Applied Physics Letters*, 92(17):171113, 2008.

[89] K. Kieu and F.W. Wise. Soliton thulium-doped fiber laser with carbon nanotube saturable absorber. *Photonics Technology Letters, IEEE*, 21(3):128–130, 2009.

[90] Yong-Won Song, Shinji Yamashita, Chee S. Goh, and Sze Y. Set. Passively mode-locked lasers with 17.2-GHz fundamental-mode repetition rate pulsed by carbon nanotubes. *Opt. Lett.*, 32(4):430–432, 2007.

[91] Ralph Krupke, Frank Hennrich, Hilbert v. Lohneysen, and Manfred M. Kappes. Separation of Metallic from Semiconducting Single-Walled Carbon Nanotubes. *Science*, 301(5631):344–347, 2003.

[92] Woo-Jae Kim, Monica L. Usrey, and Michael S. Strano. Selective functionalization and free solution electrophoresis of single-walled carbon nanotubes: Separate enrichment of metallic and semiconducting SWNT. *Chemistry of Materials*, 19(7):1571–1576, 2007.

[93] T.W. Ebbesen and P.M. Ajayan. Large-scale synthesis of carbon nanotubes. *Nature*, 358(6383):220–222, 1992.

[94] Ting Guo, Pavel Nikolaev, Andrew G. Rinzler, David Tomanek, Daniel T. Colbert, and Richard E. Smalley. Self-assembly of tubular fullerenes. *The Journal of Physical Chemistry*, 99(27):10694–10697, 1995.

[95] Morinobu Endo, Kenji Takeuchi, Kiyoharu Kobori, Katsushi Takahashi, Harold W. Kroto, and A. Sarkar. Pyrolytic carbon nanotubes from vapor-grown carbon fibers. *Carbon*, 33(7):873 – 881, 1995.

[96] Munehiro Ishioka, Toshihiko Okada, Kenji Matsubara, and Morinobu Endo. Formation of vapor-grown carbon fibers in CO-CO_2-H_2 mixtures, II. Influence of catalyst. *Carbon*, 30(6):865 – 868, 1992.

[97] Y.-C. Chen, N. R. Raravikar, L. S. Schadler, P. M. Ajayan, Y.-P. Zhao, T.-M. Lu, G.-C. Wang, and X.-C. Zhang. Ultrafast optical switching properties of single-wall carbon nanotube polymer composites at 1.55 μm. *Applied Physics Letters*, 81(6):975–977, 2002.

[98] Z. Sun, A. G. Rozhin, F. Wang, V. Scardaci, W. I. Milne, I. H. White, F. Hennrich, and A. C. Ferrari. L-band ultrafast fiber laser mode locked by carbon nanotubes. *Applied Physics Letters*, 93(6):061114, 2008.

[99] Khanh Kieu and Masud Mansuripur. Femtosecond laser pulse generation with a fiber taper embedded in carbon nanotube/polymer composite. *Opt. Lett.*, 32(15):2242–2244, 2007.

[100] Jeffrey L. Bahr, Edward T. Mickelson, Michael J. Bronikowski, Richard E. Smalley, and James M. Tour. Dissolution of small diameter single-wall carbon nanotubes in organic solvents. *Chemical Communications*, 2:193–194, 2001.

[101] Masataka Nakazawa, Seiji Nakahara, Toshihiko Hirooka, Masato Yoshida, Toshikuni Kaino, and Kyoji Komatsu. Polymer saturable absorber materials in the 1.5 μm band using poly-methyl-methacrylate and polystyrene with single-wall carbon nanotubes and their application to a femtosecond laser. *Opt. Lett.*, 31(7):915–917, 2006.

[102] M. F. Islam, D. E. Milkie, C. L. Kane, A. G. Yodh, and J. M. Kikkawa. Direct measurement of the polarized optical absorption cross section of single-wall carbon nanotubes. *Phys. Rev. Lett.*, 93(3):037404, 2004.

[103] Dietrich Meyerhofer. Characteristics of resist films produced by spinning. *Journal of Applied Physics*, 49(7):3993–3997, 1978.

Appendix A

Selected Publications

1. A. H. Quarterman, K. G. Wilcox, S. P. Elsmere, Z. Mihoubi, V. Apostolopoulos and A. C. Tropper, "70-fs Transform-Limited Pulses Emitted by InGaAs/GaAs Quantum Well Laser", Submitted to Nature Photonics, 2009.

2. A. H. Quarterman, K. G. Wilcox, S. P. Elsmere, Z. Mihoubi, and A. C. Tropper, "Active stabilisation and timing jitter characterisation of sub-500 fs pulse passively modelocked VECSEL," Electronics Letters 44, 1135-1136 (2008).

3. A. H. Quarterman, K. G. Wilcox, Z. Mihoubi, S. P. Elsmere, and A. C. Tropper, "Characterization of Pulse Timing Jitter of Actively Stabilised 1-GHz Vertical-External-Cavity Surface-Emitting Semiconductor Laser Producing 500-fs Pulses," 2008 Conference on Lasers and Electro-Optics and Quantum Electronics and Laser Science Conference, Vols 1-9, 1135-1136 (2008).

4. S. P. Elsmere, Z. Mihoubi, A. Quarterman, A. C. Tropper, P. Dupriez, J. Nilsson, and J. S. Roberts, "High repetition-rate sub-picosecond source of fibre-amplified vertical-external-cavity surface-emitting semiconductor laser pulses," CLEO/Europe - IQEC 2007. European Conference on Lasers and Electro-Optics and the International Quantum Electronics Conference, 493 (2007).

5. S. P. Elsmere, Z. Mihoubi, A. H. Quarterman, P. Dupriez, J. Nilsson, J. S. Roberts, and A. C. Tropper, "High-repetition-rate subpicosecond source of fiber-amplified vertical-external-cavity surface-emitting semiconductor laser pulses," Ieee Photonics Technology Letters 20, 623-625 (2008).

6. Z. Mihoubi, K. G. Wilcox, S. Elsmere, A. Quarterman, R. Rungsawang, I. Farrer, H. E. Beere, D. A. Ritchie, A. Tropper, and V. Apostolopoulos, "All-semiconductor room-temperature terahertz time domain spectrometer," Optics Letters 33, 2125-2127 (2008).

7. K. G. Wilcox, Z. Mihoubi, G. J. Daniell, S. Elsmere, A. Quarterman, I. Farrer, D. A. Ritchie, and A. Tropper, "Ultrafast optical Stark mode-locked semiconductor laser," Optics Letters 33, 2797-2799 (2008).

8. K. G. Wilcox, Z. Mihoubi, S. Elsmere, A. Quarterman, H. D. Foreman, S. Hashimoto, T. Sudmeyer, U. Keller, and A. Tropper, "Passively modelocked 832 nm vertical-external-cavity surface-emitting semiconductor laser producing 15.3 ps pulses at 1.9 GHz repetition rate," Electronics Letters 44, 1469-U1135 (2008).

9. K. G. Wilcox, Z. Mihoubi, S. P. Elsmere, A. H. Quarterman, H. D. Foreman, and A. Tropper, "Passively Mode-locked 832-nm Vertical-External-Cavity Surface-Emitting Semiconductor Laser Producing 15.3-ps Pulses at 1.9-GHz Repetition Rate," 2008 Conference on Lasers and Electro-Optics and Quantum Electronics and Laser Science Conference, Vols 1-9, 2163-2164 (2008).